

Polarized signals from oriented frozen hydrometeors
using passive microwave radiometry

Inaugural-Dissertation
zur
Erlangung des Doktorgrades
der Mathematisch-Naturwissenschaftlichen Fakultät
der Universität zu Köln

vorgelegt von
Xinxin Xie
aus Hunan, China

Köln

2012

Berichterstatter: Prof. Dr. S. Crewell
Prof. Dr. C. Simmer

Tag der mündlichen Prüfung: 26.06.2012

Abstract

Ice clouds play a significant role in energy budget of the earth-atmosphere system, and they also participate in global hydrological cycle. Thick ice clouds which are associated with precipitation transfer energy and water between the atmosphere and the earth. The net effects of ice clouds on the earth-atmosphere system highly depend on their microphysical properties. However, the complex and variable structure of ice clouds makes it difficult to capture them well in models. The oversimplified microphysical properties of ice clouds in retrievals introduce significant uncertainties in weather and climate studies.

The knowledge on the orientation of ice particles is very limited. The orientation of frozen hydrometeors which induces polarization signatures determines the magnitude of polarized signals. In order to investigate the potential polarized signatures induced by the oriented frozen hydrometeors, ground-based polarization observations have been performed at “Umweltforschungsstation Schneefernerhaus” (UFS) on Mount Zugspitze (German Alps) at 2650 m above sea level. In this study, the polarization observations carried out by a ground-based dual polarized microwave radiometer (DPR) at 150 GHz are investigated together with auxiliary instruments deployed at UFS, i.e., a second microwave radiometer (HATPRO) and a K-band micro rain radar (MRR). HATPRO measures liquid water path (LWP) and integrated water vapor (IWV) during snowfall, and MRR operating at 24.1 GHz provides indirect snow water path (SWP) information.

Based on the observations, the analysis of a single snow case and one-year snowfall data show that the brightness temperature (TB) differences between the vertical and horizontal polarizations reach up to -10 K at an elevation angle of 34.8° during snowfall. The polarized signals during snowfall can be explained well by the occurrence of oriented snow particles. The analysis of the synergic observations shows the effects of snowfall parameters on polarization differences (PDs) observed with DPR at 150 GHz. The dependencies of the measured PD and TB on MRR integrated radar reflectivity and independently derived LWP are discussed. It shows that the high SWP indicated by high values of MRR integrated reflectivity enhances both TB and PD due to the scattering effects of snow particles. Meanwhile, TBs are found to be enhanced during snowfall when supercooled liquid water is present, while PD resulting from oriented snow particles is damped by the increase of LWP. The polarization observations support the potential role of polarization measurements in improving retrievals of snowfall microphysical parameters.

To evaluate the effects of SWP and LWP on PD and TB, radiative transfer (RT) simulations assuming horizontally aligned snow oblates using a polarized RT model have been performed. PD and TB observations can be captured well by the RT model with given reasonable assumptions on the microphysical parameters of oriented snow oblates. Additionally, the uncertainties of PD and TB caused by snow microphysical properties are fully examined in the RT simulations. The “damping (enhancing)” effects of supercooled liquid water on

PD (TB) are further interpreted by a simple physical model where the height of cloud liquid varies with respect to the dichroic snow layer. From the ground-based observations, it is found that PD resulting from oriented snow particles is absorbed by supercooled liquid below snow layers. When supercooled liquid water is located above snow layers, PD is damped since it is compensated by the emission of supercooled liquid water penetrating the snow layer. TB is generally enhanced by the presence of LWP: the warmer the supercooled liquid water, the larger the TB.

The polarization observations promote the design of new instruments further. Under an assumption that ice particles are oriented, RT simulations are performed for the space-borne satellite FengYun-4 (FY-4) channels to examine polarization information content for ice cloud characterization. The results show that polarization can be beneficial for ice cloud retrievals and additional information can be provided by polarized signals to quantify ice cloud parameters, especially at high frequency channels. Therefore, the present work strongly suggests the deployment of microwave polarization channels for ice cloud observations.

Zusammenfassung

Eiswolken spielen eine wichtige Rolle im Energiehaushalt des Systems Erde-Atmosphäre und nehmen darüber hinaus auch einen wichtigen Platz im globalen Wasserkreislauf ein. Dicke Eiswolken, welche mit der Niederschlagsentstehung in Verbindung stehen, transportieren Energie und Wasser zwischen Atmosphäre und Erdboden. Der Netto-Effekt von Eiswolken auf das Erde-Atmosphäre System hängt stark von deren mikrophysikalischen Eigenschaften ab. Jedoch macht gerade die komplexe und variable Struktur der Eiswolken es schwierig diese in Modellen abzubilden. Die stark vereinfachten mikrophysikalischen Eigenschaften von Eiswolken in Ableitungsalgorithmen führen daher zu erheblichen Unsicherheiten in Wetter- und Klimastudien.

Unser Wissen über die Orientierung von Eispartikeln ist sehr begrenzt. Die Orientierung von gefrorenen Hydrometeoren, welche polarisierte Signale erzeugen können, bestimmt maßgeblich die Stärke der Polarisierung. Um das Potenzial polarimetrischer Signale zu untersuchen, welche durch gefrorene Hydrometeore verursacht werden, wurden bodengebundene polarimetrische Messungen an der Umweltforschungsstation Schneefernerhaus (UFS) unterhalb der Zugspitze (Deutsche Alpen) auf 2650 m Höhe (NN) durchgeführt. Im Rahmen dieser Studie wurden polarimetrische Beobachtungen bei 150 GHz von einem boden-gebundenen Dual Polarized Microwave Radiometer (DPR) zusammen mit zusätzlichen Instrumenten, welche auf der UFS installiert waren untersucht. Diese zusätzlichen Instrumente bestanden u.a. aus einem zweiten Mikrowellenradiometer (HATPRO) und einem Mikro-Regenradar (MRR) welches im K-Band arbeitet. Mit HATPRO können der vertikal integrierte Flüssigwassergehalt (LWP) sowie der integrierte Wasserdampfgehalt (IWV) während Schneefall gemessen werden, während das MRR, welches bei 24.1 GHz betrieben wird, eine indirekte Information über den vertikal integrierten Schneewassergehalt (SWP) liefert.

Basierend auf diesen Beobachtungen ergaben die Analysen eines einzelnen Schneefallereignisses sowie des gesamten einjährigen Schneefalldatensatzes, dass die Unterschiede in den Strahlungstemperaturen (TB) zwischen vertikaler und horizontaler Polarisationsrichtung während Schneefall bis zu -10 K bei einem Elevationswinkel von $34,8^\circ$ betragen. Die Polarisations-signale während der Schneefallereignisse können durch das Auftreten von orientierten Schneepartikeln erklärt werden. Zusammen mit den anderen Beobachtungen zeigte die Untersuchung den Einfluß der verschiedenen Schneefallparameter auf die Polarisationsdifferenzen (PDs) bei 150 GHz welche mit dem DPR gemessen wurden. Außerdem werden in dieser Arbeit die Abhängigkeiten der gemessenen PD und TB von der mittels MRR gemessenen integrierten Radarreflektivität und dem unabhängig abgeleiteten LWP diskutiert. Es zeigt sich, dass die hohen SWP Werte, angezeigt durch hohe Werte der vom MRR gemessenen integrierten Radarreflektivität, durch Streueffekte an den Schneepartikeln zu erhöhten TB und PD führen. Die TBs sind ebenfalls erhöht bei Schneefallereignissen, welche unterkühltes Flüssigwasser enthalten. Im Gegensatz dazu, werden die PDs, hervorgerufen durch orientierte

Schneepartikel, durch zunehmende LWP Gehalte gedämpft. Die Polarisationsbeobachtungen bestätigen daher das Potenzial polarisierter Beobachtungen für die Verbesserung der Ableitung mikrophysikalischer Schneefallparameter.

Um die Effekte von SWP und LWP auf die PD und TB genauer zu untersuchen, wurden Strahlungstransportsimulationen (RT) mit einem polarisierten Strahlungstransportmodell und horizontal orientierten Schnee-Ellipsoiden durchgeführt. Die beobachteten Werte von TB und PD können unter Annahme realistischer Werte für die mikrophysikalischen Eigenschaften der Schnee-Ellipsoide gut durch die RT-Simulationen wiedergegeben werden. Ebenfalls wurden die Unsicherheiten der TB und PD, welche durch die variablen mikrophysikalischen Schneefalleigenschaften verursacht werden, eingehend mittels RT Simulationen untersucht. Der "dämpfende (erhöhende)" Effekt des unterkühlten Flüssigwassers auf die PD (TB) wurde weitergehend mittels eines einfachen physikalischen Modells überprüft, bei dem die Höhe der Flüssigwasserschicht in Bezug zur Schneefallschicht variiert werden kann. Bodengebundene Beobachtungen ergaben, dass die durch orientierte Schneepartikel hervorgerufenen PD von Flüssigwasserschichten unterhalb der Schneefallschicht absorbiert werden. Wenn die unterkühlte Flüssigwasserschicht sich hingegen über der Schneefallschicht befindet, führt dies zu einer Dämpfung der PD, da es durch die Emission des unterkühlten Flüssigwassers, welches die Schneefallschicht durchdringt, kompensiert wird. Die TB werden jedoch grundsätzlich durch das Vorhandensein von unterkühltem Flüssigwasser erhöht: Je wärmer das unterkühlten Flüssigwasser dabei ist, desto höher sind die korrespondierenden TB.

Die Polarisationsbeobachtungen bestärken die Entwicklung neuer Messinstrumente. Unter der Annahme orientierter Eispartikel wurden RT Simulationen für die Frequenzkanäle des Satelliten FengYun-4 (FY-4) durchgeführt um den Informationsgehalt polarisierter Messungen für die Charakterisierung von Eiswolken zu untersuchen. Die Ergebnisse zeigen, dass Polarisationsmessungen wertvoll sein können für Ableitungsalgorithmen von Eiswolken. Besonders bei den hochfrequenten Frequenzkanälen können Polarisationsmessungen zusätzliche Informationen liefern um Parameter von Eiswolken zu quantifizieren. Ausgehend von den Ergebnissen der hier vorgestellten Arbeit ist es deshalb äußerst empfehlenswert für die Beobachtung von Eiswolken polarisierte Mikrowellenempfänger einzusetzen.

Contents

1	Introduction	1
1.1	Motivation	1
1.2	State-of-the-art	3
1.2.1	Microwave remote sensing of frozen hydrometeors	3
1.2.2	Polarization radiation observed by microwave radiometers	6
1.3	Focus of the study	8
2	Methodology	11
2.1	Definition of terminology in radiative transfer	11
2.1.1	Basic radiative parameters	11
2.1.2	Polarization and Stokes parameters	12
2.1.3	Radiation interactions in the atmosphere	15
2.2	Radiative transfer theory	20
2.2.1	The polarized radiative transfer equation	20
2.2.2	Solution to the polarized radiative transfer equation	21
2.3	Scattering properties of particles	23
2.3.1	T-matrix method	24
2.3.2	DDA algorithm	25
3	Instrumentation and data set	29
3.1	Instrumentation	29
3.1.1	Microwave radiometer: DPR	29
3.1.2	Microwave radiometer: HATPRO	30
3.1.3	Micro rain radar	32
3.1.4	Additional instruments	32
3.2	DPR PD bias correction	32

4	Ground-based polarization observation during snowfall	37
4.1	Case study: 4 April 2010	37
4.2	Statistical analysis in 2010	39
4.3	Conclusions	43
5	RT simulations during snowfall	45
5.1	Case study: 4 April 2010	45
5.1.1	RT setup	45
5.1.2	RT results	47
5.2	Sensitivity of PD and TB to snow parameters	50
5.2.1	Aspect ratio	51
5.2.2	Particle canting angle	53
5.2.3	Mass size relationship	55
5.2.4	Other parameters	60
5.3	Explanations of supercooled liquid water effects on PD and TB	61
5.3.1	With or without supercooled liquid water	61
5.3.2	Locations of supercooled liquid water	65
5.4	Conclusions and remaining uncertainties	69
5.5	Implications of PD for snowfall retrievals	70
6	Potential of PD information for ice cloud detection	73
6.1	FY-4 description	73
6.2	RT simulations at FY-4 window channels	74
6.2.1	RT setup	74
6.2.2	Ice particles with horizontal orientation	76
6.2.3	Ice particles with canting angles	78
6.3	Conclusions	80
7	Summary and outlook	85
	List of acronyms	89
	List of symbols	91
	Bibliography	93

Chapter 1

Introduction

Ice clouds which regularly cover at least 20% of the globe profoundly affect global weather and climate systems (*Liou, 1986; Wylie et al., 1994*). They play an important role in the energy budget of the earth-atmosphere system, since ice clouds can reflect short and long wave radiation and emit long wave thermal radiation to the earth-atmosphere system (*Liou, 1986*). The net radiation effect caused by ice clouds strongly depends on their radiative properties, such as, spacial distribution, ice water content, microphysical properties of ice particle, etc. (*Buehler et al., 2007*). Thick ice clouds, which are regarded to be associated with frozen precipitation (e.g., falling snow), are quite important for energy and water transfers between the earth and the atmosphere. The typical high albedo of snow cover on the surface reflects solar radiances back to the atmosphere and warms the surface air temperature (the so-called “snow-albedo feedback”) (*Armstrong and Brun, 2008*). The frozen precipitation which originates from ice clouds transports water between the earth and the atmosphere is an important component in hydrological cycle of the globe.

The importance of ice clouds for weather and climate has been recognized in previous studies (e.g., *Buehler et al., 2007; Stephens and Kummerow, 2007; Armstrong and Brun, 2008*). However, the variable structure of ice clouds in time and space makes it extremely difficult to characterize them properly. The simplifications of microphysical properties of ice clouds give rise to substantial uncertainties in weather and climate modelings (*Protat et al., 2010*). Therefore, it becomes important to better understand and represent ice clouds in observations and models.

1.1 Motivation

Ground-based and space-/air-borne microwave radiometry has shown promising ability in ice cloud observations (e.g., *Evans et al., 2002; Kneifel et al., 2010; Skofronick-Jackson and Johnson, 2011*). Compared to visible and infrared remote sensing, microwave radiation can penetrate most clouds and thus provides an insight into vertical profiles of ice clouds. Moreover, the wavelength in the microwave spectrum is comparable to the size of the frozen hydrometeors ranging from several microns to several millimeters and the sensitivity of microwave to ice particles is considerably high (*Jiménez et al., 2007; Wu et al., 2008*). Accordingly, microwave radiometry has been recognized as one of the most efficient and important approaches to observe ice clouds (*Wang et al., 2001; Skofronick-Jackson et al., 2004; Wu et al., 2006*). The sensitivities of microwave channels to hydrometeors in the frequency range from 1 GHz

to 1000 GHz have been thoroughly investigated in previous studies (e.g., *Gasiewski, 1992; Evans and Stephens, 1995b*). They showed that observations with microwave channels, especially those at higher frequencies (≥ 90 GHz), are able to derive microphysical parameters of frozen hydrometeors.

Ice particles occur in clouds when the temperature is below 0°C , and the probability of ice particles being present increases as the temperature decreases (*Wallace and Hobbs, 2006*). Frozen hydrometeors can grow at the expense of water vapor in the vicinity. When ice particles collide with water droplets or ice particles, their growth by aggregation or riming makes their shapes more irregular (*Wallace and Hobbs, 2006*). Observations show that ice clouds are composed of a large number of nonspherical frozen hydrometeors. Common crystal types in ice clouds are predominantly categorized into be platelike, columnlike and irregular ice particles (*Heymsfield, 1972; Noel and Sassen, 2005*).

The knowledge on the microphysics of ice clouds is still limited. The oversimplifications of ice cloud microphysics in models produce significant uncertainties in the meteorological and climatological studies (*Kim et al., 2008; Protat et al., 2010*). Specially, the orientation of frozen hydrometeors is one of the important components which pose significant impact in the retrievals. Most analysis on ice clouds, either in radiative transfer models or retrieval algorithms, assumed that frozen hydrometeors are spherical or randomly oriented (*Evans et al., 2005; Grecu and Olson, 2008; Kim et al., 2008; Kneifel et al., 2010*). The study by *Ono (1969)* suggested that ice crystals in clouds tend to fall with their maximum dimension parallel to the ground. Pristine ice particles have been found to fall with their largest dimension horizontally oriented (*Pruppacher and Klett, 1997*). In the past decades, observations in the visible and near infrared spectral range have verified that ice particles have preferential orientation (*Chepfer et al., 1999; Noel and Chepfer, 2004; Noel and Sassen, 2005*). However, for large particles, it becomes difficult to define their preferential orientation, especially for frozen hydrometeors with complex habit, e.g., aggregates. Their orientation also increasingly depends on the local aerodynamic conditions.

Thus, it is still unclear,

- whether frozen particles in ice clouds and during precipitation are orientated or not,
- to which extent they can cause polarization signals in ground-based and space-/air-borne observations if frozen hydrometeors are oriented,
- how polarized signals improve ice cloud retrievals when ice particles produce significant polarization signatures during their falling process.

In order to solve these specific questions concerning ice particle orientation, ground-based polarization observations have been conducted at “Umweltforschungsstation Schneefernerhaus” (UFS) in Germany, by means of a dual polarized microwave radiometer at the frequency of 150 GHz (*Löhnert et al., 2011*). UFS on Mount Zugspitze offers a unique perspective for the observations of ice clouds and snow precipitation. It is located at 2650 m above mean sea level (MSL) and the occurrences of snow events are much more frequent, comparing to observation sites at lower altitudes. The polarization observations at UFS are dedicated to gain insight into the polarization signatures originating from oriented frozen hydrometeors. The study aims to investigate the potential role of the polarization signatures caused by orientated frozen particles in determining their microphysical parameters.

The unique study on polarization observations may further promote the design of new space-borne instruments for ice cloud observations. In contrast to ground-based remote sensing, observations from space require much lighter but more reliable instruments. It is unknown whether polarized channels should be aboard satellites or not, since the existence of orientated ice particles and the benefits of polarization observations have not been clarified so far. New satellite sensors at submillimeter waveband (microwave frequency ≥ 300 GHz) have been proposed for ice cloud characterization in the past few years (e.g., *Buehler, 2005*). Meanwhile, in China a second generation of geosynchronous satellite FengYun-4 (FY-4) also aims at ice cloud observations. One of the advantages of space-/air-borne remote sensing is that, the surface contribution is negligible due to the strong absorption of water vapor near the surface, especially in the so-called submillimeter-wave spectrum. Thus, observations from space at high frequencies have significant contributions from ice clouds. The analysis on polarization observations could be valuable for the retrievals of ice clouds. The polarization information provided by oriented frozen hydrometeors will be determinative for the additional polarization channels of space-borne instruments.

1.2 State-of-the-art

1.2.1 Microwave remote sensing of frozen hydrometeors

Because of the important role of ice clouds in energy budget and hydrological cycle of the earth-atmosphere system, there is an increasing interest in retrieving ice clouds (*Evans and Evans, 1999; Buehler et al., 2007*). To develop retrieval algorithms, it is crucial to understand the radiative interactions in the atmosphere which physically relates the observations to physical properties of ice clouds.

The basic principle of radiative interaction in the atmosphere can be described as follow. In the presence of scattering (absorbing) medium in the atmosphere, the radiation propagating through the medium is scattered (absorbed and re-emitted) to all directions. For liquid-phased hydrometeors, their emission effects dominate the observed radiances by microwave radiometers (*Battaglia and Simmer, 2007*), while the scattering effects are the predominant process for frozen hydrometeors, like ice and snow particles, especially at high microwave frequencies (*Gasiewski, 1992; Evans and Stephens, 1995a; Noh, 2006*). From the ground-based perspective, the scattering/absorption effects of clouds and precipitating hydrometeors enhance the radiances received by upward looking instruments below the atmospheric medium, while they reduce the observed radiance for downward viewing sensors which are located above the medium. The magnitude of the received radiances strongly depends on the radiative characteristics of ice clouds and precipitation systems (e.g., *Bennartz and Petty, 2001; Kim et al., 2008*). Therefore, the observation which results from scattering/absorption processes is employed to derive the microphysical properties of clouds and precipitation, e.g., ice water path (IWP) and particle effective size, either from ground-based or space-borne instruments (e.g., *Greco and Olson, 2008; Kim et al., 2008; Defer et al., 2008*). Moreover, while microwaves can probe clouds with high IWP, visible and infrared waves are saturated within the clouds. Since microwave observations are generally sensitive to hydrometeors especially at high frequencies, they are applicable to detect the vertical structure of ice clouds (*Cordisco et al., 2006; Noh, 2006*).

The weak signals at microwave frequencies lower than 90 GHz make observations of frozen hydrometeors move to a higher frequency. Considering small crystals in high level ice clouds,

the submillimeter-wave cloud ice radiometer (SWCIR) developed by the Jet Propulsion Laboratory (JPL) was designed for ice cloud observations with channel frequencies up to 643 GHz. The accuracy of the employed retrieval algorithm is assumed to be $\sim 30\%$ for the integrated ice amount and $\sim 15\%$ for the median mass equivalent sphere diameter (*Evans et al.*, 2002). The compact scanning submillimeter imaging radiometer (CoSSIR) was first deployed for the regional study of tropical anvils and cirrus layers Florida area cirrus experiment (CRYSTAL-FACE) in 2002 (*Evans et al.*, 2005). The observations of CoSSIR in CRYSTAL FACE verified that submillimeter-wave channels have higher sensitivity to ice particle size, compared to the lower frequencies. Another submillimeter-wave instrument for ice cloud measurements has been recently proposed by *Buehler* (2005): the cloud ice water path submillimetre imaging radiometer (CIWSIR). Theoretically, the CIWSIR could retrieve the IWP with an accuracy of $\sim 20\%$ and the median mass equivalent sphere diameter with an accuracy of $\sim 30 \mu\text{m}$ (*Buehler et al.*, 2007). From an active perspective, the observations from the Cloud-Sat satellite carrying with a 94 GHz radar (*Stephens et al.*, 2002) and the Cloud-Aerosol Lidar and Infrared Pathfinder Satellite Observation (CALIPSO) (*Winker et al.*, 2010) provide important information for retrieving the microphysical properties of ice clouds (e.g., *Delanoë and Hogan*, 2010).

Going on to thick ice clouds, these clouds are usually associated with precipitation processes, like falling snow. Radar provides valuable information on these clouds as well as on thin ice clouds. They were used to characterize frozen hydrometeors (e.g., *Hogan et al.*, 2006; *Matrosov*, 2007). The amount of radiance scattered backwards from ice hydrometeors depends on their microphysical properties, i.e., size distribution, particle size, shape, density, composition and orientation (*Collier*, 1989). Some microphysical parameters of frozen hydrometeors, like precipitation rate and ice water content (IWC), have been predicted based on the radar reflectivity in previous studies (e.g., *Hogan et al.*, 2006; *Matrosov*, 2007; *Greco and Olson*, 2008; *Hogan et al.*, 2012). However, the variability of microphysical properties of frozen hydrometeors in ice clouds and during precipitation results in significant variations in the relations between the radar reflectivity and precipitation rate (*Levizzani et al.*, 2011).

Synthesizing observations of active and passive microwave remote sensing shows noticeable performance in frozen hydrometeor retrievals (*Greco and Olson*, 2008; *Kim et al.*, 2008). Using the Bayesian retrieval algorithm associated with advanced microwave sounder unit-B (AMSU-B) observations, *Kim et al.* (2008) reported that the retrieved snowfall rate was consistent with the radar measurements. The retrieval algorithm which combined the radar data with the microwave radiometer measurements showed its application to the actual observations, although the estimation on the microphysics of frozen hydrometeors can cause a bias in the retrieval (*Greco and Olson*, 2008).

The accuracy of retrieval algorithms are all associated with the necessary assumptions on microphysical parameters of frozen particles, both for passive and active remote sensing. Realistic representation of frozen particles in models could be of peculiar help to improve the accuracy of retrievals. The vertical structure of frozen hydrometeors is also required in order to quantify ice clouds (*Levizzani et al.*, 2011). However, on the one hand, the complex microphysics of frozen hydrometeors make it difficult to model them accurately. On the other hand, the lack of information on their microphysics greatly hamper the accuracy of ice cloud retrievals. No observations can offer enough information to retrieve all the parameters. Therefore, an optimization of microphysical parameters of frozen hydrometeors are necessary to improve the retrieval algorithms.

In the following, microphysical properties of ice clouds, which have significant impact on radiative properties of frozen hydrometeors, are addressed on the basis of the present studies.

Ice permittivity

The complex permittivity of pure ice, which depends on many factors, is one of the determinative factors for ice scattering properties, and it is difficult to obtain the true value of permittivity of ice particles in clouds. *Jiang and Wu* (2004) updated Hufford's model (*Hufford*, 1991) for radiative transfer calculations for microwave limb sounders (MLS). They found that the uncertainties in the real and imaginary parts of ice permittivity result in errors in extinction coefficients and single scattering albedo at a typical particle size at the upper atmosphere research satellite (UARS) and earth observing system (EOS) MLS radiometer frequencies (*Jiang and Wu*, 2004). Employing another model for ice permittivity (*Mätzler and Wegmüller*, 1987), *Kim* (2004) calculated the extinction and absorption cross sections and asymmetry factors for spherical crystals, based on 20% uncertainty in the imaginary part of complex permittivity. The uncertainties of ice permittivity lead to a 3% uncertainty in both extinction efficiencies and asymmetry factors, for size parameters less than 12 at the frequency of 340 GHz. An uncertainty of 5% in the real part of permittivity resulted in more than 5% mean deviations in both scattering and extinction efficiencies, especially significant at high frequencies (183 GHz). The absolute variations of the emerging brightness temperature (TB) from ice clouds due to uncertainties in the permittivity were found to be more than 1 K (*Xie et al.*, 2009).

Ice particle shape

Traditionally, hydrometeors are assumed to be spherical in radiative transfer models and retrievals (e.g., *Skofronick-Jackson et al.*, 2002; *Evans et al.*, 2005). Studies begin to treat ice particles with more realistic shapes in the past years, like columns, plates and aggregates (*Kim et al.*, 2008; *Kneifel et al.*, 2010), since scattering properties of nonspherical ice particles can be calculated by solving the electromagnetic equations (*Draine and Flatau*, 1994; *Yang and Liou*, 1996; *Bohren and Huffman*, 1998; *Mishchenko et al.*, 2002). Databases for single scattering properties of randomly oriented particles are available (e.g., *Liu*, 2008; *Hong et al.*, 2009). The effect of nonspherical habits on radiance is further investigated, e.g., *Bennartz and Petty* (2001); *Kneifel et al.* (2010). Varying ice particles, from dendrites to bullet aggregates, brings forth differences of TB on the order of 20 K at 150 GHz (*Kneifel et al.*, 2010).

Ice particle mass size relationship

The different particle densities lead to different particle mass size relationships, and further results in different relations between IWC and radar reflectivity (e.g., *Brown and Francis*, 1995; *Matrosov*, 2007; *Heymsfield et al.*, 2010). Radar reflectivity and precipitation rate relations are found to vary with temperature, since the riming process during snowfall potentially changes the mass size relationships (*Matrosov*, 2007). Assuming ice-air mixed oblates, *Hogan et al.* (2012) compared two different mass size relationship of ice particles, i.e., *Brown and Francis* (1995) and *Heymsfield et al.* (2010), and they found that the high particle density results in an overestimation of IWC retrieved from radar reflectivity.

Ice particle size spectrum

It was shown that the hydrometeors sizes follow an exponential size distribution (*Marshall and Palmer*, 1948; *Field et al.*, 2005). *Field et al.* (2005) proposed a universal size distribution of ice particles based on aircraft measurements. They expressed intercept parameter in size spectra

as a function of the atmospheric temperature. The variability in ice particle size spectrum leads to considerable uncertainties in passive and active remote sensing (*Hogan et al.*, 2006; *Kneifel et al.*, 2010), since scattering ability of frozen hydrometeors varies with their size (e.g., *Liu*, 2008).

Supercooled liquid water in ice clouds

Significant amounts of supercooled liquid water were frequently found in ice cloud observations, even at very low temperatures (*Löhnert et al.*, 2011). The emission of supercooled liquid water has an impact on the observed radiances, especially at high frequencies. However, the radiative properties of supercooled liquid water is not completely understood due to the lack of laboratory measurements of its refractive index (*Mätzler et al.*, 2010; *Cadeddu*, 2011). This makes ice cloud retrievals much more difficult when ice particles coexist with supercooled liquid water (*Levizzani et al.*, 2011).

Ice particle orientation

So far, ice particles are assumed to be randomly oriented in most studies. However, the preferential orientation enhances the scattering effects of frozen hydrometeors. Therefore it affects the brightness temperature depression (*Xie and Miao*, 2011) and enhances radar reflectivity (*Sun et al.*, 2011). Meanwhile, from the passive perspective, oriented frozen hydrometeors result in TB difference between the vertical and horizontal polarizations (e.g., (*Evans and Stephens*, 1995*b*)). Thus, RT simulations were done to investigate the potential of polarization observations from space for ice cloud characterization (*Miao et al.*, 2003; *Xie and Miao*, 2011). By active remote sensing of frozen hydrometeors, *Matrosov* (2007) and *Hogan et al.* (2012) found that oriented oblates give better approximations for radar observations than particles with radome orientation.

In contrast to randomly oriented particles, the scattering properties of oriented ice particles, as well as the polarization of the scattered radiation, vary with the incident and scattered directions (*Yang et al.*, 2011). Numerous methods have been developed to calculate scattering characteristics of perfectly or partially oriented nonspherical particles, e.g., *Mishchenko* (2000). Scattering calculations for oriented ice particles are rare because their orientation is still an open issue, especially for aggregated or rimed particles. With the T-matrix method (*Mishchenko*, 2000; *Mishchenko et al.*, 2002) and other numerical algorithms (*Kahnert*, 2003), e.g., the discrete dipole approximation (DDA) algorithm (*Draine and Flatau*, 1994; *Yurkin and Hoekstra*, 2007) and finite-difference time domain method (FDTD) (*Yang and Liou*, 1996), scattering properties of oriented snow particles can be calculated principally, though there are still some limitations. The T-matrix method can be used only for particles with a rotational symmetry around a defined axis (*Mishchenko et al.*, 2002), e.g., columns, oblates and Chebyshev particles. The DDA and FDTD methods can be used to calculate scattering characteristics of particles with an arbitrary shape. However, the algorithm is computationally expensive, especially for larger particles at the microwave band (*Kahnert*, 2003; *Draine and Flatau*, 2004).

1.2.2 Polarization radiation observed by microwave radiometers

It is known that frozen hydrometeors with preferential orientation have strong dichroism effects which cause polarization difference (PD) between the horizontal and vertical polarizations (e.g., *Evans and Stephens*, 1995*b*; *Miao et al.*, 2003). *Davis et al.* (2005) obtained the

polarized signals in cirrus clouds at 122 GHz. However, as described above, frozen hydrometeors have been assumed to be spherical or randomly-oriented in RT models and retrieval algorithms for decades, and radiation emerging from clouds is considered to be unpolarized (e.g., *Evans et al.*, 2005; *Kim et al.*, 2008; *Kneifel et al.*, 2010). On the one hand, this is for simplification in the models; on the other hand, the orientation of frozen hydrometeors is unknown.

The studies on radiative properties of the atmosphere show that the observed polarization signature, either from ground or space, could originate from three processes: (a) dichroic emission from liquid hydrometeors (e.g., water drops) or surface (e.g., sea surface), (b) polarized/unpolarized radiation propagating through the dichroic medium, (c) scattering effects of frozen hydrometeors (*Kutuza et al.*, 1998; *Battaglia et al.*, 2006). Later simulations on polarization signals found that nonspherical particles, especially those with preferential orientation have strong dichroism effects and can result in significant PDs (e.g., *Evans and Stephens*, 1995b; *Czekala and Simmer*, 1998; *Czekala et al.*, 1999).

Polarization signature caused by liquid precipitation has been found in previous observations. *Spencer et al.* (1983) observed significant polarization signatures with the scanning multichannel microwave radiometer (SMMR) in storms. However, they later attributed the polarization signature observed from SSM/I to the instrument intrinsic bias, and re-calibrated the polarized signals for the observation data (*Spencer et al.*, 1989). The study conducted by *Heymsfield and Fulton* (1994) showed lower polarization signals over the convective regions rather than the stratiform regions, using SSM/I observations at the frequency of 85 GHz. In addition, they found that the horizontal channel was cooler in the midlatitude region than in the tropical area. Ground-based polarization measurements showed that the PD between the two orthogonal polarizations reaches 10 K in rain events at microwave frequencies, and further confirmed the existence of PDs during rainfall (*Kutuza et al.*, 1998; *Czekala et al.*, 2001b; *Battaglia et al.*, 2009).

To evaluate polarization measurements, polarized radiative transfer models were developed (e.g., *Wu and Weinman*, 1984; *Evans and Vivekanandan*, 1990; *Roberti and Kummerow*, 1999). The polarization phenomenon observed by microwave radiometers can not be interpreted if only spherical particles are assumed in polarized radiative transfer models (*Wu and Weinman*, 1984; *Czekala and Simmer*, 1998). *Wu and Weinman* (1984) calculated the vertical and horizontal radiances emerging from precipitating clouds and their results showed that TBs are remarkably depressed by precipitation when observed from space. However, the difference between horizontal and vertical radiances is less than 1 K for spherical particles and deformed water drops at frequencies up to 37 GHz, while the PD value drastically increases for nonspherical particles, up to 10 K. The related studies on polarization signature, where the simulations were set up with the assumptions of nonspherical particles, were reviewed by *Haferman* (2000). The simulation results during liquid precipitation quantified the effects of particle orientation on polarized microwave radiances at the SSM/I frequencies (*Prigent et al.*, 2001, 2005).

It has been found that in mixed-phased clouds and during rain precipitation, particles tend to be horizontally aligned and this results in significant polarized signals from the ground-based and space-borne observations at microwave band (*Heymsfield and Fulton*, 1994; *Czekala et al.*, 2001b; *Troitsky et al.*, 2003). *Czekala et al.* (2001a) developed a new algorithm to distinct rain drops from cloud droplets. They proposed to use the combination of PD and TB in the new retrieval algorithm, on the basis of the different scattering properties of particles with respect to size. The polarization signatures during rainfall were further

proven to be helpful to distinguish cloud liquid water from rain drops with the advanced microwave radiometer for rain identification (ADMIRARI) (*Battaglia et al., 2009*). Furthermore, a ground-based microwave radiometry observed significant polarized signals in mixed phase clouds (*Troitsky et al., 2003*).

Although most emphasis has been put on polarization observations of rainfall and mixed-phased cloud systems (e.g., *Czekala et al., 2001b; Prigent et al., 2001; Troitsky et al., 2003; Battaglia et al., 2009*), there are few observations concerning orientations of frozen hydrometeors, even though ice particles with preferential orientation affect the radiances received by active and passive instruments (*Sun et al., 2011; Xie and Miao, 2011*). Microwave remote sensing, either from space or ground, can provide long term observations to assess microphysical parameters of ice clouds and the related precipitation systems. However, very few analysis are performed to quantify the effects of oriented frozen hydrometeors in RT simulations.

1.3 Focus of the study

To provide a deep insight into the orientation of frozen hydrometeors and the polarization signature caused by their preferential orientation, ground-based polarization observations are carried out during snowfall at UFS on Mount Zugspitze in Germany. The dual-polarized microwave radiometer (DPR) provides polarized signature at 150 GHz during snowfall. By means of the synergy of instruments deployed at UFS, other remote sensing techniques have been employed to fully exploit the information content on polarization signatures in snow events. This study is not only important for the potential use of polarization observations for snowfall retrievals, but also for the promotion of the new instrument design. Whether polarized channels will be deployed on future space-borne satellites will be strongly dependent on the information content obtained from polarization.

This study therefore aims at the investigation of polarization signals caused by frozen hydrometeors. It will aim to answer the questions which focus on frozen hydrometeors:

- Do frozen hydrometeors have preferred orientation, especially during their falling process?
- If snow particles are oriented, what is their preferred orientation? And how large are polarized signals received by instruments from space and ground?
- What in the ice clouds can affect the PD resulting from oriented ice particles, their own microphysical properties, or/and some other factors?
- Can polarization signature benefit ice cloud retrievals, if space/air-borne or ground-based instruments are equipped with two orthogonal polarizations?

For these purposes, the study is structured as follows: Chapter 2 briefly describes the basic radiative terminology and radiative interaction in the atmosphere. A polarized radiative transfer model and the algorithms for scattering radiative properties of the scattering medium are also described in Chapter 2. In Chapter 3, the dual polarized microwave radiometer, together with the auxiliary synergic instruments deployed at UFS, are introduced for the observations of snowfall. The data set for snowfall in the whole year 2010 is illustrated with the correction for the polarization bias (Chapter 3). The observation results conducted by the instruments at UFS are analyzed in Chapter 4: first a single snow case is shown and then the complete data set of 458-hour snowfall in 2010 is analyzed. With the auxiliary

observations at the summit of Mount Zugspitze, Chapter 4 discusses the effects of atmospheric conditions on polarization signals. By means of radiative transfer calculations, Chapter 5 verifies the polarization observations presented in Chapter 4 and evaluates the effects of snow water path (SWP) and liquid water path (LWP) on PD and TB. After that, Chapter 5 examines the sensitivity of snow microphysical parameters to TB and PD, assuming a varying density of frozen hydrometeors, their sizes and orientations, etc. Followed by the analysis on polarization implications for snowfall retrievals, the effects of the frequently present liquid water on TB and polarized signals are explained by a simple physical model in Chapter 5. The potential of polarized signatures for ice cloud characterization is investigated in Chapter 6 to promote the new space-borne instruments and to investigate the benefits of polarization observations. Finally, the summary of the work, along with an outlook for future study, is given in Chapter 7.

Parts of the work presented in this thesis, which analyze the polarization observations during snowfall at UFS, were recently published in the following paper:

- Xie, X., U. Löhnert, S. Kneifel, and S. Crewell, Snow particle orientation observed by ground-based microwave radiometry, *Journal of Geophysical Research*, 117, D02206, doi:10.1029/2011JD016369, 2012.

The simulations of the potential polarization signature in ice cloud systems, as analyzed in Chapter 6, has been published in:

- Xie, X. and J. Miao, Polarization difference due to nonrandomly oriented ice particles at millimeter/submillimeter waveband, *Journal of Quantitative Spectroscopy and Radiative Transfer*, 112, 1090-1098, doi:10.1016/j.jqsrt.2010.11.020, 2011.

Chapter 2

Methodology

Radiative transfer theory is a powerful tool, which is widely used in the research field of atmospheric radiation and remote sensing to understand the interaction of the solar and terrestrial radiation with the atmosphere and further to infer microphysical parameters of gaseous molecules, aerosols and cloud particles in the atmosphere. A radiative transfer model is a necessity in order to achieve these goals (*Liou, 2002; Petty, 2006*). The complex radiation interaction in the atmosphere (*Bohren and Huffman, 1998; Mishchenko et al., 2002*), i.e., the scattering and absorption of the atmosphere, also needs to be investigated. In the following, a polarized radiative transfer model which deals with the scattering atmosphere with a plane-parallel and azimuthally-symmetric geometry will be introduced.

2.1 Definition of terminology in radiative transfer

2.1.1 Basic radiative parameters

The radiative intensity (henceforth called intensity) is the radiant energy dE traveling in a particular solid angle $d\Omega$ in a time duration dt in a wavelength interval $d\lambda$ on an effective area dA_e . It can be expressed as a differential of radiant energy with respect to time, solid angle, effective area and wavelength,

$$I_\lambda = \frac{dE}{dt d\Omega dA_e d\lambda} \quad (2.1)$$

where the effective area A_e is the surface area normal to the propagation direction of the radiant energy.

The intensity emitted by a blackbody is closely associated with its physical temperature according to Planck's law (Equation 2.2). A blackbody is an idealized object with its emissivity equal to 1, i.e., the intensity absorbed by the blackbody at all wavelengths is equal to its emitted intensity that covers the entire electromagnetic spectrum.

$$B_\lambda = \frac{2hc^2}{\lambda^5} \left(\frac{1}{e^{hc/\lambda k_B T} - 1} \right) \quad (2.2)$$

where B_λ (in $\text{W m}^{-2}\text{m}^{-1}\text{sr}^{-1}$) is the emitted intensity by the blackbody, $h = 6.626 \times 10^{-34}$ (in J·s) is the Planck constant, $k_B = 1.381 \times 10^{-23}$ (in J/K) is the Boltzmann constant, λ (in m) is the wavelength, T (in K) is the temperature of the blackbody and $c = 2.998 \times 10^8$ (in m/s) is speed of light.

2.1.2 Polarization and Stokes parameters

A plane monochromatic wave with an electric field \mathbf{E} propagates in the direction of \hat{n} in a non-absorbing medium (Figure 2.1). The electric field \mathbf{E} can be mathematically written as the superposition of two perpendicular electric field vectors, \mathbf{E}_h and \mathbf{E}_v , which oscillate respectively in the directions of \hat{h} and \hat{v} (Equation 2.3). Along the propagation direction \hat{n} of the beam, the component is equal to zero due to the non-absorbing medium. Thus, the electric wave can be expressed as

$$\begin{aligned}\mathbf{E}(\mathbf{r}, t) &= \text{Re}\{(\mathbf{E}_h + \mathbf{E}_v) \exp(ik\hat{n} \cdot \mathbf{r} - i\omega t)\} \\ &= \text{Re}\{(E_{0h}\hat{h} + E_{0v}\hat{v}) \exp(ik\hat{n} \cdot \mathbf{r} - i\omega t)\} \\ &= E_h\hat{h} \cos(k\hat{n} \cdot \mathbf{r} - \omega t + \Delta_h) + E_v\hat{v} \cos(k\hat{n} \cdot \mathbf{r} - \omega t + \Delta_v)\end{aligned}\quad (2.3)$$

with

$$\begin{aligned}E_{0h} &= E_h \exp(i\Delta_h) \\ E_{0v} &= E_v \exp(i\Delta_v)\end{aligned}\quad (2.4)$$

where E_{0h} and E_{0v} are the two complex amplitudes of the two electric field vectors, E_h and E_v are the amplitudes of the two independent components, the unit vectors \hat{h} and \hat{v} indicate the oscillating directions of the electric field, Δ_h and Δ_v are the phases of the two complex amplitudes, ω is the angular frequency of the wave, $k = 2\pi/\lambda$ (in m^{-1}) is the wave number with wavelength λ , and $\hat{n} \cdot \mathbf{r}$ (in m) specifies the distance of the wave propagating in the direction \hat{n} .

The polarization state of the electromagnetic wave is determined by the amplitudes and the relative phase $\Delta_{v-h} = \Delta_v - \Delta_h$ of the two components \mathbf{E}_h and \mathbf{E}_v . If either of the two components (either \mathbf{E}_h or \mathbf{E}_v) in Equation 2.3, is equal to zero, the wave is said to be linearly polarized (horizontally or vertically polarized). The wave is also linearly polarized when the relative phase Δ_{v-h} between the two components is zero and the two components are in phase. When the two orthogonal components have the same amplitude and the relative phase is equal to $\pm\pi/2$, this kind of polarization is called circular polarization. When either the relative phase is not zero or $\pm\pi/2$, or the two components do not have the same amplitude, the electromagnetic wave is therefore not linearly or circularly polarized. In this case it is called elliptically polarized. Besides the electric field vectors, the Stokes vector $\vec{\mathbf{I}}$ is also introduced to describe the polarization state of the beam (*Stokes*, 1852; *Bohren and Huffman*, 1998; *Liou*, 2002; *Mishchenko et al.*, 2002). The four Stokes parameters I , Q , U and V of the Stokes vector $\vec{\mathbf{I}}$ are defined as follows,

$$\vec{\mathbf{I}} = \begin{bmatrix} I \\ Q \\ U \\ V \end{bmatrix} = \begin{bmatrix} E_{0v}E_{0v}^* + E_{0h}E_{0h}^* \\ E_{0v}E_{0v}^* - E_{0h}E_{0h}^* \\ -E_{0v}E_{0h}^* - E_{0h}E_{0v}^* \\ i(E_{0h}E_{0v}^* - E_{0v}E_{0h}^*) \end{bmatrix}\quad (2.5)$$

where the asterisk $*$ denotes the complex conjugation operation, i is the imaginary unit, and E_{0v} and E_{0h} are the two complex amplitudes of the wave as given in Equation 2.4. Note that a constant factor $\frac{1}{2}\sqrt{\frac{\epsilon_0}{\mu_0}}$ is omitted in Equation 2.5, where ϵ_0 is the permittivity and μ_0 is the magnetic permeability.

The four Stokes parameters can be also derived by the two amplitudes (E_v and E_h) of the electric fields and the relative phase ($\Delta_{v-h} = \Delta_v - \Delta_h$) between the two electric field vectors

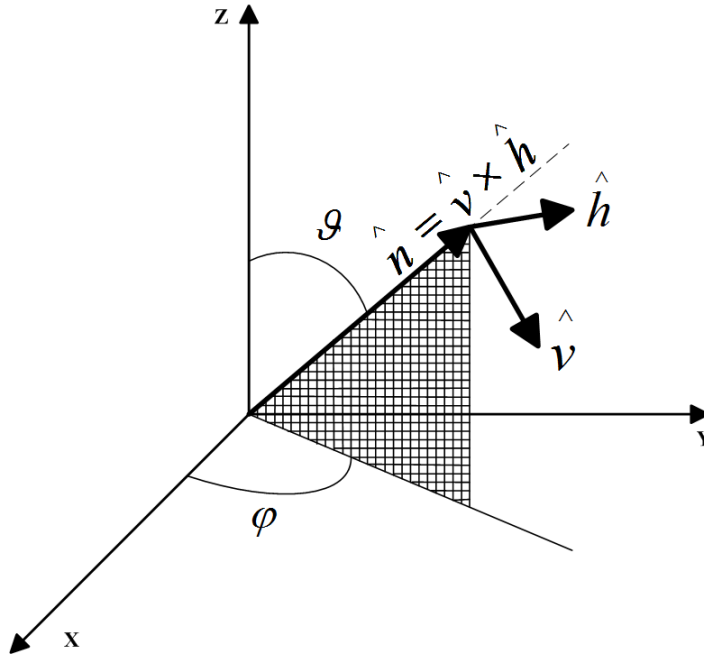


Figure 2.1: Coordinate system used to describe the propagation direction and the polarization state of a plane electromagnetic wave. The unit vector \hat{n} , which indicates the propagation direction of the wave, is specified by the zenith and azimuth angles (ϑ , φ) in the coordinate system. The unit vector \hat{v} , which is in the meridional plane specified by \hat{n} , indicates the direction of the vertical electric field vector (vertical polarization), and the unit vector \hat{h} perpendicular to the meridional plane shows the horizontal component (horizontal polarization). (From *Mishchenko et al.*, 2002)

\mathbf{E}_v and \mathbf{E}_h , by means of Equations 2.3 – 2.5. The Stokes parameters I , Q , U and V therefore can be rewritten as

$$\begin{aligned}
 I &= E_v^2 + E_h^2 \\
 Q &= E_v^2 - E_h^2 \\
 U &= -2E_v E_h \cos \Delta_{v-h} \\
 V &= 2E_v E_h \sin \Delta_{v-h}
 \end{aligned} \tag{2.6}$$

The Stokes parameters I and Q are also usually expressed by the intensities at the vertical and horizontal polarizations, I_v and I_h , respectively.

$$\begin{aligned}
 I &= I_v + I_h \\
 Q &= I_v - I_h
 \end{aligned} \tag{2.7}$$

To show how the Stokes vector $\vec{\mathbf{I}}$ can express the polarization state of an electromagnetic wave, an elliptically polarized wave is assumed in Figure 2.2. The ellipticity of the elliptically polarized wave, i.e., the ratio of the minor axes to the major axis, is specified by $|\tan \eta|$. The propagation direction of the wave, determined by the relation $\hat{n} = \hat{v} \times \hat{h}$ denoted in Figure 2.1, is perpendicular to the $\hat{h} - \hat{v}$ plane and towards the reader. When the electric field vector rotates clockwise as viewed by the observer looking towards the propagation direction of the wave, η is positive and the polarization of the wave is thus called right-handed, as shown

in Figure 2.2. The counterclockwise rotation of the electric field vector results in a negative η and a left-handed polarization, if looking towards the propagation direction of the beam. The components of the wave in the horizontal and vertical directions can be expressed by the angle ζ which is defined by rotating the unit vector \hat{h} clockwise around the origin O to the major axis of the wave, when looking in the propagation direction of the wave. The Stokes parameters of the wave I , Q , U , and V are therefore derived as a function of the angle η and ζ as follows,

$$\begin{aligned}
 I &= I \\
 Q &= -I \cos 2\eta \cos 2\zeta \\
 U &= I \cos 2\eta \sin 2\zeta \\
 V &= -I \sin 2\eta
 \end{aligned} \tag{2.8}$$

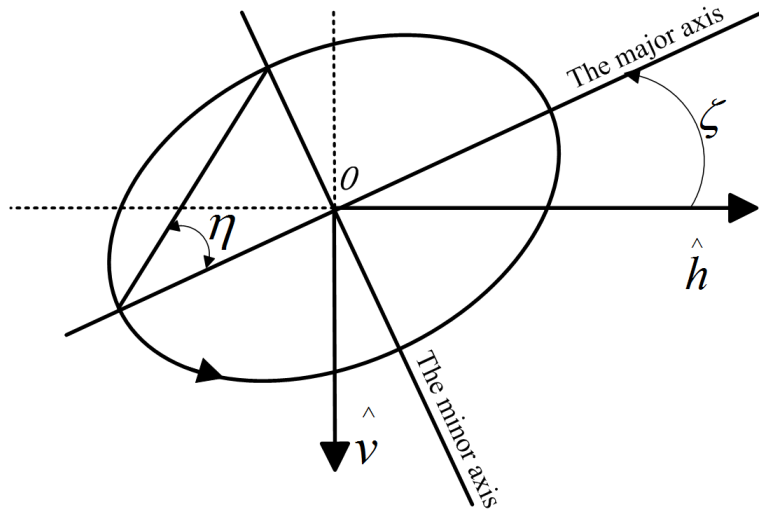


Figure 2.2: The polarization state of an elliptically-polarized wave. The wave propagates towards the reader and normal to the $\hat{h} - \hat{v}$ plane according to the relation $\hat{n} = \hat{v} \times \hat{h}$. (From *Mishchenko et al.*, 2000)

According to Equation 2.8, the relation between the Stokes parameters and the parameters expressing the wave characteristics (the angle η and ζ) can be given as

$$\begin{aligned}
 \tan 2\eta &= -\frac{V}{\sqrt{Q^2 + U^2}} \\
 \tan 2\zeta &= -\frac{U}{Q}
 \end{aligned} \tag{2.9}$$

The first Stokes parameter I indicates the total intensity of the electromagnetic wave, and depends on the major and minor axes of the ellipse. The other three Stokes parameters Q , U and V specify the polarization state of the wave. As shown in Figure 2.2, if the angle η is equal to zero, the wave is linearly polarized and the Stokes parameter V also becomes zero. If the wave is right-handed polarized, η is positive and thus V is negative; and V is positive only when the wave is left-handed polarized. The Stokes parameter V is therefore associated with the degree of circular polarization, and the sign of the Stokes parameter V denotes whether the electromagnetic wave is right-handed or left-handed polarized. Hence,

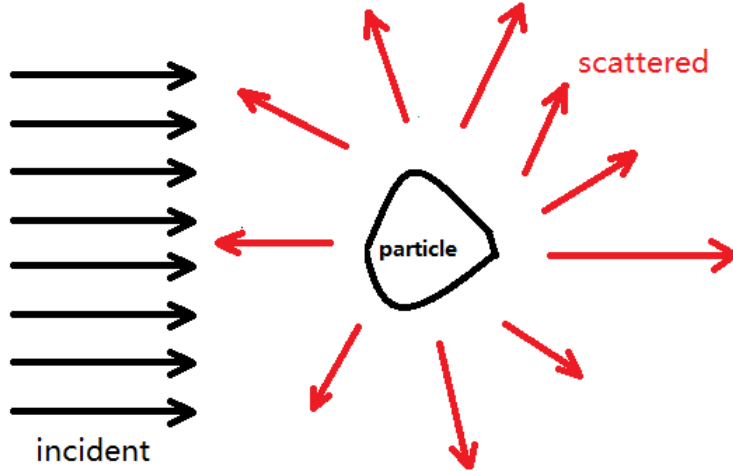


Figure 2.3: A schematic illustration of the scattering by a particle

the degree of polarization P of the wave, the degree of the linear polarization P_L , the degree of circular polarization P_C can be given as follows,

$$\begin{aligned}
 P &= \frac{\sqrt{Q^2 + U^2 + V^2}}{I} \\
 P_L &= \frac{\sqrt{Q^2 + U^2}}{I} \\
 P_C &= \frac{V}{I}
 \end{aligned} \tag{2.10}$$

For a monochromatic electromagnetic wave, its amplitude and phase are constant. However, the amplitude and phase of the wave usually vary with time, and the fluctuation frequency of these parameters is much lower than the angular frequency of the wave ω . This kind of wave is called as the quasi-monochromatic electromagnetic wave. For the quasi-monochromatic wave, the four Stokes parameters obey the relation $I^2 \geq Q^2 + U^2 + V^2$. Thus, the degree of polarization P is satisfied with the relation $P \leq 1$, and the equality holds only when the wave is fully polarized, i.e., the four Stokes parameters are satisfied with the relation $I^2 = Q^2 + U^2 + V^2$.

2.1.3 Radiation interactions in the atmosphere

When an electromagnetic wave propagates in the atmosphere, it interacts with the atmosphere. The secondary radiation due to the induced accelerated electric charges distributed in particles is called the radiation scattered by the particles (Figure 2.3). In addition to the scattered intensity, part of the incident energy is transferred into other forms, e.g., the thermal energy, and this process is called absorption. The so-called extinction is defined as the summation of radiation loss due to the scattering and absorption in the atmosphere. When

the intensity I_λ passes along a path ds , its attenuation dI_λ therefore can be expressed by

$$\begin{aligned} dI_\lambda &= \beta_{ext} I_\lambda ds \\ &= (\beta_{abs} + \beta_{sca}) I_\lambda ds \end{aligned} \quad (2.11)$$

where β_{ext} (in m^{-1}) is the extinction coefficient of the medium, β_{abs} (in m^{-1}) is the absorption coefficient, and β_{sca} (in m^{-1}) is the scattering coefficient. β_{ext} (β_{abs} or β_{sca}), which depends on wavelengths and radiative characteristics of the medium (e.g., water drops, gaseous molecules, etc.), is the summed extinction (absorption or scattering) cross sections of individual atmospheric particles C_{ext} (C_{abs} or C_{sca} , in m^2) in the volume. Extinction cross section C_{ext} with a dimension of an area describes the incident energy attenuated by a single particle.

$$\begin{aligned} \beta_{ext} &= \sum_i N_i C_{ext} \\ \beta_{sca} &= \sum_i N_i C_{sca} \\ \beta_{abs} &= \sum_i N_i C_{abs} \end{aligned} \quad (2.12)$$

where N_i (in m^{-3}) is the number of the particles in the volume with the same radiative characteristics. The total number of particles N in the medium is satisfied with

$$N = \sum_i N_i$$

The radiative properties of the atmosphere can be characterized by the optical depth in Equation 2.13. The optical depth is the integrated extinction coefficient over a propagation path of the incident wave.

$$\tau = \int_s \beta_{ext} ds \quad (2.13)$$

The total attenuated intensity can be expressed by $e^{-\lambda} I_\lambda$ with the optical depth τ when integrating Equation 2.11 along the path s .

Another parameter which is used to describe the radiative characteristics of the medium is its single scattering albedo ω_0 . For a single particle, ω_0 is defined as the ratio of scattering cross section to extinction cross section.

$$\omega_0 = \frac{C_{sca}}{C_{ext}} \quad (2.14)$$

When the single scattering albedo ω_0 is equal to one, scattering is the only effect that results in the extinction of the incident intensity; when ω_0 is zero, the extinction is only caused by the absorption effect. Usually at microwave band, the absorption is predominant in extinction for liquid water, while the scattering by ice particles dominates their extinction. The scattering of gaseous molecules is negligibly small and only absorption effects are considered in the microwave spectrum, since the sizes of gaseous molecules in the atmosphere are much smaller with respect to the wavelength. Therefore, the extinction due to the gaseous molecules is equal to their absorption (i.e., $\omega_0 = 0$), and makes contribution to the attenuation of the intensity in the atmosphere. Generally, the relevant absorbing gaseous species considered in the microwave spectrum are oxygen (O_2), nitrogen (N_2) and water vapor (H_2O) molecules.

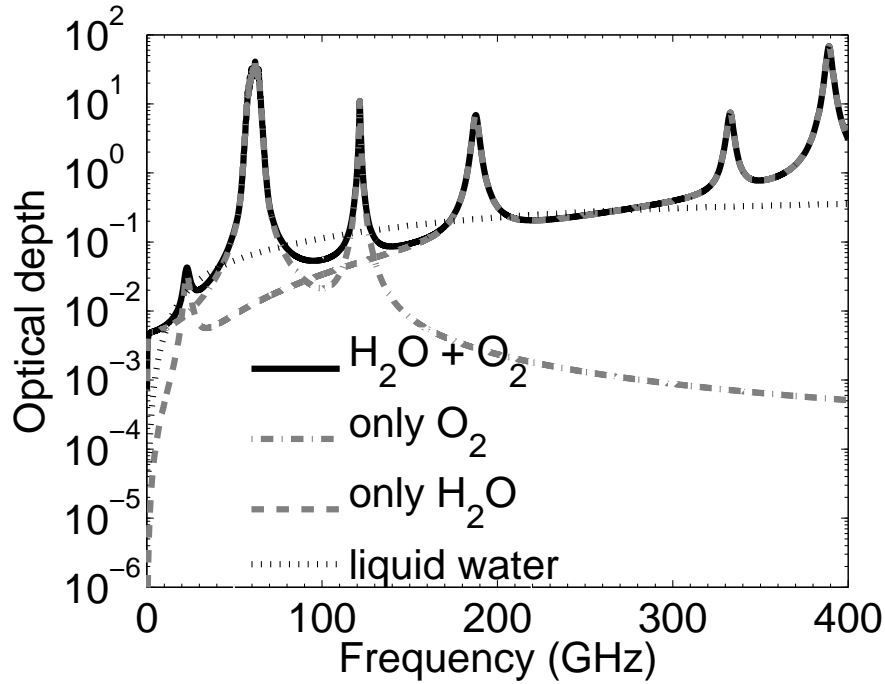


Figure 2.4: Optical depth due to the absorption of gaseous molecules in the atmosphere (winter time at mid-latitude) and due to the absorption of supercooled liquid water at the temperature of -20°C . The gray slashed-dotted line indicates the absorption due to the oxygen molecules in the atmosphere (only O_2), the gray slashed line is the absorption due to the water vapor molecules (only H_2O), the black solid line is the summation of the water vapor and oxygen absorption ($\text{H}_2\text{O}+\text{O}_2$), and the dotted line indicates the absorption due to liquid water with a liquid water path of 100 g/m^2 in the atmosphere.

The absorption of gaseous molecules in the atmosphere results from (a) the resonant absorption lines of relevant gaseous molecules and (b) the continuum absorption which does not exhibit line-like structure (e.g., *Liebe, 1989; Pardo et al., 2001*) (Figure 2.4). The absorption lines are the consequences of molecules' energy state transition, and are broadened by the Doppler effect and atmospheric pressure (*Petty, 2006*). At the lower atmosphere (troposphere and stratosphere), the pressure broadening is predominant since the dense atmosphere causes frequent collisions among the gaseous molecules and results in the broadening of absorption lines. The Doppler effect plays a more important role in the broadening of absorption lines at high altitudes. The continuum absorption has important contributions from the far-wing absorption of the water vapor lines and the collision-induced absorption of the dry air ($\text{N}_2\text{-O}_2$, $\text{O}_2\text{-N}_2$, $\text{N}_2\text{-N}_2$ and $\text{O}_2\text{-O}_2$ collisions) (*Pardo et al., 2005*). Figure 2.4 shows the optical depth due to the absorption of atmospheric gaseous molecules and the optical depth due to the absorption of supercooled liquid water in the microwave spectrum.

Besides the absorption due to gaseous molecules, the scattering by larger particles with respect to wavelength, e.g., ice particles and rain drops, becomes important in radiation interactions in the atmosphere. The electromagnetic wave propagating in the atmosphere, which can be expressed by the superposition of the vertical and horizontal electric field vectors, has already been described in Section 2.1.2. For the calculations of the scattering by particles, a 2×2 amplitude scattering matrix is then introduced, in order to link the wave scattered by a single

particle with the incident wave,

$$\begin{bmatrix} E_{0v}^{sca}(\vartheta, \varphi) \\ E_{0h}^{sca}(\vartheta, \varphi) \end{bmatrix} = \frac{e^{ikr}}{r} \begin{bmatrix} F_{vv}(\vartheta, \varphi, \vartheta', \varphi') & F_{vh}(\vartheta, \varphi, \vartheta', \varphi') \\ F_{hv}(\vartheta, \varphi, \vartheta', \varphi') & F_{hh}(\vartheta, \varphi, \vartheta', \varphi') \end{bmatrix} \begin{bmatrix} E_{0v}^{inc}(\vartheta', \varphi') \\ E_{0h}^{inc}(\vartheta', \varphi') \end{bmatrix} \quad (2.15)$$

where E_{0v}^{sca} and E_{0h}^{sca} are the complex scattered electric fields in the vertical and horizontal polarizations, respectively, E_{0v}^{inc} and E_{0h}^{inc} are the electric fields of the incident wave, (ϑ', φ') specifies the zenith and azimuth angles of the incident wave while (ϑ, φ) is the direction of the scattered wave. Note that the scattering angle ϑ is the angle between the incident and scattered wave ranging from 0° to 180° . Forward scattering ($\vartheta = 0^\circ$) has the same direction as the incidence.

The elements of the amplitude scattering matrix F_{lm} with $l = v, h$ and $m = v, h$ relate the scattered wave in the l polarization to the incident wave in the m polarization. The diagonal elements of the amplitude scattering matrix specify that the particle scatters the incident vertical (horizontal) radiance to the vertical (horizontal) polarization of the scattered wave, while the non-diagonal elements quantify the cross polarization intensity transferred from the incident wave. The amplitude scattering matrix is associated with the directions of the scattered and incident waves, and also greatly depends on the physical characteristics of particles in the atmosphere, i.e., their size with respect to wavelength, their geometry, composition and orientation. For spherical symmetric particles, the amplitude scattering matrix reduces to a 2×2 diagonal matrix and the elements F_{hv} and F_{vh} in the amplitude scattering matrix are zero.

By means of the amplitude scattering matrix in Equation 2.15, the extinction matrix \vec{K} , the scattering matrix \vec{M} and the emission vector $\vec{\sigma}$ can be derived (*Evans and Vivekanandan, 1990; Bohren and Huffman, 1998; Mishchenko et al., 2002*). The three parameters describe scattering properties of a single particle. The intensity attenuated by the scattering of the particle can be expressed by $\vec{M} \times \vec{I}^{inc}$, the extinction of the intensity is expressed by $\vec{K} \times \vec{I}^{inc}$ and the absorption of the intensity $\vec{\sigma} \times \vec{I}^{inc}$, where \vec{I}^{inc} is the Stokes vector of the incident wave.

The first element in the extinction matrix K_{11} is related to the total intensity attenuated by the particle, and the element K_{12} is often used to characterize the linear polarization of the wave. The 4×4 extinction matrix \vec{K} is defined as

$$\begin{aligned} \vec{K} &= \begin{bmatrix} K_{11} & K_{12} & K_{13} & K_{14} \\ K_{21} & K_{22} & K_{23} & K_{24} \\ K_{31} & K_{32} & K_{33} & K_{34} \\ K_{41} & K_{42} & K_{43} & K_{44} \end{bmatrix} \\ &= \begin{bmatrix} 2\pi Im(F_{vv} + F_{hh})/k & 2\pi Im(F_{vv} - F_{hh})/k & -2\pi Im(F_{vh} + F_{hv})/k & 2\pi Re(F_{hv} - F_{vh})/k \\ 2\pi Im(F_{vv} - F_{hh})/k & 2\pi Im(F_{vv} + F_{hh})/k & 2\pi Im(F_{hv} - F_{vh})/k & -2\pi Re(F_{vh} + F_{hv})/k \\ -2\pi Im(F_{vh} + F_{hv})/k & -2\pi Im(F_{hv} - F_{vh})/k & 2\pi Im(F_{vv} + F_{hh})/k & 2\pi Re(F_{vv} - F_{hh})/k \\ 2\pi Re(F_{hv} - F_{vh})/k & 2\pi Re(F_{vh} + F_{hv})/k & -2\pi Re(F_{vv} - F_{hh})/k & 2\pi Im(F_{vv} + F_{hh})/k \end{bmatrix} \end{aligned} \quad (2.16)$$

Similar to the extinction matrix, the first element of the scattering matrix M_{11} describes the total intensity scattered by the particle, and the second element M_{12} expresses the polarization status of the scattered wave in the scattering direction. The scattering matrix depends not only on the scattering direction of the wave but also on the incident direction of the wave, while the extinction matrix is only a function of the propagation direction of the incident

wave. The 4×4 scattering matrix is also called as the Mueller matrix or the phase matrix. It is expressed by

$$\vec{M} = \begin{bmatrix} M_{11} & M_{12} & M_{13} & M_{14} \\ M_{21} & M_{22} & M_{23} & M_{24} \\ M_{31} & M_{32} & M_{33} & M_{34} \\ M_{41} & M_{42} & M_{43} & M_{44} \end{bmatrix} \quad (2.17)$$

where all the elements of the scattering matrix are derived from the amplitude scattering matrix

$$\begin{aligned} M_{11} &= \frac{1}{2}(F_{vv}F_{vv}^* + F_{vh}F_{vh}^* + F_{hv}F_{hv}^* + F_{hh}F_{hh}^*) \\ M_{12} &= \frac{1}{2}(F_{vv}F_{vv}^* - F_{vh}F_{vh}^* + F_{hv}F_{hv}^* - F_{hh}F_{hh}^*) \\ M_{13} &= -Re(F_{vv}F_{vh}^* + F_{hv}F_{hh}^*) \\ M_{14} &= -Im(F_{vv}F_{vh}^* + F_{hv}F_{hh}^*) \\ M_{21} &= \frac{1}{2}(F_{vv}F_{vv}^* + F_{vh}F_{vh}^* - F_{hv}F_{hv}^* - F_{hh}F_{hh}^*) \\ M_{22} &= \frac{1}{2}(F_{vv}F_{vv}^* - F_{vh}F_{vh}^* - F_{hv}F_{hv}^* + F_{hh}F_{hh}^*) \\ M_{23} &= Re(F_{vv}F_{vh}^* - F_{hv}F_{hh}^*) \\ M_{24} &= -Im(F_{vv}F_{vh}^* - F_{hv}F_{hh}^*) \\ M_{31} &= -Re(F_{vv}F_{hv}^* + F_{vh}F_{hh}^*) \\ M_{32} &= -Re(F_{vv}F_{hv}^* - F_{hh}F_{vh}^*) \\ M_{33} &= Re(F_{vv}F_{hh}^* + F_{vh}F_{hv}^*) \\ M_{34} &= Im(F_{vv}F_{hh}^* + F_{hv}F_{vh}^*) \\ M_{41} &= -Im(F_{hv}F_{vv}^* + F_{hh}F_{vh}^*) \\ M_{42} &= -Im(F_{hv}F_{vv}^* - F_{hh}F_{vh}^*) \\ M_{43} &= Im(F_{vv}F_{hh}^* - F_{vh}F_{hv}^*) \\ M_{44} &= Re(F_{vv}F_{hh}^* - F_{vh}F_{hv}^*) \end{aligned}$$

The 4×1 emission vector is a function of the direction of the incident wave. It is associated with the radiation loss due to the absorption, which is the difference of radiation loss caused by the extinction and the scattering. It is a 4×1 vector, and can be calculated by means of the extinction matrix and scattering matrix given in Equation 2.16 and Equation 2.17, respectively. In the incident direction \hat{n} , the emission vector $\vec{\sigma}$ can be obtained when the integration of the scattering matrix in all direction is deducted from the extinction matrix in the same incident direction \hat{n} . The emission vector is given as follows, where \hat{n}' indicates the scattered direction.

$$\vec{\sigma} = \begin{bmatrix} \sigma_1(\hat{n}) \\ \sigma_2(\hat{n}) \\ \sigma_3(\hat{n}) \\ \sigma_4(\hat{n}) \end{bmatrix} = \begin{bmatrix} K_{11}(\hat{n}) - \int M_{11}(\hat{n}, \hat{n}')d\Omega' \\ K_{12}(\hat{n}) - \int M_{12}(\hat{n}, \hat{n}')d\Omega' \\ K_{13}(\hat{n}) - \int M_{13}(\hat{n}, \hat{n}')d\Omega' \\ K_{14}(\hat{n}) - \int M_{14}(\hat{n}, \hat{n}')d\Omega' \end{bmatrix} \quad (2.18)$$

When the amplitude scattering matrix is diagonal for spherically symmetric particles, eight out of the sixteen elements in the scattering matrix and the extinction matrix are set to zero. Calculations of the scattering properties for a volume of random particles will be presented later in Section 2.3.

2.2 Radiative transfer theory

2.2.1 The polarized radiative transfer equation

Suppose an atmospheric column located at the position s (Figure 2.5). The incident wave is scattered and absorbed by the atmosphere at this position s when it propagates in the atmospheric column. The change of the intensity $\vec{\mathbf{I}}(s)$ along the infinitesimal path ds in a specific direction specified by the cosine of the zenith angle μ and the azimuth angle φ has contributions from three significant processes: (a) the extinction by the atmosphere along the infinitesimal path ds (double-headed black arrow in Figure 2.5), (b) the radiation emitted by the atmosphere along the propagation path ds propagating in the direction (μ, φ) (double-headed green arrows in Figure 2.5) and (c) the intensities which come from all directions scattered into the direction (μ, φ) (double-headed red arrows in Figure 2.5).

The extinction of the wave results from the scattering and absorption effects of the atmosphere along the propagation path ds , and would become the source of scattered intensity for the adjacent volumes or be transferred to emission. The frequency of the incident wave is the same as the frequency of the scattered wave, while the emitted intensity of the particles are calculated according to the Planck's law. The incident intensity is reduced by the extinction of the atmospheric column but compensated by the scattered intensity coming from all directions and the emission of the atmospheric column. The change of the incident intensity, which is caused by the presence of the medium in the atmosphere, therefore can be expressed by the following equation,

$$\begin{aligned} \frac{d\vec{\mathbf{I}}(s, \mu, \varphi)}{ds} &= \vec{\mathbf{K}}(\mu, \varphi) \vec{\mathbf{I}}(s, \mu, \varphi) \\ &\quad - \int_0^{2\pi} \int_{-1}^1 \vec{\mathbf{I}}(s, \mu', \varphi') \vec{\mathbf{M}}(\mu, \mu', \varphi, \varphi') d\mu' d\varphi' \\ &\quad - \vec{\sigma}(\mu, \varphi) B(T(s)) \end{aligned} \quad (2.19)$$

where the propagation direction of the incoming incident wave is expressed by the cosine of the zenith angle μ' and the azimuth angle φ' , s denotes the position in the atmosphere relating to the x, y and z axis, $\vec{\mathbf{I}}(s, \mu, \varphi)$ is the Stokes vector in the direction of (μ, φ) at the position ds , $\vec{\mathbf{K}}$ indicates the extinction matrix along the propagation direction (μ, φ) , $\vec{\mathbf{M}}$ is the scattering matrix, $\vec{\sigma}$ is the emission vector, and B is the Planck radiation at the temperature T .

In a plane-parallel and azimuthally-symmetric atmosphere, the radiation from the ground surface is also azimuthally-symmetric. The particles in the atmosphere are assumed to have no preferred orientation in the azimuth direction. Therefore, the extinction matrix $\vec{\mathbf{K}}$ and the emission vector $\vec{\sigma}$ are only a function of the zenith angle, and the scattering matrix $\vec{\mathbf{M}}$ is also reduced to be only a function of the incident and scattered zenith angles. The Stokes parameters U and V are zero and the wave is supposed to be only linearly polarized, due to the azimuthally symmetric radiation in the atmosphere. Therefore, the radiative transfer equation can be simplified as follows (*Evans and Stephens, 1995b*),

$$\begin{aligned} \mu \frac{d\vec{\mathbf{I}}(z, \mu)}{dz} &= \vec{\mathbf{K}}(z, \mu) \vec{\mathbf{I}}(z, \mu) \\ &\quad - 2\pi \int_{-1}^1 \vec{\mathbf{I}}(z, \mu') \vec{\mathbf{M}}(z, \mu, \mu') d\mu' \\ &\quad - \vec{\sigma}(z, \mu) B(T(z)) \end{aligned} \quad (2.20)$$

where

$$ds = \frac{dz}{\cos \vartheta} = \frac{dz}{\mu}$$

ds is independent on x and y axes, μ is the cosine of the zenith angle of the incident wave, while μ' is the cosine of the zenith angle of the scattered wave, the extinction matrix \vec{K} and the emission vector $\vec{\sigma}$ are only a function of the incident zenith direction μ , the scattering matrix \vec{M} only closely depends on the incident and scattered zenith directions due to the plane-parallel and azimuthally-symmetric atmosphere.

2.2.2 Solution to the polarized radiative transfer equation

To solve the polarized radiative transfer equation (Equation 2.20), several solutions have been developed (*Evans and Stephens, 1991; Schulz et al., 1999; Liou, 2002; Cornet et al., 2010*), e.g., the discrete-ordinates method, Monte-Carlo method, doubling and adding method, etc. In the following, the doubling and adding method will be briefly reviewed.

The doubling and adding method which calculates the transmitted and reflected intensity in the atmosphere is applicable to the polarized radiation transfer calculations with randomly or non-randomly oriented particles (*Evans and Stephens, 1991*). The scheme of the doubling and adding method is shown in Figure 2.6. Suppose one single layer in the atmosphere. The intensity of the layer interacts with the intensity originating from other layers. The upward and downward intensity in this layer can be expressed by the interaction between the intensity

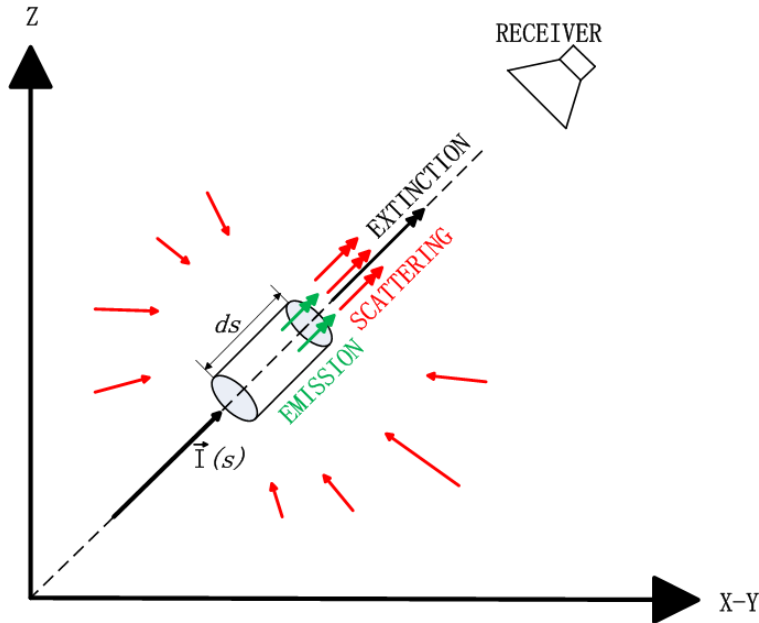


Figure 2.5: Scattering, extinction and emission by the medium along an infinitesimal path ds . The one-headed black arrow indicates the direction of the incident beam. Double-headed green arrows indicate the emission in the infinitesimal path ds along the incident direction specifying by (μ, φ) . One-headed red arrows are the intensities from adjacent columns in 4π steradian, while double-headed red arrows are the scattered wave by the medium along the path into the direction (μ, φ) .

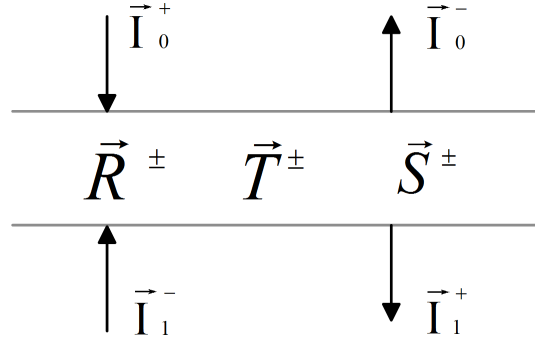


Figure 2.6: Configuration of the reflected and transmitted intensities for the doubling and adding method. The sign “-” (“+”) specifies that the intensity propagates upwards (downwards). \vec{R} , \vec{T} and \vec{S} are the reflection matrix, transmission matrix and emission vector, respectively. The Stokes vector $\vec{\mathbf{I}}_1^-$ and $\vec{\mathbf{I}}_0^+$ are the incident intensities, and the Stokes vector $\vec{\mathbf{I}}_0^-$ and $\vec{\mathbf{I}}_1^+$ are the emerging intensities. (From *Evans and Stephens*, 1991)

originating from different layers (*Evans and Stephens*, 1991).

$$\begin{aligned}\vec{\mathbf{I}}_1^+ &= \vec{T}^+ \vec{\mathbf{I}}_0^+ + \vec{R}^+ \vec{\mathbf{I}}_1^- + \vec{S}^+ \\ \vec{\mathbf{I}}_0^- &= \vec{T}^- \vec{\mathbf{I}}_1^- + \vec{R}^- \vec{\mathbf{I}}_0^+ + \vec{S}^-\end{aligned}\quad (2.21)$$

Equation 2.21 can be also written as

$$\begin{bmatrix} \vec{\mathbf{I}}_1^+ \\ \vec{\mathbf{I}}_0^- \end{bmatrix} = \begin{bmatrix} \vec{T}^+ & \vec{R}^+ \\ \vec{R}^- & \vec{T}^- \end{bmatrix} \begin{bmatrix} \vec{\mathbf{I}}_0^+ \\ \vec{\mathbf{I}}_1^- \end{bmatrix} + \begin{bmatrix} \vec{S}^+ \\ \vec{S}^- \end{bmatrix}\quad (2.22)$$

where the $\vec{\mathbf{I}}_1^-$ and $\vec{\mathbf{I}}_0^+$ are the Stokes vectors of the incident intensity, and the $\vec{\mathbf{I}}_0^-$ and $\vec{\mathbf{I}}_1^+$ are the emerging intensities from the layer. The sign “-” and “+” denotes that the intensity propagates upwards and downwards, respectively. The emerging upward intensity is the superposition of the incident downward radiation reflected by the medium, the transmitted upward radiation and the emission of this layer.

The atmosphere in the doubling and adding method is divided into a number of infinitesimal thin layers which are considered to be vertically homogenous. For every individual layer, the transmission matrix \vec{T} , the reflection matrix \vec{R} and the source vector \vec{S} specify the physical properties of these layers, which are characterized by the extinction, scattering matrix and emission vector described in Section 2.1.3 (*Evans and Stephens*, 1995b). The reflection matrix \vec{R} relating to the scattering matrix expresses the intensity scattered by the medium into the specular direction of the incident wave. The transmission matrix \vec{T} is used to specify the amount of the intensity propagating in the same direction as the incident intensity after scattering and extinction processes of the incident wave in the layer. The source vector \vec{S} is a function of the radiance emitted by this layer.

The surface boundary is treated as one single layer with uniform transmission. The reflection of the surface boundary depends on the surface radiative properties and the surface type. Two idealized surface types are Lambertian and Fresnel surfaces. For a Lambertian surface, the radiance emitted by the surface is isotropic, and the reflected intensity by the surface is also isotropic and unpolarized. The emitted intensity is temperature-dependent and directly

proportional to the emissivity of the Lambertian surface. If it is a Fresnel surface (e.g. water surface), it obeys the specular reflection law. The reflection at the specular angle of the incident wave, as well as the emitted intensity, depends not only on radiative properties but also on the polarization state of the incident wave.

2.3 Scattering properties of particles

The scattering properties by one single particle can be calculated by the amplitude scattering matrix which links the incident wave with the scattered wave (Equation 2.15). Consider a collection of independent particles distributed randomly in the atmosphere. The particles in the collection are of different sizes, geometries and orientations. The diffusion effects among the particles can be ignored when the distance between each particles is much larger than the particle size, by more than a factor of 4. Thus, only the first-order scattering in the collection is considered. The total scattered electric field by the collection of particles is therefore the superposition of the scattered electric field by the individual particles inside the collection. Furthermore, the extinction matrix, scattering matrix, and emission vector can be simplified when the atmosphere is plane-parallel and azimuthally symmetric, as described in section 2.2. The non-zero elements in the Stokes vector are only I and Q . Suppose that the particle number in the collection is N . Based on Equations 2.16 – 2.18, the total extinction matrix, scattering matrix and emission vector of this particle collection can be given in the following forms

$$\begin{aligned}
\vec{K} &= \sum N_i \begin{bmatrix} K_{11} & K_{12} \\ K_{21} & K_{22} \end{bmatrix} \\
&= \sum N_i \frac{2\pi}{k} \begin{bmatrix} \text{Im}(F_{vv} + F_{hh}) & \text{Im}(F_{vv} - F_{hh}) \\ \text{Im}(F_{vv} - F_{hh}) & \text{Im}(F_{vv} + F_{hh}) \end{bmatrix} \\
\vec{M} &= \sum N_i \begin{bmatrix} M_{11} & M_{12} \\ M_{21} & M_{22} \end{bmatrix} \\
&= \sum \frac{1}{2} N_i \begin{bmatrix} (F_{vv}F_{vv}^* + F_{vh}F_{vh}^* + F_{hv}F_{hv}^* + F_{hh}F_{hh}^*) & (F_{vv}F_{vv}^* - F_{vh}F_{vh}^* + F_{hv}F_{hv}^* - F_{hh}F_{hh}^*) \\ (F_{vv}F_{vv}^* + F_{vh}F_{vh}^* - F_{hv}F_{hv}^* - F_{hh}F_{hh}^*) & (F_{vv}F_{vv}^* - F_{vh}F_{vh}^* - F_{hv}F_{hv}^* + F_{hh}F_{hh}^*) \end{bmatrix} \\
\vec{\sigma} &= \sum N_i \begin{bmatrix} \sigma_1 \\ \sigma_2 \end{bmatrix} \\
&= \sum N_i \begin{bmatrix} K_{11}(\hat{n}) - \int M_{11}(\hat{n}, \hat{n}') d\Omega' \\ K_{12}(\hat{n}) - \int M_{12}(\hat{n}, \hat{n}') d\Omega' \end{bmatrix} \tag{2.23}
\end{aligned}$$

where N_i is a sub-collection of particles with the same geometry, size and orientation and it is satisfied with $\sum N_i = N$. The parameters F_{vv} , F_{vh} , F_{hv} and F_{hh} are corresponding elements of the amplitude scattering matrix given in Equation 2.15.

To calculate the amplitude scattering matrix of particles preparing for the polarized radiative transfer model, one must derive the electromagnetic scattering field based on the electromagnetic theory. One of the accurate solutions is the Mie theory (*Mie*, 1908; *Debye*, 1909). A full description of the Mie theory can be found, e.g., in *van de Hulst* (1957) and *Bohren and Huffman* (1998). The Mie theory is an analytic solution to the scattering by spheres and it is widely used for its efficiency and accuracy.

In the Mie theory, the separation of variable method is used in order to expand the incident and scattered electric fields in spherical vector wave functions. The boundary conditions

of the spherical particles are then employed to solve the expansion coefficients of scattered electric fields. The expansion coefficients in the Mie theory a_n and b_n are a function of the particle size parameter x . x is expressed by the radius of the sphere r and the wavelength in the medium λ ,

$$x = \frac{2\pi r}{\lambda} \quad (2.24)$$

In the forward direction, the elements in the amplitude scattering matrix are given as

$$F_{vv} = F_{hh} = F = \frac{i}{2k} \sum_n (2n+1)(a_n + b_n) \quad (2.25)$$

where k is the wave number and i is the imaginary unit.

However, particles in the atmosphere are usually not perfectly-shaped spherical particles and their geometry is far more complicated than spheres in reality. Numerical solutions to the electromagnetic scattering by irregularly-shaped particles have been developed in decades in many research fields (e.g., *Mishchenko et al.*, 1996; *Yang and Liou*, 1996; *Draine and Flatau*, 1994; *Yurkin and Hoekstra*, 2011). An overview of these numerical methods can be found in *Kahnert* (2003). In the following, two algorithms for nonspherical particles which are used in this study, i.e., the T-matrix method and the DDA algorithm, will be introduced.

2.3.1 T-matrix method

The T-matrix method was first proposed by *Waterman* (1965). It is popularly used in the calculations of the electromagnetic scattering by particles. The method has been applied to calculate the scattering by rotationally symmetric particles, like spheroids, plates, cylinders and Chebyshev particles (*Mishchenko et al.*, 1996; *Mishchenko*, 2000; *Mishchenko et al.*, 2002). The particles in the T-matrix method can be assumed to be with random or fixed orientation.

In the T-matrix method, the incident and scattered fields are expanded in the series of spherical vector wave functions. The expansion coefficients of the scattered fields (\mathbf{p} and \mathbf{q}) relate to the expansion coefficients of the incident fields (\mathbf{a} and \mathbf{b}), by means of the so-called transition matrix (T-matrix) (*Mishchenko et al.*, 1996).

$$\begin{bmatrix} \mathbf{p} \\ \mathbf{q} \end{bmatrix} = \mathbf{T} \begin{bmatrix} \mathbf{a} \\ \mathbf{b} \end{bmatrix} = \begin{bmatrix} \mathbf{T}^{11} & \mathbf{T}^{12} \\ \mathbf{T}^{21} & \mathbf{T}^{22} \end{bmatrix} \begin{bmatrix} \mathbf{a} \\ \mathbf{b} \end{bmatrix} \quad (2.26)$$

The transition matrix \mathbf{T} depends only on the particle characteristics, i.e., particle shape, composition, size parameter, orientation, etc. The amplitude scattering matrix can be derived by the T-matrix accordingly when the expansion coefficients of the scattered electric field is solved (*Mishchenko et al.*, 2002). It is diagonal when the particle is averaged-oriented or rotationally-symmetric. For spherical particles, the T-matrix method reduces to the Mie theory.

The T-matrix code developed by *Mishchenko* (2000) can be employed to calculate the scattering properties of perfectly or partially oriented particles. It can calculate the size parameter of the particle up to 30 or more (*Kahnert*, 2003). The size parameter of a particle is expressed by $2\pi r_e/\lambda$, where r_e is the equivalent-volume radius of the particle and λ is the wavelength.

For extreme size particles, i.e., the ratio of the maximum dimension to the minimum dimension of the particles is quite large, like thin plates or long columns, it is difficult to reach convergence in the T-matrix method.

The directions of the incident and scattered waves in the T-matrix code package (*Mishchenko, 2000*) is defined by the zenith and azimuth angles (ϑ^{sca} , φ^{sca} , ϑ^{inc} , φ^{inc}). The three Euler angles of rotation (β , θ , ϕ) are used to describe the orientation of the particles in the T-matrix method. The specifications of the three Euler angles are shown in Figure 2.7. Panel (1) of Figure 2.7 shows the so-called laboratory reference frame X-Y-Z. When the laboratory reference frame rotates around the Z axis (clockwise direction if looking in the direction of the Z axis), the angle between the axis Y1 (the new Y axis) and the original axis Y in the laboratory frame is the Euler angle β , as shown in Panel (2) of Figure 2.7. When the reference frame rotates around the axis Y1 in Panel (3), the Euler angle θ is the angle between the axis Z2 (the new Z axis) and the axis Z. The rotation around the axis Z2 gives the Euler angle ϕ in Panel (3). The new reference frame which is defined with the axes X3-Y3-Z3 is the so-called particle frame, as shown in the Panel (4) of Figure 2.7.

It is convenient to use a global reference frame, i.e., the same reference frame for the scattering and radiative transfer calculations. The laboratory reference frame in the T-matrix method is treated as the global coordinate system for radiative transfer calculations, because of the arbitrary incident and scattered directions of the electric wave that is defined in the laboratory reference frame.

2.3.2 DDA algorithm

The DDA algorithm (*Purcell and Pennypacker, 1973*) can be used to calculate the scattering by spherical or non-spherical particles (*Draine and Flatau, 1994; Evans and Stephens, 1995a; Yurkin and Hoekstra, 2007, 2011*). In this algorithm, a particle is divided into an array of dipoles. Each dipole represents a volume cell of the particles, and is located in the center of the volume cell. The distance between two dipoles is much less than wavelength. Therefore, each dipole is subject to the sum field of the incident field and the fields contributed by other dipoles of the particle. It can be used to calculate scattering properties of particle with arbitrary geometry, size and orientation. In contrast to the T-matrix method, for particles with extreme sizes, the DDA method is still applicable.

The calculation accuracy of the DDA method is highly dependent upon the number of the discretized dipoles in the particle (e.g., *Kim, 2004*). However, the large number of dipoles imposes a significant burden on CPUs and makes the calculations computationally expensive. In the DDA code package provided by *Draine and Flatau, 2004* (2004) (hereinafter called DDSCAT6.1), the criteria $|m_0|kd < 0.5$ should be satisfied for accurate scattering matrix calculations, where m_0 is the refractive index of the particle, k is the wave number in vacuum and d is the distance between each dipole.

The laboratory and particle reference frames defined in the DDSCAT6.1 code package are different from the coordinate system shown in Figure 2.7. The X-Y-Z axes in the DDSCAT6.1 code package correspond to the Z-X-Y axes in the T-matrix method, respectively, if a coincident definition in the two approaches is arrived for the definition of the three Euler angles (β , θ , ϕ). Moreover, the propagation direction of the incident wave is fixed in the X axis in the DDSCAT6.1 code package, instead of flexible incident directions in the T-matrix method. The output amplitude scattering matrix in the DDSCAT6.1 code package is given as a func-

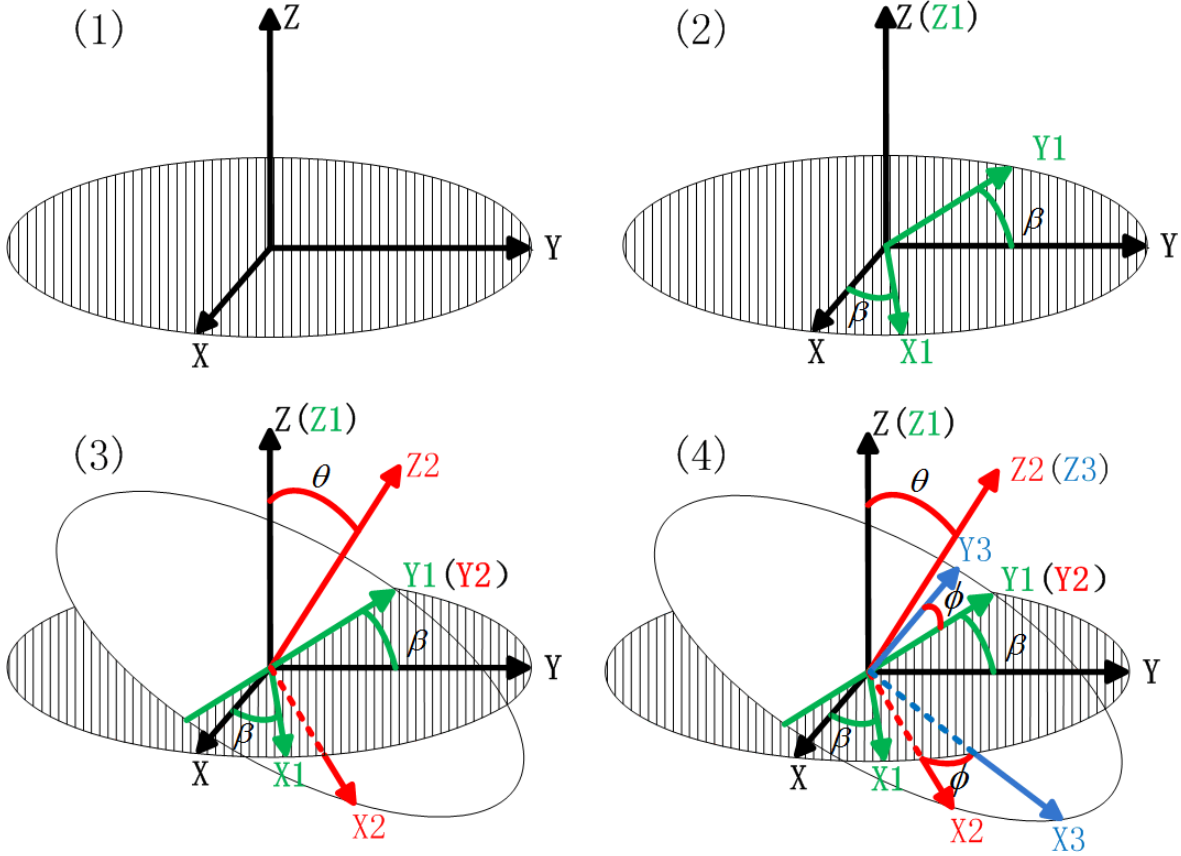


Figure 2.7: The three Euler angles of rotation (β , θ , ϕ) specify the orientation of the particles. Panel (1) is the so-called laboratory coordinate system. When looking into the direction of Z-axis in Panel (2), the clockwise rotation angle of the X-Y plane around the Z-axis is the Euler angle β , which is in the range of 0 and 2π . Panel (3) illustrates the Euler angle $\theta \in [0, \pi]$ caused by the rotation of the new axis Y1. In Panel (4) the axes X3-Y3-Z3 indicate the particle coordinate system, and the Euler angle $\phi \in [0, 2\pi]$, which results from the clockwise orientation of the axis Z2, is the angle between the Y2 and Y3 axes in the X2-Y2 plane when looking in the direction of the Z2-axis.

tion of the scattering angles, which are denoted by the zenith and azimuth angles (ϑ , φ) in the laboratory reference frame.

However, for the input of the polarized radiative transfer equation in the plane-parallel atmosphere (Equation 2.20), the direction of the incident radiance ranges from 0 to π . Generally, the scattering properties of oriented particles varies with the direction of the incident wave (Yang *et al.*, 2011). In order to calculate the scattering properties of particles with arbitrary size and orientation by means of the DDSCAT6.1 code package, one choice is to orientate the particle when the direction of the incident beam is fixed.

For convenience, the particle reference frame is treated as the global coordinate for the radiative transfer calculations, instead of the laboratory frame as the global coordinate system in the T-matrix method. Therefore, the output amplitude scattering matrix in the laboratory reference frame should be transformed into the corresponding value in the particle frame.

The orientation of the particles is defined by the three Euler angles (β , θ , ϕ) as shown in Figure

2.7, when the X-Y-Z axes are exchanged according to their definition in the DDSCAT6.1 code. The matrix \bar{t} which links the electric field in the particle frame with the laboratory frame can be expressed by

$$\begin{bmatrix} E_{0v}^P \\ E_{0h}^P \end{bmatrix} = \bar{t}(\hat{n}, \beta, \theta, \phi) \begin{bmatrix} E_{0v}^L \\ E_{0h}^L \end{bmatrix} \quad (2.27)$$

where E_{0v} and E_{0h} are the complex vertical and horizontal electric fields, the superscript P or L denotes the particle or laboratory reference frame.

The amplitude scattering matrix in the laboratory reference frame can be transformed to the corresponding matrix in the particle reference frame. And the relation between the two reference frames can be derived accordingly (*Mishchenko et al.*, 2002),

$$\begin{aligned} \bar{S}^P(\vartheta_P^{sca}, \varphi_P^{sca}; \vartheta_P^{inc}, \varphi_P^{inc}; \beta, \theta, \phi) = \\ \bar{t}(\hat{n}^{sca}; \beta, \theta, \phi) \bar{S}^L(\vartheta_L^{sca}, \varphi_L^{sca}; \vartheta_L^{inc}, \varphi_L^{inc}; \beta, \theta, \phi) \bar{t}^{-1}(\hat{n}^{inc}; \beta, \theta, \phi) \end{aligned} \quad (2.28)$$

where \bar{S}^P is the 2×2 amplitude scattering matrix in the particle reference frame, and \bar{S}^L is in the laboratory reference frame, (β, θ, ϕ) are the three Euler angles illustrated in Figure 2.7. The specified definitions of the three Euler angles can be also found in *Draine and Flatau*, (2004) and *Mishchenko et al.*, (2002). The unit vector \hat{n} denotes the propagating direction of the wave, and the superscript of the vector \hat{n}^{sca} (\hat{n}^{inc}) denotes the propagation direction of the scattered (incident) wave.

The matrix $\bar{\alpha}$ converts the vertical and horizontal components of the electric field into the three components in Cartesian coordinate system, where the E_{0x} (E_{0y} or E_{0z}) is the electric component in the X (Y or Z) axis direction.

$$\begin{bmatrix} E_{0x} \\ E_{0y} \\ E_{0z} \end{bmatrix} = \bar{\alpha}(\vartheta, \varphi) \begin{bmatrix} E_{0v} \\ E_{0h} \end{bmatrix} \quad (2.29)$$

The matrix $\bar{\beta}$ connects the three components in the particle reference frame to the components in the laboratory reference frame.

$$\begin{bmatrix} E_{0x}^P \\ E_{0y}^P \\ E_{0z}^P \end{bmatrix} = \bar{\beta}(\beta, \theta, \phi) \begin{bmatrix} E_{0x}^L \\ E_{0y}^L \\ E_{0z}^L \end{bmatrix} \quad (2.30)$$

Then the matrix \bar{t} in Equation 2.28 can be expressed by the matrices $\bar{\alpha}$ and $\bar{\beta}$

$$\bar{t}(\hat{n}; \beta, \theta, \phi) = \bar{\alpha}^{-1}(\vartheta_P, \varphi_P) \bar{\beta}(\beta, \theta, \phi) \bar{\alpha}(\vartheta_L, \varphi_L) \quad (2.31)$$

The matrices of $\bar{\alpha}$ and $\bar{\beta}$ are given as follows (*Mishchenko et al.*, 2002; *Mishchenko*, 2000),

$$\bar{\alpha}^{-1}(\vartheta, \varphi) = \begin{bmatrix} -\sin(\vartheta) & \cos(\vartheta) \cos(\varphi) & \cos(\vartheta) \sin(\varphi) \\ 0 & -\sin(\varphi) & \cos(\varphi) \end{bmatrix} \quad (2.32)$$

$$\bar{\alpha}(\vartheta, \varphi) = \begin{bmatrix} -\sin(\vartheta) & 0 \\ \cos(\vartheta) \cos(\varphi) & -\sin(\varphi) \\ \cos(\vartheta) \sin(\varphi) & \cos(\varphi) \end{bmatrix} \quad (2.33)$$

$$\overline{\beta}(\beta, \theta, \phi) = \begin{bmatrix} \cos(\theta) & \sin(\theta) \cos(\phi) & \sin(\theta) \sin(\phi) \\ -\sin(\theta) \cos(\beta) & \cos(\theta) \cos(\beta) \cos(\phi) - \sin(\beta) \sin \phi & \cos(\theta) \cos(\beta) \sin \phi + \sin(\beta) \cos(\phi) \\ \sin(\theta) \sin(\beta) & -\cos(\theta) \sin(\beta) \cos(\phi) - \cos(\beta) \sin(\phi) & -\cos(\theta) \sin(\beta) \sin(\phi) + \cos(\beta) \cos(\phi) \end{bmatrix} \quad (2.34)$$

Compared to the coordinate transformation described in *Mishchenko (2000)*, the exchange of the columns here is due to the different reference frames defined in the T-matrix method and DDSCAT6.1 code.

For particles with averaged azimuth orientations, the scattering matrix

$$M_1(\vartheta^{inc}, \vartheta^{sca}, \varphi^{inc} - \varphi_1^{sca}) = M_2(\vartheta^{inc}, \vartheta^{sca}, \varphi^{inc} - \varphi_2^{sca}) \quad (2.35)$$

if

$$|\varphi^{inc} - \varphi_1^{sca}| = |\varphi^{inc} - \varphi_2^{sca}|$$

where φ_1^{sca} and φ_2^{sca} are the azimuth angles of the scattered waves. The azimuth angles of the incident and scattered wave range from 0 to 2π .

Equation 2.35 indicates that, for particles with azimuthally averaged orientation, the scattering matrix is only dependent on the difference of the azimuth angles when the incident and scattered zenith directions are fixed. Moreover, in the azimuthally symmetric atmosphere (Equation 2.20), the incoming radiance is uniform in the azimuth direction. Suppose an incident wave in a specific direction of $(\vartheta^{inc}, \varphi^{inc})$, and the azimuth angle φ^{inc} distributed uniformly in the range from 0 to 2π . Instead of averaging over the incident wave with a uniform distribution in the azimuth direction, the scattering matrix is averaged over the scattered azimuth angle since the incident direction of the wave is fixed in the DDSCAT6.1 code. This is an equivalent calculation for particle scattering properties in the DDSCAT6.1 code package. The scattering matrix of the particles is therefore only a function of the zenith angles of the incident and scattered waves $(\vartheta^{inc}, \vartheta^{sca})$ for azimuthally symmetric atmosphere, when particle orientations are azimuthally averaged. Hence, the scattering matrix is independent on the azimuth angles of the incident and scattered waves. The extinction matrix and the emission vector are only a function of the incident zenith angle ϑ^{inc} .

Chapter 3

Instrumentation and data set

Oriented snow particles induce polarized signals between vertical and horizontal polarized channels due to their dichroism effects. In order to investigate the potential PD resulting from snow particles, ground-based polarization observations were carried out at UFS (~ 2650 m MSL) on Mount Zugspitze (German Alps, located at $47^{\circ}25'N$, $10^{\circ}59'E$).

The instruments used for the observations are presented in this chapter. Polarization observations are performed by a dual polarized microwave radiometer DPR at the frequency of 150 GHz. A second microwave radiometer deployed at UFS is for liquid water and water vapor observations during snowfall. The active instrument in this study is a K-band radar operating at 24.1 GHz. An overview of the three instruments and their specifications are fully given in Table 3.1. The polarization bias, which could be caused by the uncertainties of the calibration process, is corrected based on the observed PD during clear sky cases in the whole year 2010.

3.1 Instrumentation

3.1.1 Microwave radiometer: DPR

The dual polarized microwave radiometer DPR manufactured by Radiometer Physics GmbH (RPG) has been deployed at UFS since 2007. DPR provides TB measurements at three independent channels, one at 90 GHz and the other two channels at 150 GHz.

The definition of TB can be described as follows. Suppose an object with a physical temperature T and an frequency-dependent emissivity ε_{λ} . Its emitted intensity I_{λ} at the wavelength λ is associated with the corresponding intensity B_{λ} calculated by Planck's law.

$$I_{\lambda}(T) = \varepsilon_{\lambda}B_{\lambda}(T) \quad (3.1)$$

For a blackbody, its physical temperature T is the so-called brightness temperature. However, the emissivity of an object ε_{λ} is normally less than 1 and depends upon wavelength. The emitted intensity I_{λ} which is less than B_{λ} is related to the emissivity of the object. The TB of the object is then calculated by

$$\begin{aligned} \text{TB} &= I_{\lambda}^{-1}(T) \\ &= \varepsilon_{\lambda}B_{\lambda}^{-1}(T) \end{aligned} \quad (3.2)$$

where B_{λ}^{-1} is the reverse function of Planck's law. Therefore, the corresponding TB of the object is cooler than its physical temperature T when its emissivity is less than one.

The specification of DPR is given in Table 3.1. The two 150 GHz channels of DPR work at two orthogonal polarizations, vertical and horizontal, respectively. A wire grid in the DPR system is used to separate the received intensity into horizontal and vertical components, so that both the vertical and horizontal polarized channels measure separately and simultaneously. The whole instrument rotates around a fixed axis parallel to the ground surface. Therefore, the received polarized TB at 150 GHz can be conserved at horizontal and vertical polarizations. The long-term accuracy of this instrument is about 2 K at 150 GHz and the accuracy is about 1 K at 90 GHz. The observation period of DPR is ~ 14 min with an integration time of ~ 2 sec. During one period, the DPR measures TBs at different elevation angles ranging from 0° to 90° . The nine elevation angles which are investigated in this study are 15.6° , 25.2° , 34.8° , 44.4° , 54.0° , 63.6° , 73.2° , 82.8° and 90.0° .

The DPR blower and surveillance systems were further improved during the ‘‘Towards an Optimal estimation based Snow Characterization Algorithm’’ (TOSCA) campaign 2008/2009 (Löhnert *et al.*, 2011). To make sure that the observations of DPR are not contaminated by precipitating hydrometeors frozen on the radome of the antenna horn, a web-camera with a spot light has been deployed to observe the radome in order to qualitatively control the measured data. Meanwhile, a heated blower system is used to prevent falling snow and water drops accumulating on the DPR radome. In case of wet radome, the heated blower system can heat the radome to evaporate water drops.

TBs at 150 GHz analyzed in this study are the averaged TB between vertical and horizontal polarizations, i.e., $TB = (TB_v + TB_h)/2$, while the PD is the brightness temperature difference between the vertical and horizontal polarizations ($PD = TB_v - TB_h$). A negative sign ‘‘-’’ of PD indicates that TBs at the vertical polarization are lower than TBs at the horizontal polarization from ground-based observations, when describing the increase or decrease of PDs in this study.

3.1.2 Microwave radiometer: HATPRO

A second microwave radiometer at UFS is the humidity and temperature profiler (HATPRO), which has been also manufactured by RPG. It was installed next to the DPR. HATPRO has fourteen channels, and it measures TBs at the wing of the water vapor absorption line (22 GHz – 31 GHz) and at the oxygen absorption band (50 GHz – 60 GHz). The specification of HATPRO parameters can be found in Table 3.1.

HATPRO was also equipped with a web-camera and a spot light to observe the status of its antenna radome during daytime and night. The heated blower system is used to avoid melting ice and water covering the radome. The two microwave radiometers DPR and HATPRO are calibrated using liquid nitrogen every few months (Turner *et al.*, 2009).

HATPRO provides integrated water vapor (IWV) and liquid water observations. Ground-based passive microwave radiometry is one of the most accurate methods to derive LWP. The LWP and IWV in this study are independently retrieved by a statistical algorithm (Löhnert and Crewell, 2003). The accuracy of the retrieved IWV is ~ 0.5 kg/m² for this algorithm and the accuracy of LWP is 20~30 g/m². Due to the different attenuation caused by IWV and LWP in the atmosphere, the responses of measured TBs to IWV and LWP are different when varying the frequencies at the wing of water vapor absorption from 22 GHz to

Table 3.1: An overview of the instruments

Instrument	Parameter	Specification
DPR		
	Frequency / GHz	90; 150 (v ^a); 150(h ^a)
	Bandwidth / MHz	2000; 2000; 2000
	Optical Resolution (HPBW ^b)	2°; 2°; 2°
	Integration time / s	2
	Size / mm×mm×mm	630×360×900
	Accuracy / K	~2 K for 150 GHz channels, ~1 K for 90 GHz channel
	Weight / kg	~120
HATPRO		
	Receiver 1	water vapor absorption line
	Frequency / GHz	22.24; 23.04; 23.84; 25.44; 26.24; 27.84; 31.40
	Bandwidth / MHz	230; 230; 230; 230; 230; 230; 230
	Optical Resolution (HPBW ^b)	3.3°-3.7°
	Receiver 2	oxygen absorption band
	Frequency / GHz	51.26; 52.28; 53.86; 54.94; 56.66; 57.30; 58.00
	Bandwidth / MHz	230; 230; 230; 230; 600; 1000; 2000
	Optical Resolution (HPBW ^b)	2.2°-2.5°
	Integration time / s	1
	Accuracy / K	~1
	size / mm×mm×mm	630×360×900
	Weight / kg	~60
MRR		
	Frequency / GHz	24.1
	Radar type	FM-CW ^c
	Temporal resolution / min	1
	Range resolution / m	100
	Antenna diameter / m	0.5
	HPBW ^b	1.5°
	Sensitivity	~0 dB
	Detection range / m	3000
No. of range gates	30	

^a polarization status of the channel, v for vertical polarization and h for horizontal polarization

^b the half power beam width (it is also called 3-dB beam width)

^c frequency modulated continuous wave

31 GHz (Figure 2.4). The amount of liquid water and water vapor in the atmosphere then can be retrieved accordingly by relating measured TBs to their absorption in the statistical algorithm.

3.1.3 Micro rain radar

The micro rain radar MRR manufactured by Meteorologische Messtechnik GmbH (METEK) operates at 24.1 GHz at UFS. It is a zenith pointing radar with a single polarized receiver (Table 3.1). The MRR operates with a spatial resolution of 100 m and a temporal resolution of 1 min. The detection range of MRR is up to 3000 m. MRR provides snowfall information in snow events. It can be used for the detection of moderate and heavy snowfall events; however, it is not sensitive to light snowfall and small droplets due to its low sensitivity of around 0 dB (*Kneifel et al.*, 2011).

The effective reflectivity factor Ze and the mean snowfall Doppler velocity are derived from the raw data, by means of the algorithm proposed by *Kneifel et al.* (2011). The effective reflectivity factor Ze of MRR is defined as the summation of the backscattering cross sections in a volume (*Kneifel et al.*, 2011, Equation 2). Considering the near field effects at lower level, the effective reflectivity Ze at an altitude lower than 300 m is excluded. The integrated Ze between an altitude of 300 m (above ground level, AGL) and 2500 m (AGL), which is closely related to snow water path (SWP) during snow events, is expressed in Equation 3.3.

$$Ze, int = 10 \log_{10} \int_{300 \text{ m}}^{2500 \text{ m}} Ze(h') dh \quad (3.3)$$

where h (in m) is the vertical resolution of MRR, $Ze(h')$ (in mm^6m^{-3}) is the effective reflectivity factor at height h' (in m).

3.1.4 Additional instruments

The UFS is further equipped with a Jenoptik CHM15K ceilometer, before 1 June 2010 a Vaisala ceilometer was deployed at UFS. The zenith-pointing ceilometer operates at a wavelength of 1064 nm. Its observations are only available at zenith looking. The observation of ceilometer is based on the light detecting and ranging (LIDAR) principle. Cloud base heights can be derived from the analysis of the received laser beams by the ceilometer, i.e., the beam travel time and the backscattering information of the laser pulses. The detection range of the ceilometer is up to 15 km. It is used to detect “clear sky” conditions in this study.

Another auxiliary instrument is the Parsivel optical disdrometer (*Löffler-Mang and Joss*, 2000), which is used to exclude blowing snow events. The Parsivel optical disdrometer can detect particles with diameters ranging from 0.3 mm to 30 mm.

At the summit of Mount Zugspitze (2962 m MSL, ~ 300 meter above UFS), the standard weather observations (including 2m-temperature, wind speed and direction, etc) is hourly collected by the weather station operated by German Weather Service (DWD). The synoptic observations are recorded by a human observer at the weather station.

3.2 DPR PD bias correction

When the radiation from the surface ground is unpolarized and no dichroism medium exist in the atmosphere, PDs between the 150 GHz horizontal and vertical polarization channels are expected to be zero during clear sky at any elevation angle due to the dominant gaseous absorption/emission processes in the atmosphere. PDs at an elevation angle of 90° should

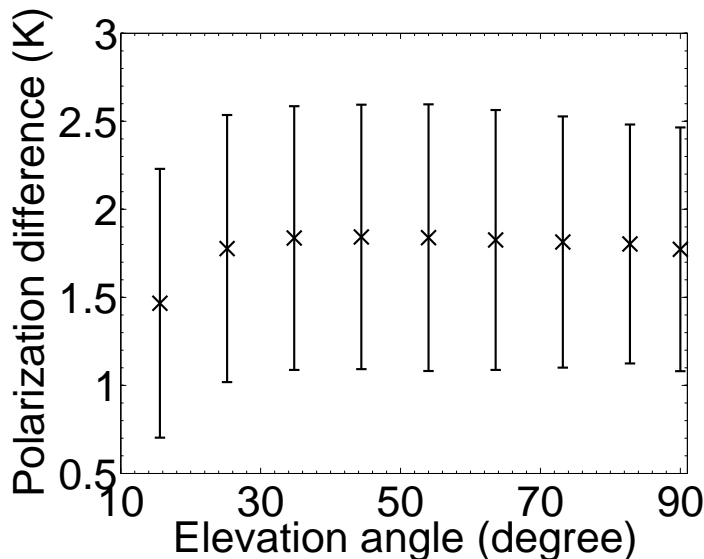


Figure 3.1: Mean value and standard deviation of polarization difference between vertical and horizontal polarizations at 150 GHz as a function of elevation angle during clear-sky periods in 2010. (From *Xie et al.*, 2012)

also be zero during snowfall if the snow particles are assumed to be azimuthally symmetric (*Evans and Stephens, 1995b*).

However, the two orthogonal channels of DPR show a small bias even during clear sky conditions due to calibration uncertainty. In order to investigate the temporal variability of this bias, the clear sky cases are analyzed during the entire year 2010. These clear sky cases are determined by the combination of available instruments with strongest emphasis on the ceilometer. The ceilometer operates in zenith mode, and no information about the spatial distribution of clouds is available. Therefore, the zenith observation of these instruments sometimes gives a clear sky flag even if clouds are present in the off-zenith viewing direction. In order to avoid such mis-identifications of clear sky cases, the restriction that the clear sky conditions had to last at least one hour was made. The web-cameras of DPR and HATPRO view a part of the sky and the horizon, besides the radiometer radome. Thus, this information was additionally used to verify clear-sky conditions during daytime. In order to quantify the clear-sky calibration offset, Figure 3.1 shows the mean value and standard deviation of PDs as a function of DPR elevation angle using the whole year clear sky data. The total amount of clear sky periods identified in 2010 sums up to 398.5 hours. The mean PDs during clear sky are 1.8 K at different elevation angles with a standard deviation of 0.7 K. An exception is the lowest elevation angle of 15.8 where the mean PD is 1.5 K.

In order to be able to correct for this clear-sky PD bias, Figure 3.2 shows the temporal variability of the 4-hourly averaged mean value and standard deviation of PDs at the elevation angle of 34.8° for all clear sky cases. The mean value and standard deviation are related to time periods between one and four hours, i.e., 40 – 160 measurements per elevation angle. The mean clear-sky values of PDs at the elevation angle of 34.8° are mostly very close to 2 K (standard deviation varies from 0.3 K to 0.9 K). It indicates that the DPR has a systematic, but rather stable offset. Only at the beginning of October, mean PD during clear sky is around -1 K, and the observed TBs are around 60 K. Based on these considerations, the yearly mean values of the PD offsets at different elevation angles were used to correct each

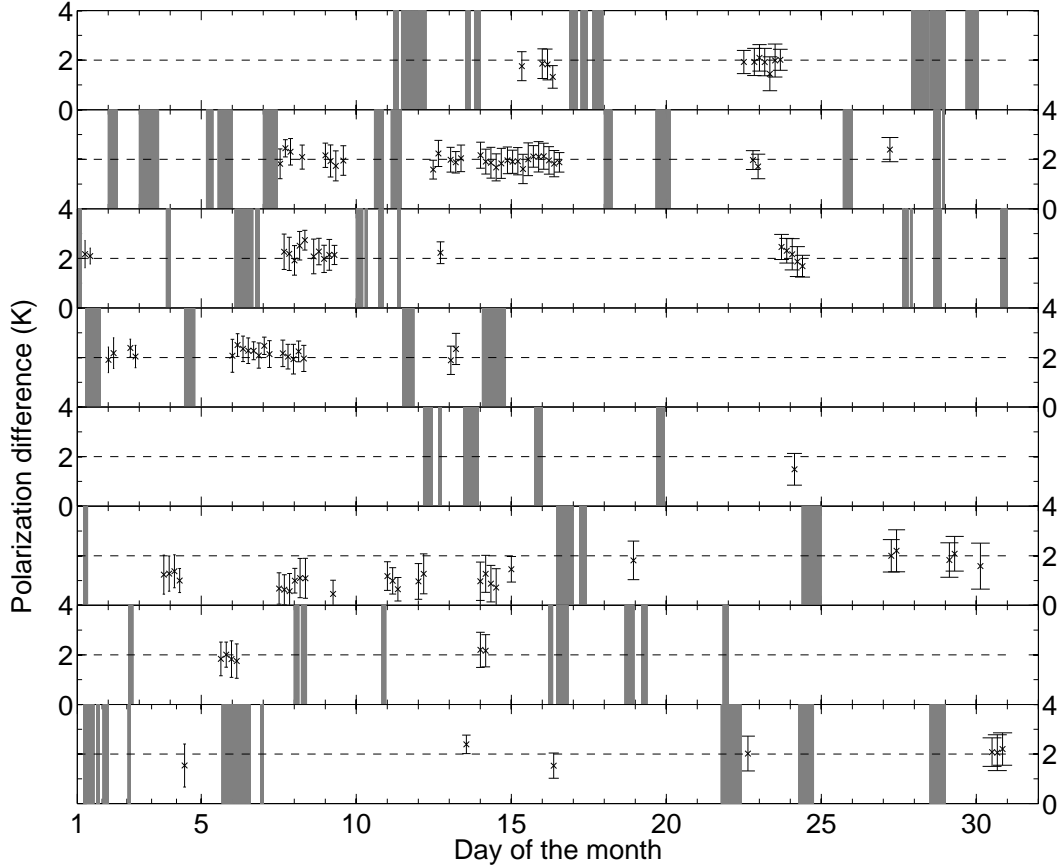


Figure 3.2: Time series of 4-hourly mean values (crosses) and standard deviations (error bars) of polarization difference during clear sky at 34.8° elevation angle at 150 GHz in 2010, from top to bottom, January, February, March, April, May, October, November, and December. Gray intervals indicate snow events identified by the Micro Rain Radar (MRR) and Web cameras. The number of snow events is 75 during the whole year 2010 (458 hours of snowfall). (From *Xie et al.*, 2012)

measurement during snowfall events (gray intervals of Figure 3.2). MRR observations are used to identify snow cases, and the web-cameras of DPR and HATPRO provide auxiliary observations to determine snowfall duration during daytime. The total snowfall time found for the year 2010 is 458 hours. Note that no snowfall cases were found in June, July, August and September since the observed environmental temperature was higher than 0°C at UFS. Figure 3.3 shows the number of PD occurrence for the whole time period as a function of TB during clear sky at 34.8° elevation angle. Observations at this elevation angle will be investigated later in RT simulations in Chapter 5. PD values in Figure 3.3 have been corrected with the average bias during 2010, as shown in Figure 3.1. As we can see in Figure 3.3, PDs at 34.8° elevation angle mostly range between -1 K to $+1\text{ K}$ after bias correction. Only for a few cases which occurred along with high TBs at the beginning of October, the bias-corrected PD values can be found up to -3 K (Figure 3.3). The distribution of bias-corrected PD at 34.8° elevation during clear sky cases verifies the stability of the DPR system during the measurements (Figure 3.4).

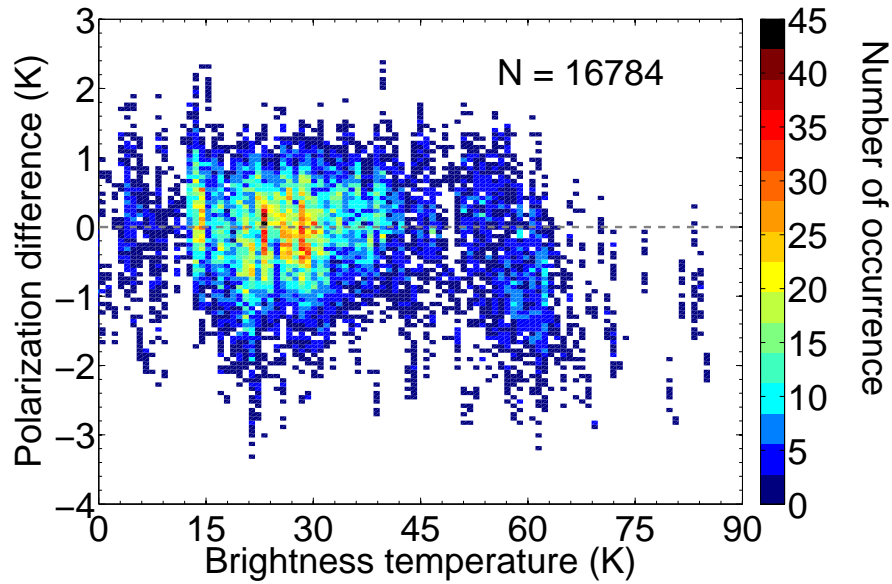


Figure 3.3: Number of occurrences of polarization difference and brightness temperature at 34.8° elevation angle at 150 GHz during clear-sky periods in 2010. Note that all values are bias corrected. (From *Xie et al.*, 2012)

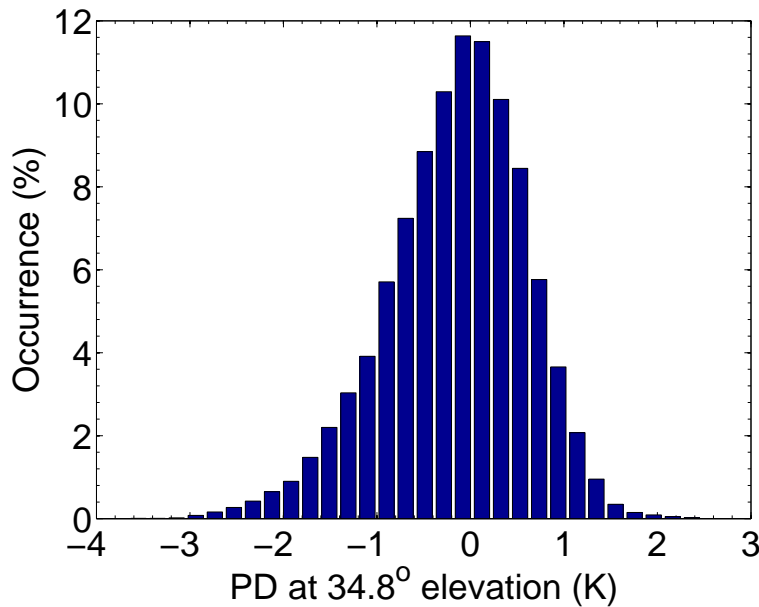


Figure 3.4: Occurrence of bias-corrected polarization difference at 34.8° elevation angle at 150 GHz during clear-sky periods in 2010.

In the following chapter, the observations performed by the combination of the instruments at UFS are presented to investigate potential PDs caused by oriented snow particles (Chapter 4). Based on the analysis of the 458 hours snowfall in the entire year 2010 (Chapter 4), RT simulations using a polarized radiative transfer model (Chapter 2) are used to examine the dependencies of PD and TB on snow parameters (Chapter 5). The implications of polarization observations for snow retrievals are also investigated in Chapter 5.

Chapter 4

Ground-based polarization observation during snowfall

To observe the potential PDs caused by preferentially-oriented snow particles during snowfall, polarization observations were performed at the frequency of 150 GHz at UFS, using the dual polarized microwave radiometer DPR. The two auxiliary instruments, MRR and microwave radiometer HATPRO, have been also deployed at UFS (described in Chapter 3) for snowfall observations since the TOSCA campaign 2008/2009 (*Löhnert et al.*, 2011).

In this chapter, the synergetic observations carried out by the instruments at UFS are analyzed, in order to gain an insight into snow particle orientation and to explore the potential role of polarized signals for snow retrievals. The vertically integrated radar reflectivity observed by MRR provides an indirect measurement of SWP. Supercooled liquid water during snowfall is independently derived from HATPRO observations. Section 4.1 shows a case study of a single snowfall case, combined with LWP and IWV retrieved from HATPRO. Section 4.2 analyzes the data set of 458 hours snowfall in the whole year 2010, together with synergetic observations performed at UFS. To investigate the dependence of observed polarized signature on snow parameters, TBs at 90 GHz, as well as the 2m-temperature at the summit of Mount Zugspitze, are also examined as a function of PD and TB at 150 GHz.

4.1 Case study: 4 April 2010

In order to illustrate the dependencies of PD and TB on snow parameters, first an example snowfall event on 4 April 2010 is investigated (Figure 4.1). This case will be compared with RT simulations later in Chapter 5. The snowfall event was caused by a low pressure system over southern England moving south-eastwards during the day. A weak cold front passed the UFS at around 15 UTC connected to a temperature decrease from -6°C to -9°C , as reported by the weather observations at the summit of Mount Zugspitze. Temperatures decreased further down to -11°C at midnight. A total snow accumulation of 20 cm was measured for the entire day by the weather observer from the DWD. On 4 April 2010, the snowfall lasted from 11 UTC until 19 UTC. During the time period between 14 and 17 UTC the weather observer reported medium snowfall, while for the remaining time light snowfall was recorded. This was also verified by the two web-cameras of the microwave radiometers. Unfortunately, there is no MRR data available on 4 April 2010.

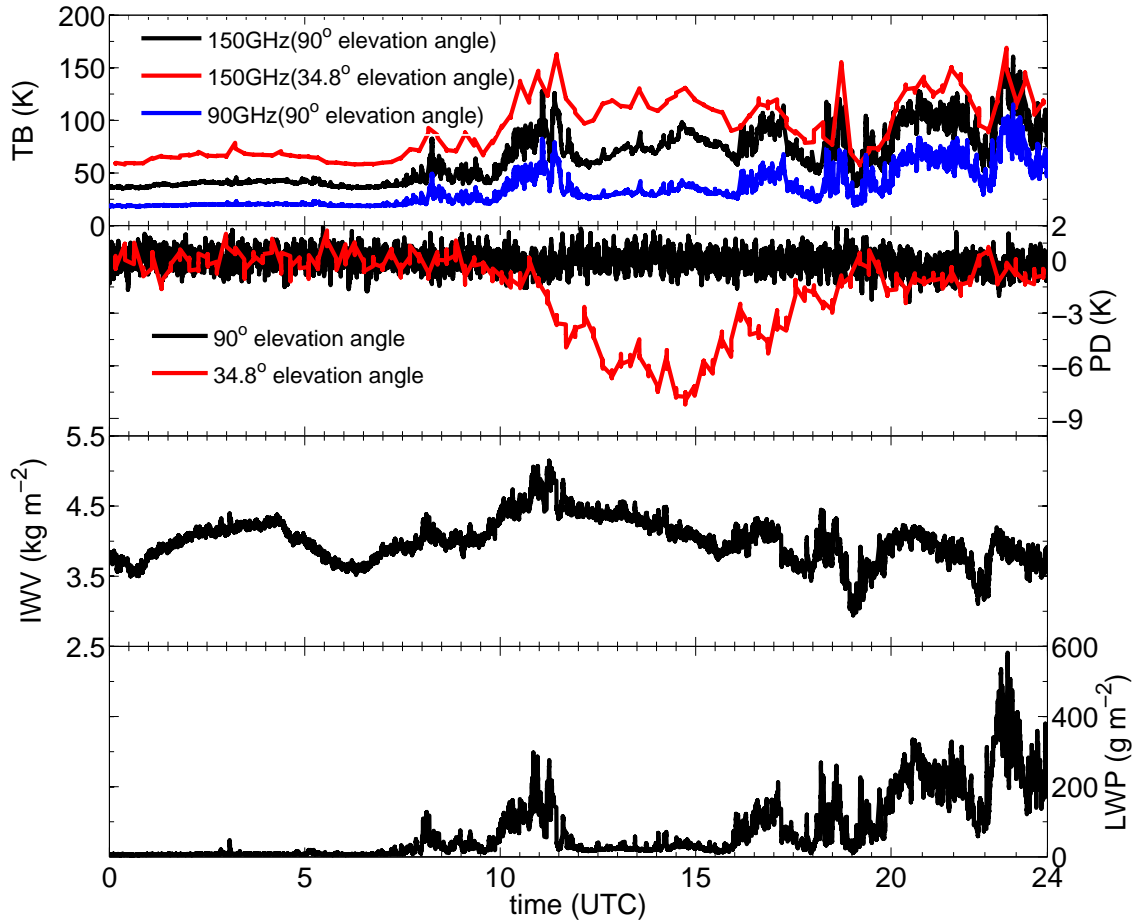


Figure 4.1: Observations on 4 April 2010. From top to bottom: DPR brightness temperatures (TB, in K) at 90 GHz (blue solid line) and 150 GHz (black solid line for 90° elevation angle and red solid line for 34.8° elevation angle); polarization difference (PD, in K) between the vertical and horizontal polarizations at 150 GHz (black solid line for 90° elevation angle and red solid line for 34.8° elevation angle); integrated water vapor (IWV, in kg m^{-2}) and supercooled liquid water path (LWP, in g m^{-2}) derived from HATPRO. (From *Xie et al.*, 2012)

TBs at 150 GHz both in zenith and at 34.8° elevation angle are enhanced during snowfall due to the scattering of the surface thermal emission by snow particles and due to the emission of supercooled liquid water (Figure 4.1). In zenith direction, PDs have a mean value of -0.01 K with a standard deviation of 0.52 K after PD bias correction based on the one-year clear sky cases (Figure 3.1). No significant changes of the zenith PDs are found during snowfall between 11 UTC and 19 UTC. In contrast, PDs at an elevation angle of 34.8° begin to increase when the snowfall starts at about 11 UTC, reach their maximum value up to -8 K at ~ 15 UTC, gradually decrease after 17 UTC, and approach 0 K when the snowfall stops around 19 UTC.

To better interpret the PD signals, LWP and IWV derived from HATPRO are shown in Figure 4.1. IWV decreases continuously from ~ 5.1 kg m^{-2} at the beginning of the snowfall

event to $\sim 3.0 \text{ kg/m}^2$, except for 17 UTC and 19 UTC where IWP values increase by $0.5 \sim 1 \text{ kg/m}^2$. In this case the LWP value reaches up to more than 200 g/m^2 at the beginning of the snowfall event. At $\sim 12 \text{ UTC}$ LWP decreases to the very low value of $\sim 35 \text{ g/m}^2$ and stays constant until 16 UTC. Later, LWP values fluctuate between 30 g/m^2 and 300 g/m^2 . During the 2008/2009 TOSCA campaign at UFS, supercooled liquid water was observed in 75% of all snowfall events and in 60% of these cases SWP was smaller than 50 g/m^2 , but the median LWP was on the order of $\sim 100 \text{ g/m}^2$ (Löhnert *et al.*, 2011). It is interesting to note that the PDs are only observed during very low amounts of LWP. Apparently, the PD signals are masked by the emission due to supercooled water.

4.2 Statistical analysis in 2010

To better understand PD and TB caused by oriented snow particles during snowfall, snow events in the whole year 2010 shown in Figure 3.2 (Section 3.2) are investigated. Using a total of 458 hours snowfall in 2010, a statistical analysis of PDs observed at 150 GHz is presented in this section, together with HATPRO and MRR observations.

LWP reveals strong effects on PD and TB during snowfall, as shown in the case study (Section 4.1). To further verify the effects of LWP in observations, the occurrence of HATPRO derived LWP during snowfall is shown in the top panel of Figure 4.2, using the whole year snowfall data, while the PD occurrence observed by DPR at 150 GHz is in the bottom panel. As can be seen in Figure 4.2, for most of the snow cases in 2010 (more than 85%), the LWP observed by HATPRO is lower than 200 g/m^2 at UFS (Figure 4.2, top panel). The median LWP during snowfall is $\sim 90 \text{ g/m}^2$. Given the retrieval accuracy of HATPRO, “unrealistic” LWP (less than 0) is set to be zero. PD values during snowfall reach up to -10 K for some snow cases, while the majority of PDs are found to be in the range from 0 K to -4 K (Figure 4.2, bottom panel). Note that the occurrence of LWP in Figure 4.2 is shown in the whole snowfall periods while PD only at 34.8° elevation.

In order to find out why the majority of PDs are around -2 K , the dependence of DPR observations on LWP and SWP is analyzed with HATPRO and MRR measurements. All PD/TB combinations at 150 GHz during snowfall are shown in Figure 4.3 at 34.8° elevation angle. The major PDs concentrate at a PD value of around -2 K (Figure 4.3, top panel), which is consistent with the PD occurrence shown in the bottom panel of Figure 4.2. When we look at PD/TB combinations during snowfall as a function of LWP (Figure 4.3, middle panel), it can be clearly seen that supercooled liquid water strongly enhances the TBs due to its strong emission process at 150 GHz. TBs increase by more than 100 K when the LWP increases from 0 g/m^2 to $\sim 800 \text{ g/m}^2$. When LWP increases up to 400 g/m^2 , the maximum PD values are only about -3 K ; PD values are greater than -4 K only when the LWP is lower than 200 g/m^2 . Supercooled water within snowfall enhances TBs but damps the PDs. Another possible hypothesis which could explain low PDs along with high TBs (Figure 4.3, middle panel) is that the higher amount of supercooled liquid water could be associated with a habit change in snow particle shape, from dendritic to heavily rimed particles, which has a great contribution to scattering TB enhancement but could result in a decrease in PDs. The riming effects which can drastically increase the radar attenuation produce strong reflectivity factor by MRR. However, the integrated radar reflectivity $Z_{e, int}$ which is small during the time of higher LWP in the observations contradicts this hypothesis (Figure 4.3, bottom panel).

The influence of cloud liquid water on the PDs is in agreement with the former measurements at lower microwave frequencies in mixed-phase clouds and during rainfall (*Czekala et al., 2001a; Troitsky et al., 2003*). How cloud liquid water can affect PD and TB caused by preferentially oriented snow particles will be further discussed by means of RT simulations in Chapter 5.

The growth of ice particles strongly depends on local temperature and humidity conditions (*Wallace and Hobbs, 2006*), and their falling behavior is subject to the change of particle habit accordingly. Therefore, to examine the dependence of PD/TB combinations on 2m-temperature, the PD/TB combinations are analyzed with the 2m-temperature observed by the weather station at the summit of Mount Zugspitze (Figure 4.4). However, it seems to be difficult to explain the enhanced TBs and PDs with 2m-temperature. Strong PDs up to -6 K could occur at a 2m-temperature of either around $\sim 0^\circ\text{C}$ or down to -10°C . When TBs are enhanced by 100 K by snow scattering and liquid water emission, the corresponding ambient temperature ranges from $\sim 0^\circ\text{C}$ to -15°C .

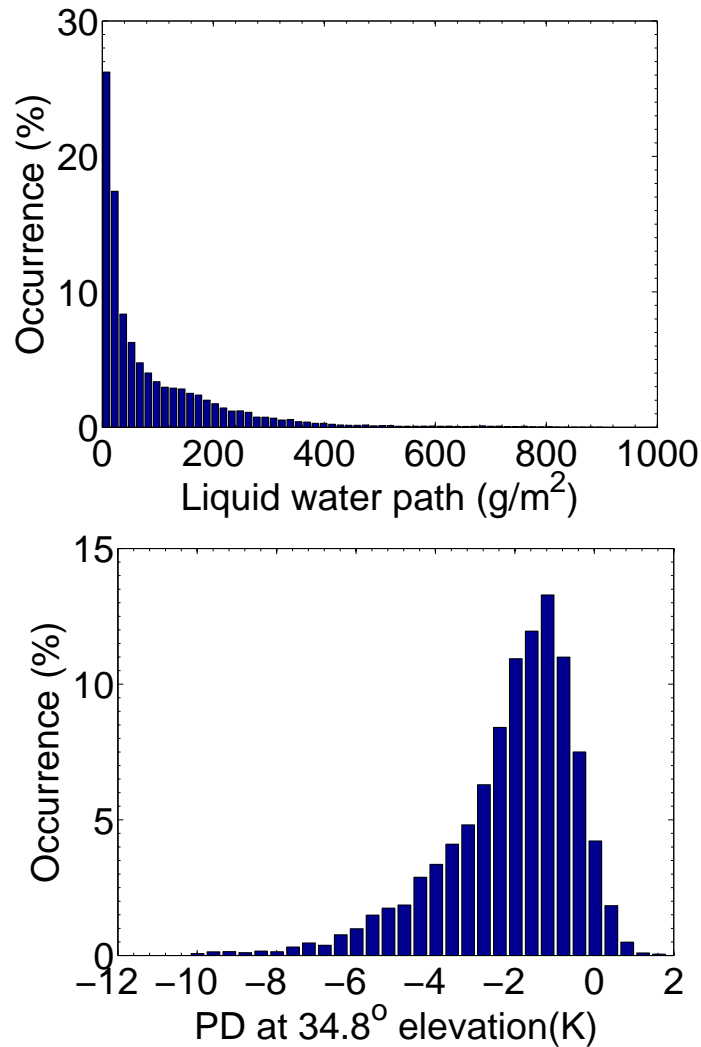


Figure 4.2: Top panel: The occurrence of LWP derived from HATPRO during snowfall in the whole year 2010. Bottom panel: Same as top panel except for the occurrence of PD observed by DPR at 34.8° elevation angle.

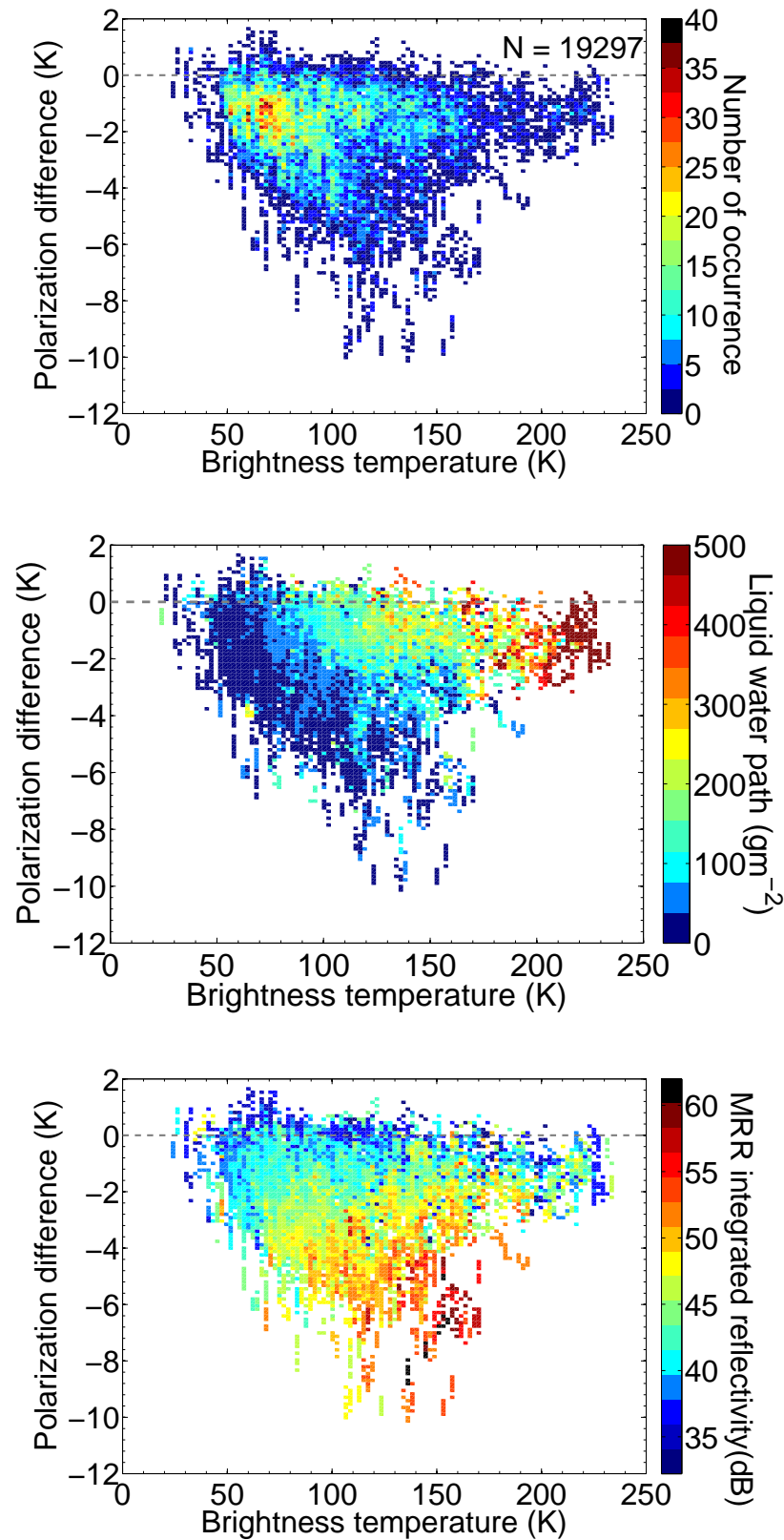


Figure 4.3: Top panel: Number of occurrence of polarization difference and brightness temperature at 34.8° elevation angle at 150 GHz for snowfall cases in 2010. Middle panel: Same as top panel but color shows the simultaneously measured zenith LWP derived by HATPRO. Note that LWP larger than 500 g/m^2 is denoted by the corresponding color at the LWP of 500 g/m^2 . Bottom panel: Same as top panel except color shows the vertically integrated reflectivity factor for the lowest 3 km from the zenith pointing MRR. Missing pixels in the bottom panel are due to MRR data blanks. (From Xie *et al.*, 2012)

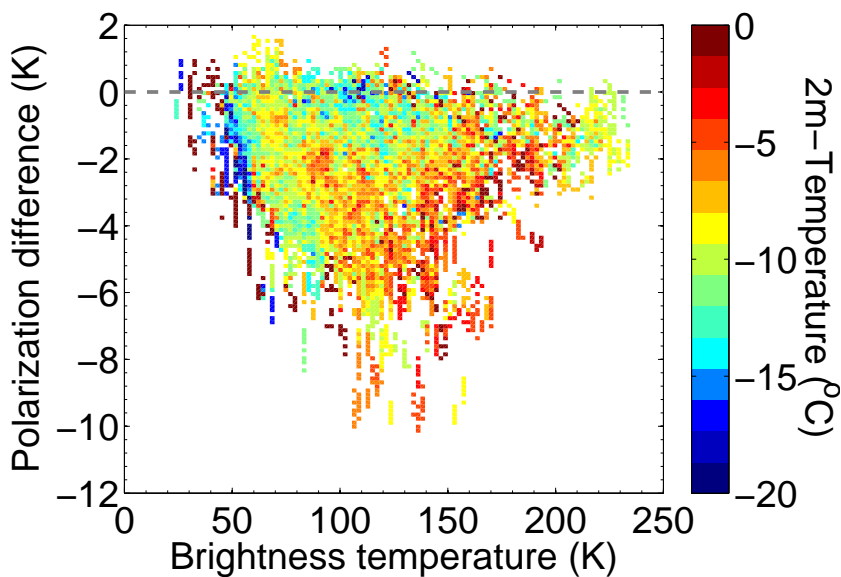


Figure 4.4: Same as Figure 4.3 except that color shows 2m-temperature observed by the weather station at the top of Mount Zugspitze (~ 300 m higher than the UFS). Missing pixels are due to data blanks.

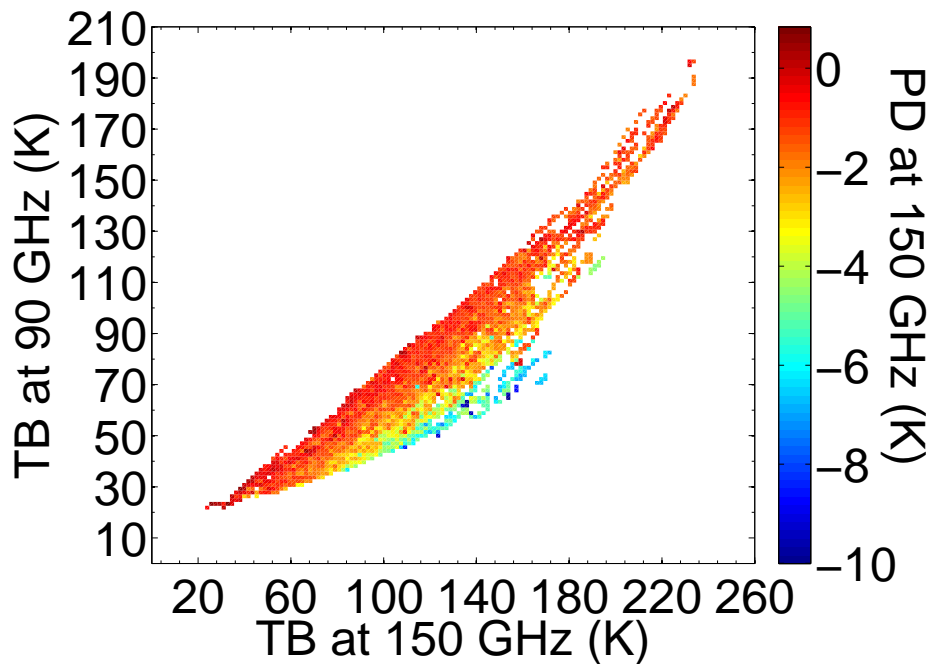


Figure 4.5: PDs as a function of TBs at 90 GHz and 150 GHz for snowfall cases in the entire year 2010. TBs and PDs are shown at 34.8° elevation angle. (From Xie *et al.*, 2012)

DPR also measures TBs at 90 GHz which is less influenced by SWP and has significant contribution from cloud liquid water emission (Löhnert *et al.*, 2011, see Figure 2). To have a deeper insight into the different effects of SWP and LWP on TB and PD, DPR measurement results at 90 GHz are analyzed with PD and TB values observed at 150 GHz at 34.8° eleva-

tion angle (Figure 4.5). The 90 GHz channel of DPR observes synchronously with the two orthogonal channels at 150 GHz. The scattering effects of SWP, which are characterized by high PDs and are at maximum during low LWP, lead to a TB increase from ~ 20 K to ~ 70 K at 90 GHz and from ~ 20 K to ~ 180 K at 150 GHz. The dominant effects, however, result from the strong emission of LWP (TBs at 90 GHz and 150 GHz both increase from ~ 20 K to more than 190 K). Compared to the 150 GHz channels, the snow scattering effects at 90 GHz are weaker (a factor of ~ 3) while the magnitude of TB enhancement due to LWP at 90 GHz is comparable to the corresponding value at 150 GHz.

Illuminated by the effects of LWP and SWP on TBs observed at the 90 GHz channel (hereinafter called TB90), TB90 is plotted as a function of PD/TB combinations at 150 GHz (Figure 4.6). It is much more clear that the increasing LWP is mainly responsible for the increase of TB90, when comparing Figure 4.6 with the middle panel of Figure 4.3. When LWP gradually increases to 500 g/m^2 (Figure 4.3, middle panel), TB90 reaches up to 100 K (Figure 4.6). Whereas, the TB90 is only on the order of 70 K for the strongly enhanced PD during heavy snowfall cases. This result implies that TBs at 90 GHz could be potentially used as additional information for cloud liquid water retrievals during snowfall due to its strong sensitivity to the emission of supercooled liquid water.

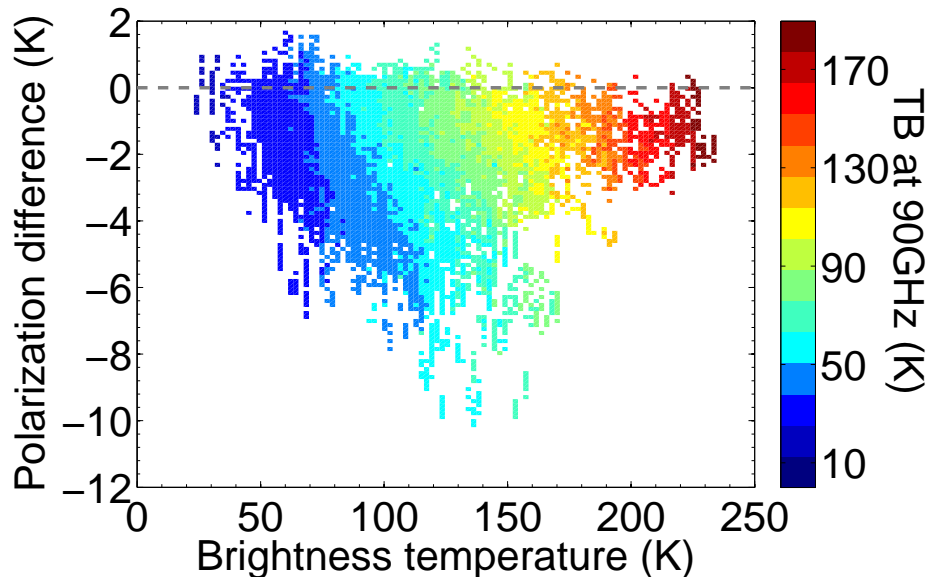


Figure 4.6: Same as Figure 4.3, except that the color shows TBs observed at 90 GHz at the elevation angle of 34.8° .

4.3 Conclusions

Using the instruments described in Chapter 3, this chapter presents polarization observations at 150 GHz analyzed together with the independently derived LWP from HATPRO and integrated radar reflectivity factor from MRR. The analysis of a single snow case and one-year snowfall data in 2010 allows to draw the following conclusions:

- (a) PDs during snowfall have been found to be up to -10 K. These strong PDs occur together with significantly enhanced TB.

- (b) The presence of supercooled liquid water strongly enhances TBs but damps PDs. PDs greater than -5 K are found only when LWP values are less than 200 g/m^2 during snowfall. This result implies that: On the one hand, with significant amount of cloud liquid water, it would be difficult for passive radiometer to detect strong PD due to preferentially oriented snow particles during snowfall. On the other hand, dual polarized instruments with a high accuracy are required to observe polarized signals in snow events accompanied by the frequent presence of cloud liquid water.
- (c) The change of TB90 as a function of PD/TB combinations shows remarkable consistency with the varying LWP (Figure 4.6), compared to the middle panel of Figure 4.3 which shows LWP as a function of PD/TB combination. TB90 has significant contributions from liquid water emission, and the sensitivity of TB90 to LWP can be comparable to the 150 GHz channels (Figure 4.5), while TB90 enhanced by snow scattering is much less prominent. Additional information on liquid water retrievals could be provided by the 90 GHz channel.
- (d) The magnitudes of PDs and TBs are correlated with SWP, which is indirectly related to the MRR integrated reflectivity, since the reflectivity values of the K-band radar are only sensitive to precipitating hydrometeors but not to cloud liquid droplets.

The synergetic observations at UFS provide important information for snow retrievals, and it will be important for future studies to collect detailed information about snowfall type, including vertical properties of clouds and comprehensive in situ observations. Further information concerning snowfall types needs to be provided to confirm the dependence of PD and TB on local atmospheric conditions. The long-term observations of the DPR and HATPRO are now supplemented by a 35.2 GHz cloud radar system which has been operating at UFS since December of 2011.

In the following chapter, RT simulations are performed with a polarized radiative transfer model (Chapter 2). By analyzing the RT results, the study tries to verify the effects of SWP and LWP on PD and TB and to evaluate the sensitivity of PD and TB to snow parameters.

Chapter 5

RT simulations during snowfall

In order to better interpret the observations in Chapter 4, RT simulations performed by the polarized RT model (Chapter 2) are presented in this chapter, assuming that snow particles are preferentially-oriented. In Section 5.1, RT simulations for a single snow event case are performed to analyze the dependencies of PD and TB on SWP and LWP. Then the sensitivities of PDs and TBs to snow microphysical parameters are evaluated by RT simulations (Section 5.2). Considering the frequent presence of cloud liquid water during snow events and its strong effects on PD and TB, Section 5.3 focuses on explaining how supercooled liquid water can affect PD and TB during snowfall. Section 5.4 concludes the study on RT simulations and discusses the uncertainties in the RT simulations. The potential role of PD signals for snowfall retrievals is analyzed in Section 5.5.

5.1 Case study: 4 April 2010

5.1.1 RT setup

In this section, RT simulations for the single snow case shown in Section 4.1 are performed to compare the DPR observations with the simulated results. The atmospheric conditions (i.e., temperature, pressure and humidity profiles) and cloud structures are necessary to be reconstructed as an input for the RT model. For this purpose, the temperature and humidity profiles which are known relatively well are taken from the radiosonde station at München-Oberschleißheim (~ 90 km away from the UFS), while reasonable assumptions on macro-/micro-physical properties of snow and liquid water clouds need to be made.

For the RT simulations, the snow layer is assumed to be located between 2650 m and 4650 m (MSL), i.e., 0 to 2000 m AGL. Unfortunately, no MRR data are available on 4 April 2010. However, according to the whole year MRR data at UFS, the top of the snow layers is usually between 1000 m (AGL) and 2000 m (AGL), and the UFS is almost always within the clouds. As a first approximation, the snow layer is therefore assumed to be located between the UFS height (2650 m MSL) and 4650 m (MSL). Because of their small size and negligible influence at 150 GHz ice crystals within ice clouds are not considered.

In this chapter, snow scattering properties of oriented snow particles are calculated by the T-matrix method which is described in Section 2.3. The current observations performed at UFS do not offer enough information to characterize the typical snow particle habit and orientation

during snowfall. For this reason, the DDA method is not used to calculate the scattering properties for complex particle shapes during snowfall. The DDA method is computationally time consuming, especially for large particle sizes up to 1 cm at 150 GHz. The cost/benefit ratio for oriented dendrites and other particles is not warranted until realistic snowflake shapes for the snow events at UFS are known. Snow particles therefore are assumed to be horizontally oriented soft oblates with a specified aspect ratio (AR) in this study, i.e., the ratio of the minimum dimension to the maximum dimension. Airborne observations indicate the AR of ice particles in the range of 0.6 – 0.65 (*Korolev and Isaac, 2003*), with the AR of ice particles in general decreasing with the increase of maximum dimension. *Hogan et al. (2012)* showed AR decreasing to 0.4 at the maximum dimensions of 4000 μm using the data collected by the aircraft in situ probes in England. A low AR of 0.4 was also found for snow particles at the maximum dimension of 8000 μm during the TOSCA campaign with the 2-Dimensional Video Disdrometer (2DVD) (*Siebler, 2010*). As a compromise between the different values reported in previous studies, the snow particles are assumed to have a fixed AR of 0.5. The sensitivity of PD and TB to AR will be discussed later in Section 5.2.1.

The scattering properties of horizontally aligned oblates are calculated with the T-matrix method (*Mishchenko, 2000*). The mass size relationship for snow particles is provided by *Matrosov (2007)*:

$$\begin{aligned} m &= 0.003D^2 \quad (0.01 < D \leq 0.2) \\ m &= 0.0067D^{2.5} \quad (0.2 < D \leq 2.0) \\ m &= 0.0047D^3 \quad (D > 2.0) \end{aligned} \tag{5.1}$$

where D (in cm) and m (in g) the maximum size of oblate is the mass of the oblate, respectively. The Matrosov mass size relationship is fully listed here although particle dimensions larger than 2 cm are not considered in this study.

The refractive index of snow particles is calculated according to the Maxwell-Garnett mixing rule, where the refractive index of snow particles is given as a function of ice volume fraction, and ice was selected as the inclusion (e.g. *Matrosov, 2007; Hogan et al., 2011*). The pure ice permittivity is calculated using the model given by *Mätzler (2006)*.

The maximum dimension of the snow oblates is assumed to range from 250 μm to 10000 μm with an assumed exponential size distribution,

$$N(D) = N_0 \exp(-\Lambda D) \tag{5.2}$$

where the intercept parameter N_0 (in m^{-4}) is assumed to depend upon atmospheric temperature according to *Field et al. (2005)*; D (in cm) is the maximum dimension of the snow oblate; the slope coefficient Λ (in cm^{-1}) can be calculated from Equation 5.1 together with the assumed SWP.

Supercooled water is assumed to be located at the top of snow layer (4650 m – 5150 m MSL) since supercooled liquid water tends to concentrate at the cloud top (*Rauber and Tokay, 1991; Fleishauer et al., 2002*). Supercooled water droplets are assumed to be monodispersed spheres with a radius of 10 μm . The temperature of the supercooled water layer is 244 K. The refractive index of supercooled liquid water is computed according to *Ellison (2006)*. The gas absorption due to oxygen, nitrogen and water vapor in the atmosphere is calculated using the absorption model from *Rosenkranz (1998)*.

5.1.2 RT results

To interpret polarization observations during snowfall at UFS, RT simulations are performed to compare with the example snow case shown in Chapter 4. Snow particles are assumed to be horizontally-oriented. To evaluate the effects of SWP and LWP on PD and TB, radiative transfer calculations were carried out for the realistic range of LWP ($0 - 400 \text{ g/m}^2$) and SWP ($0 - 1000 \text{ g/m}^2$), by means of the RT model (*Evans and Stephens, 1995b*). The RT model and its solution to the polarized RT equation has already been introduced in Chapter 2.

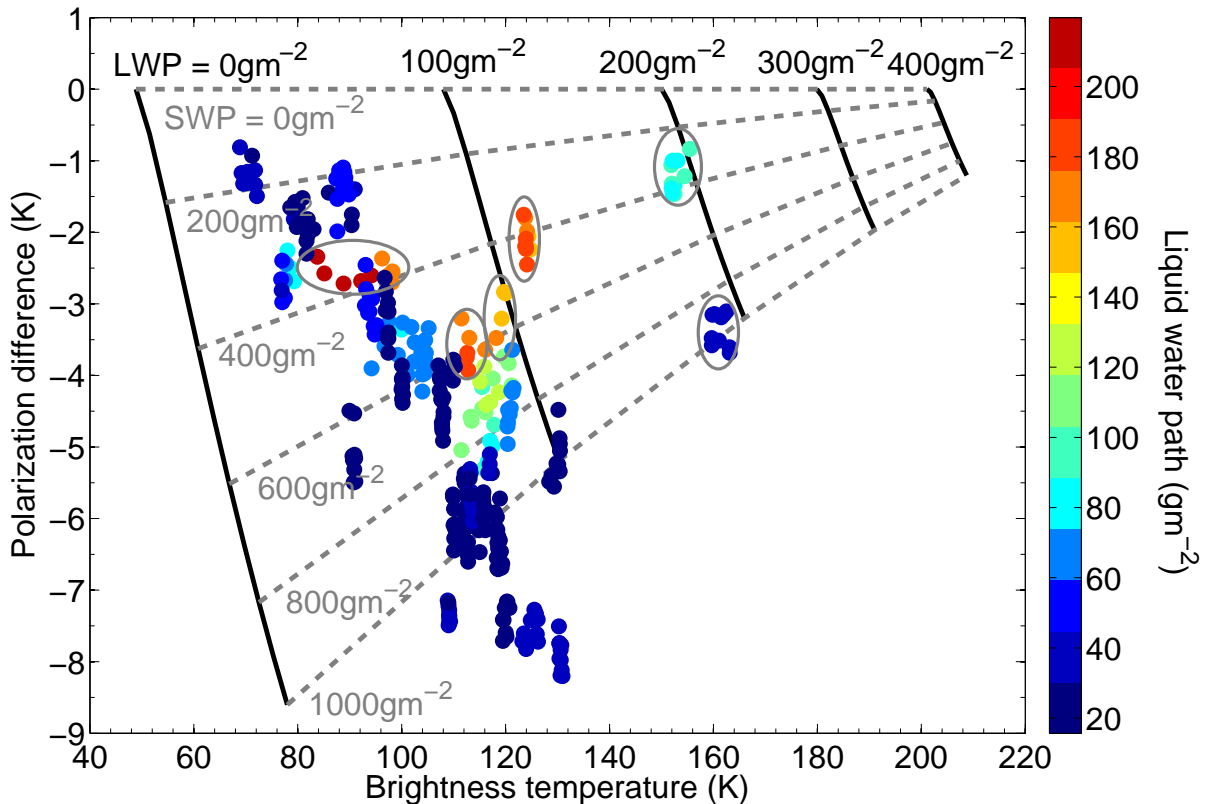


Figure 5.1: RT simulation results for 4 April 2010 at 150 GHz. The solid black lines are the contours of LWP ranging from 0 to 400 g/m^2 ; the dashed gray lines are the contours of SWP ranging from 0 to 1000 g/m^2 . Note that the RT simulations are at 32° elevation angle because the Lobatto quadrature used in RT4 model provides simulation at 16 angles in hemisphere and the closest one to 34.8° elevation is 32° . The colored dots represent DPR measurements between 11 UTC and 19 UTC; colors indicate the corresponding zenith LWP derived from HATPRO using the “closest time match” rule. The data points enclosed with gray ellipses are from the beginning or the end of the snowfall event when LWP changes rapidly. (From *Xie et al., 2012*)

With the given assumptions described above (Section 5.1.1), Figure 5.1 shows that unique values of both SWP and LWP can be determined with a given observation of TB and PD. In the absence of liquid water the TB is enhanced by about 30 K when SWP increases from 0 to 1000 g/m^2 . At the same time, PD increases from 0 to $\sim -9 \text{ K}$. In snow free conditions TB strongly increases with increasing LWP, up to 200 K at an LWP value of 400 g/m^2 . With

the increase of LWP during snowfall, PD and TB both shift: the PDs decrease while the TBs increase. Supercooled liquid water enhances the TB and damps the PD, which is consistent with measurements investigated in Chapter 4.

The projection of the observations (Figure 4.1) into Figure 5.1 allows to check the consistency of measurements and model results. For the snowfall period on 4 April 2010, i.e., between 11 UTC and 19 UTC, the measurements also show that PDs between -6 K and -9 K can only be found for HATPRO zenith LWP values lower than 50 g/m^2 (Figure 4.1). However, there are HATPRO LWP measurements of about 50 g/m^2 where the model would require 200 g/m^2 to explain the observed TB and PD.

The mismatch between the model and observation of LWP (data points enclosed by ellipses in Figure 5.1) is most likely due to the different observation geometries. LWP is measured at zenith, while PD and TB at 150 GHz is observed at 34.8° slant path. The discrepancies of observations between different elevation angles increase if the cloud field is horizontally inhomogeneous. The rapid changes of LWP at the beginning (from 11 UTC to 12 UTC) and at the end (from 17 UTC to 19 UTC) of the snowfall event shown in Figure 4.1 bring forth this LWP mismatch. If analyzing the time window of ± 2 minutes before and after the

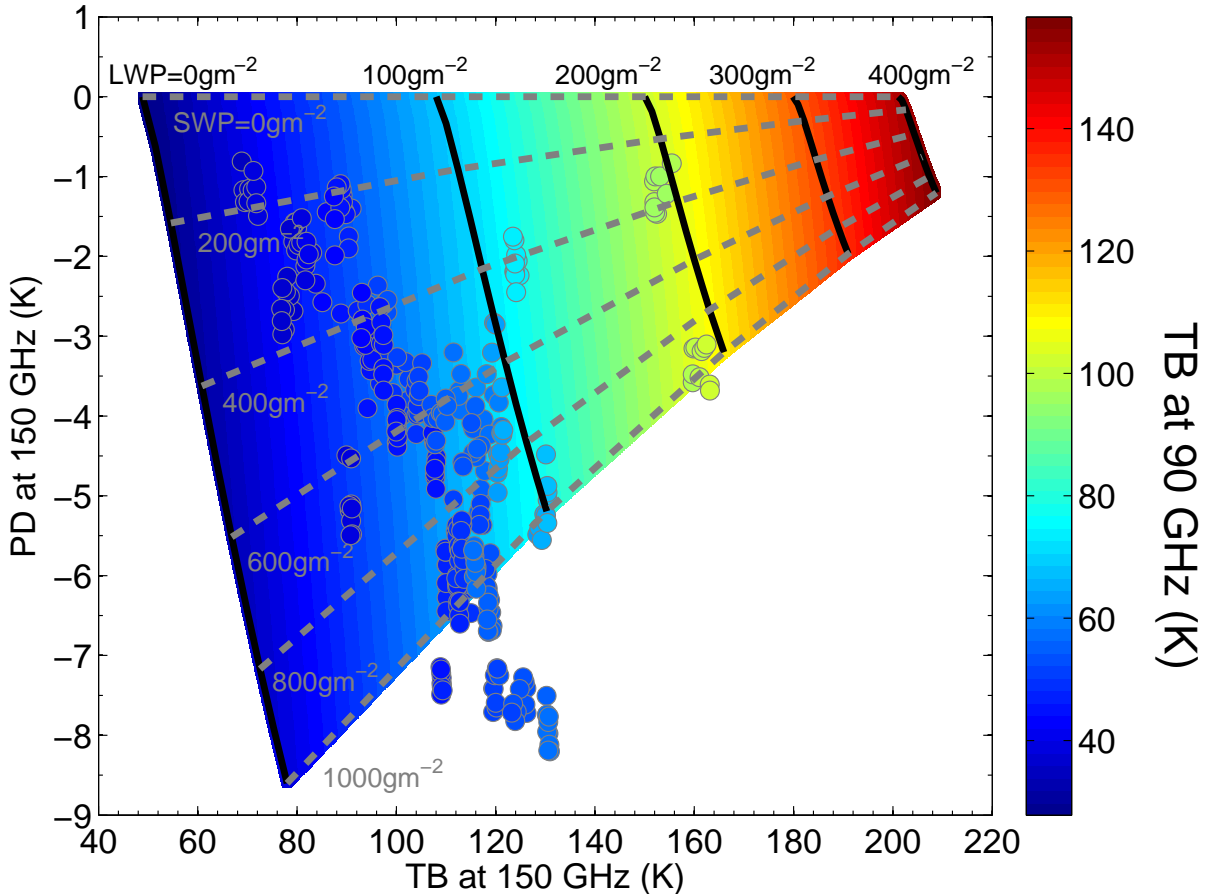


Figure 5.2: Same as Figure 5.1, except that the color shows TB at 90 GHz. The colored dots with gray marker edge is the DPR measured TBs at 90 GHz at 34.8° elevation angle between 11 UTC and 19 UTC on 4 April 2010, and the background colors show RT simulated TBs at 90 GHz with the assumptions described in Section 5.1.1.

closest DPR time, the LWP derived from HATPRO varies from $\sim 60 \text{ g/m}^2$ to $\sim 200 \text{ g/m}^2$. This may be explained by varying cloud structures close and further away from the mountain slopes.

To verify the assumption of the LWP mismatch between HATPRO observations and RT simulations that caused by different observation geometries, Figure 5.2 shows the observed TBs at 90 GHz (colored dots highlighted by gray edge) as a function of TBs and PDs at 150 GHz. The background colors in this figure indicate TB90 interpolated on the basis of RT simulations. The 90 GHz channel would be helpful to avoid the LWP mismatch which is caused by different observation geometries (data enclosed by the ellipses in Figure 5.1), since it is mostly sensitive to the LWP (Figure 4.5 and Figure 4.6) and observes synchronously with the two orthogonal channels at 150 GHz. An increase of LWP by 100 g/m^2 causes that the corresponding TB90 is enhanced on the order of 30 K, while TB90 due to an increase of 100 g/m^2 SWP is enhanced less than 10 K. When the LWP changes rapidly at the beginning and at the end of the snow event on 4 April 2010 (i.e., 11 – 12 UTC and 16 – 19 UTC in Figure 4.1), strongly enhanced TB90 which is observed by DPR is mainly caused by high LWP values in clouds due to the channel sensitive response to LWP at 90 GHz, and vice versa. Therefore, by using this information provided by the 90 GHz channel, the LWP mismatch (enclosed by ellipses in Figure 5.1) could be avoided. The results also imply that for future campaigns synchronous scanning strategies are essential, especially in regions with strong orographic structure.

Another mismatch of the PDs (data points of low measured LWP below 1000 g/m^2 SWP contour in Figure 5.1), which is underestimated in radiative transfer simulations, might be due to the underestimation of snow particle scattering when using Maxwell-Garnett mixing formula. Compared to the complex ice and air geometry (e.g., the DDA method), homogeneously mixed ice/air particles underestimate the PDs as well as the TBs in the simulations, especially at higher microwave frequencies. This could explain why the RT simulations can only show a TB enhancement of $\sim 30 \text{ K}$ due to a SWP of 1000 g/m^2 at 34.8° elevation angle at the frequency of 150 GHz. A further analysis on how the Maxwell-Garnett mixing formula weakens snow particle scattering will be given later in Section 5.2.3. Another reason for the mismatch could be the simplified snowflake model, which assumes that snowflakes are soft oblates with a perfectly horizontal orientation and a fixed AR in this case study, while the realistic snow particle habits are far more complicated during snowfall. To investigate the effects of the snow particle parameter model on PD and TB, the following section discusses the possible uncertainties in snow parameters and their corresponding influences on PD and TB (Section 5.2).

So far the results at the specific elevation angle of 34.8° are shown. In order to show the information content that is contained in the PDs as a function of different elevation angles, measurements between 16 UTC and 16:30 UTC are shown in Figure 5.3. Observations are shown together with RT4 simulations for different AR and SWP. The simulation input parameters for SWP and LWP are selected according to the best fit with the observations in Figure 5.1, i.e., $400 \text{ g/m}^2 - 600 \text{ g/m}^2$ for SWP and 100 g/m^2 for LWP. The maximum PD in the observations and simulations is found at $\sim 30^\circ$ elevation angle. The simulated PDs for an AR of 0.5 seem to fit to the measurements best while PDs with an AR of 0.6 are $\sim 1 \text{ K}$ lower. Since SWP also enhances PDs, SWP ranges from original 400 g/m^2 to 600 g/m^2 , and even this increase of SWP can not sufficiently increase the observed PD values when an AR of 0.6 is assumed.

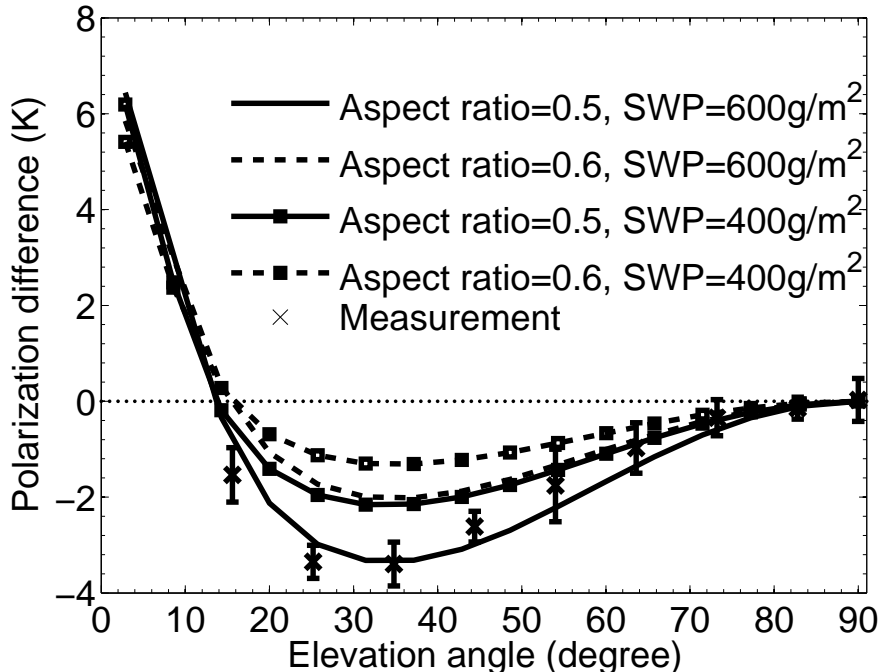


Figure 5.3: Polarization difference as a function of elevation angle at 150 GHz. The solid lines are simulated with an AR of 0.5 while the dashed lines with an AR of 0.6. The lines with squares corresponds to an SWP of 400 g/m². The observations (crosses) are shown for the time period between 16 UTC and 16:30 UTC on 4 April 2010 (mean values and standard deviations), and the TBs during this period are in the range of 94 K to 105 K. The dotted line indicates zero polarization difference. (From *Xie et al.*, 2012)

5.2 Sensitivity of PD and TB to snow parameters

The macro-/micro-physical parameters of snow particles, which determine their scattering characteristics, play a central role in the RT process. An simplification of cloud assumptions in the RT model could result in large uncertainties in PD and TB, and further deteriorate the accuracy with significant errors in retrievals.

To examine the effects of different critical snow parameters on PDs and TBs in RT simulations, a sensitivity study is performed in this section. The different input parameters for the RT simulations include snow particle AR, snow particle canting angle, mass size relationship, supercooled liquid water, surface emissivity and intercept parameter in the exponential size distribution. The “standard TB” is calculated with the “original” settings as described in Section 5.1.1, i.e., Matrosov snow particle with an AR of 0.5, perfectly horizontally oriented oblates, supercooled water refractive index model by *Ellison* (2006), intercept parameters on the order of 10^7 m^{-4} , surface emissivity of 0.9. The other settings, like particle size distribution, are the same as the RT simulation setup for the case study described in Section 5.1.1. For the sensitivity of PD and TB to one input parameter in RT simulations, other parameters remain the same as the “original” settings.

Supercooled liquid water was frequently observed during snowfall (Section 4.2). In the snow events during the TOSCA campaign 2008/2009, the median LWP was reported on the order of 100 g/m² (*Löhnert et al.*, 2011), which was on the same order in 2010, as described in

Section 4.2. Therefore, the SWP and LWP for RT simulations are assumed to be 600 g/m^2 and 100 g/m^2 , respectively. The SWP is located between 0 m and 2000 m (AGL). The LWP is homogeneously distributed above the snow layers within a height of 500 m. Supercooled liquid water is supposed to consist of monodispersed spherical particles with a radius of $10 \mu\text{m}$. Note that, the PDs and TBs shown in this section are all simulated at the elevation angle of 32° from the ground-based microwave radiometer at 150 GHz.

5.2.1 Aspect ratio

Snow particle AR tends to decrease with an increasing particle size, which is detected by ground-based and air-borne observations (Siebler, 2010; Hogan *et al.*, 2012). The AR value is reported to be down to ~ 0.4 when the particle size is larger than $4000 \mu\text{m}$ (Section 5.1.1). To examine the effects of snow particle AR on TB and PD, a reasonable range of AR is assumed in this section, i.e., from 0.3 to 1.0.

Figure 5.4 shows RT simulated PDs and TBs due to horizontally oriented particles with different AR values. When the snow particle AR increases from 0.3 to 1.0, i.e., snow particles become rounder, the difference of TBs between the two orthogonal polarizations is narrowed down, as can be seen in the top panel of Figure 5.4. PD due to spheres is $\sim 7 \text{ K}$ lower than in case of horizontally-oriented particles with an AR of 0.3. This is because the dichroism effects of these particles decreases significantly when snow particles become spherical.

PD and TB are also shown as a function of elevation angle in Figure 5.4. For all ARs, PD at zenith (90° elevation angle) is equal to zero, due to the azimuthally symmetric atmosphere. When the observation geometry changes gradually from vertically pointing to horizontally pointing, i.e., the elevation angle decreases from 90° to 0° , the induced PD first increases, reaches a maximal value and then decreases. Assuming the particle AR of 0.4, PD gradually increases when the elevation angle decreases from 90° elevation angle to 40° , reaches a maximal of $\sim -5 \text{ K}$ at $\sim 35^\circ$ elevation and then its value is reduced to zero. When the observation approaches the horizontal direction (lower than 10° elevation angle), PD observed from ground becomes positive, and the received radiation at the vertical polarization is higher than at the horizontal polarization. PD values reach up to more than $+3 \text{ K}$, even for spherical particles with an AR of 1.0 (Figure 5.4, top panel). It is interestingly noticed that the maximum PD values occur between an elevation angle of 20° and 50° , even though particle AR varies from 0.3 to 1.0. This specific behavior of PD suggests that for future snowfall observations an optimal elevation angle to observe maximum PDs ranges from 20° to 50° .

TBs calculated at an AR of 0.5 are taken as “standard values” at the corresponding elevation angles. Thus, δTB at the AR of 0.5 is zero in the bottom panel of Figure 5.4. The decreasing AR weakens the scattering effects of snow oblates. Therefore, the flatter oblates which have stronger scattering effects enhances stronger TBs than rounder particles (Figure 5.4, bottom panel). The TB difference between spheres and particles with an AR of 0.3 is up to 9 K . Decreasing particle AR from 0.6 to 0.5, i.e., flatter snow particles, enhances PD by 1.3 K while the TB increases by 1.7 K at 32° elevation.

The behavior of PDs and TBs due to different AR can be explained by scattering characteristics of snow particles, which are related to their extinction and scattering matrices (Chapter 2). Due to the strong scattering effects, snow extinction mainly results from scattering effects. The absolute value K_{12} of the extinction matrix (described in Section 2.3), which is generally connected to polarization characteristics, decreases with an increasing AR at an elevation angle ranging from 0° to 90° , and hence causes that PD decreases with the

increase of particle AR. The extinction matrix element K_{11} , which is associated to the total radiation, i.e., TBs, also decreases with the increase of snow particle AR. Therefore, the PD and TB values both decrease when snow particles become rounder. The PD changes from negative to positive when the elevation angle is close to 0° . This is mainly caused by the scattering matrix element M_{12} (Section 2.3) which changes with elevation angle. For spheri-

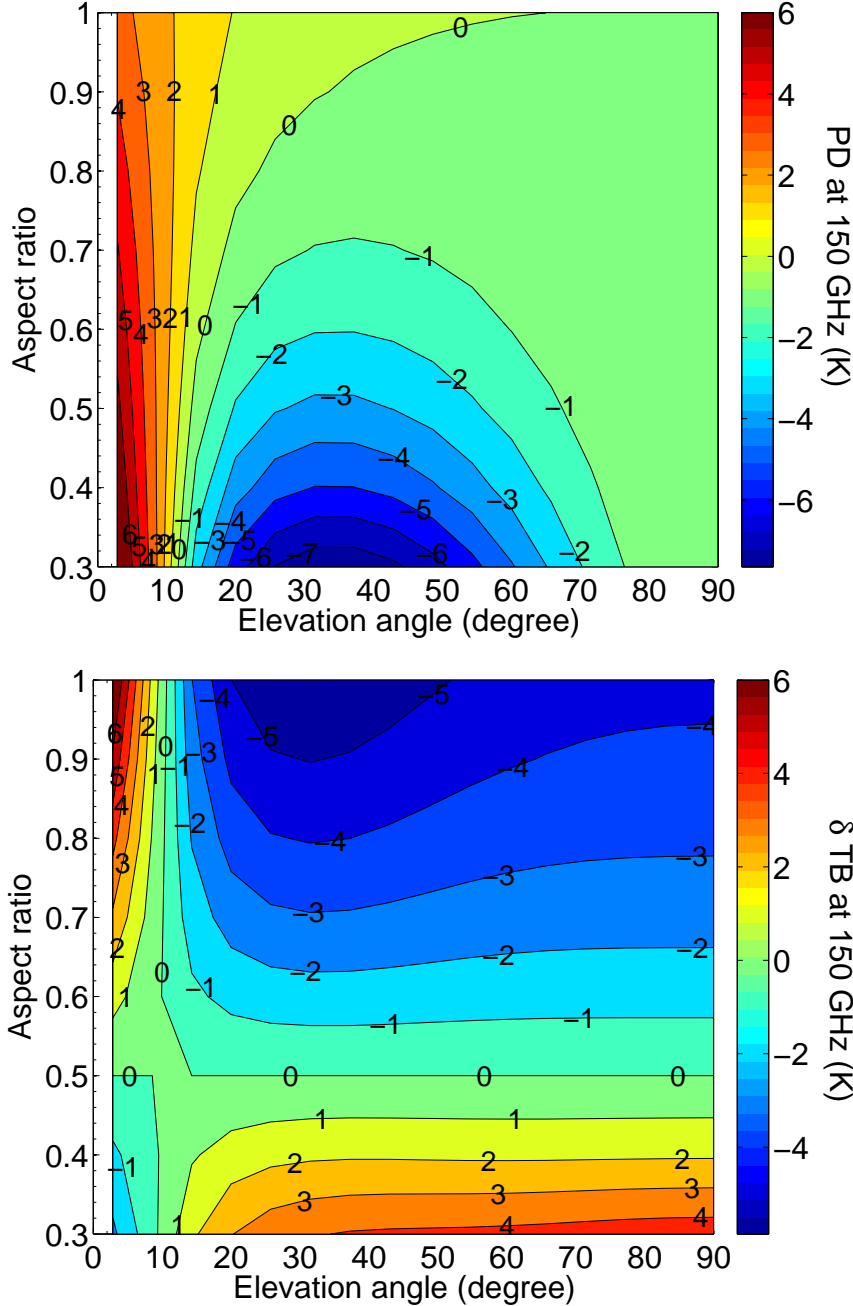


Figure 5.4: Top panel: PD at 150 GHz as a function of snow particle AR and elevation angle. Bottom panel: The change of TBs (δ TB) as a function of snow particle AR and elevation angle, compared to the “standard” TBs calculated with snow particle at an AR of 0.5 at the corresponding elevation angles. Note that the modeled particles are horizontally-aligned snow oblates.

cal particles, M_{12} normally reaches a maximal value at the scattering angle of $\sim 90^\circ$, i.e., the maximal PD value for spheres occurs near the horizontally-viewing observations.

5.2.2 Particle canting angle

The aerodynamic forcing causes snowflakes falling with their major dimension horizontally aligned (*Pruppacher and Klett, 1997*). However, with the presence of strong turbulence snow particles could begin tumbling during their falling process, and the tumbling can further affect particle scattering characteristics in RT simulations. To quantify the effects of varying snow particle orientation, the following study investigates the sensitivity of PD and TB to particle orientation.

Particle orientation is specified by its canting angle, which is defined as the tilted angle of the particle major axis away from the horizontal orientation. The canting angle ranges from 0 to π , and usually it can be reduced to be in the interval between 0 and $\pi/2$ if particles have symmetric characteristics. For the horizontal orientation (vertical orientation), particle canting angle is equal to 0° (90°). The orientation of snow particle can be defined by the three Euler angles in the algorithms that calculate scattering properties (Figure 2.7). Two of the Euler angles, β and ϕ , are supposed to be uniformly distributed in the range of 0 and 2π since the atmosphere is plane-parallel and azimuthally symmetric, and the third Euler angle θ is used in this section to specify the canting angle of particles, i.e., their orientation.

To analyze the effects of particle orientation on RT simulations, snow particles are assumed to be oblates with the same aspect ratio of 0.5. RT simulated TBs and PDs, which are illustrated as a function of particle canting angle in Figure 5.5, are calculated at a single canting angle, i.e., all snow particles during snowfall tilt ideally at the same canting angle. When snow particles tilt away from the horizontal orientation, the sign of PD changes gradually from negative to positive, as can be seen at 30° elevation angle (Figure 5.5, top panel). This is caused by the changing dichroism characteristic of preferentially oriented snow oblates. When particles are horizontally-oriented, more horizontal radiation is scattered backwards to the ground surface and the PD value observed from upward viewing on the ground is negative. For particles with vertical orientation, the radiance at vertical polarization is predominant and radiation at vertical polarization is larger than at horizontal direction, when observing from the ground based perspective (Figure 5.5, top panel).

The TB change due to the changing particle orientation is prominent. The variation of TB is on the order of 3 K, when snow particles tilt away from horizontal orientation to vertical orientation (Figure 5.5, bottom panel). This can be already detected by the present instruments which usually have a sensitivity around 1 K.

However, in reality, snow is usually composed of a mixture of snow particles with different shapes and orientations. To further examine the effects of particle orientation on PD and TB, the distribution of snow particle orientations are assumed to follow a truncated Gaussian function (*Miao et al., 2003*), and the weighting for each canting angle can be expressed by

$$p(\theta) = C_0 e^{-\frac{(\theta-\bar{\theta})^2}{2\theta_\delta}}, \quad 0 \leq \theta \leq \pi/2 \quad (5.3)$$

where C_0 is a normalized constant, θ_δ is the width parameter (WP) in Gaussian distribution, and the mean value $\bar{\theta}$ is supposed to be zero.

Figure 5.6 shows the schematic diagram of the truncated Gaussian function when WP varies. For WP=0, only horizontally oriented particles exist and the weight $p(0^\circ)$ equals one only at

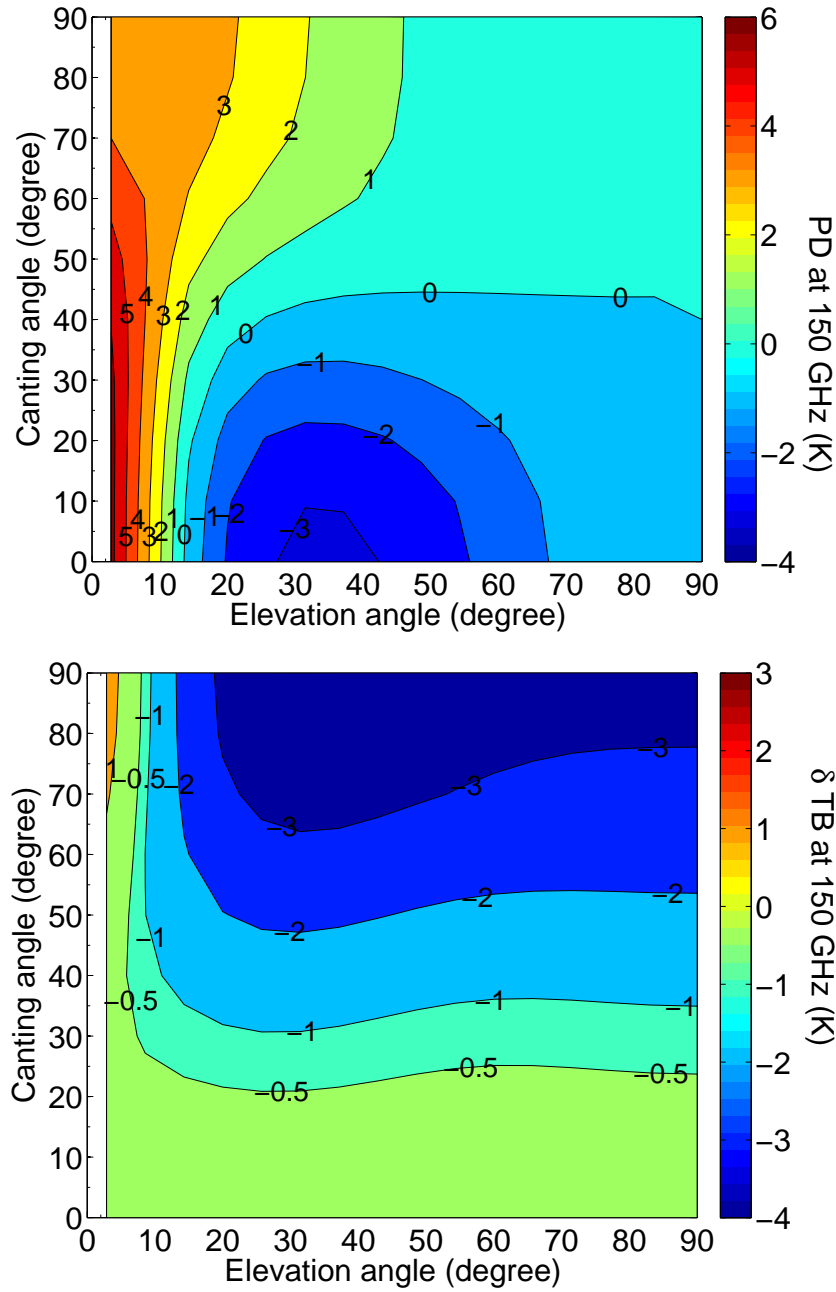


Figure 5.5: Top panel: PD at 150 GHz as a function of particle single canting angle and observation elevation angle. Bottom panel: The change of TBs (δ TB) as a function of snow particle canting angle and elevation angle, compared to the “standard” TBs calculated at a snow particle AR of 0.5 at the corresponding elevation angle when the canting angle of particles is assumed to be 0° . Note that all snow particles are assumed to be snow oblates with an AR of 0.5.

$\theta = 0^\circ$, while at other canting angles the weights are all null. Changing WP from 0 to infinite, snow particles tend to orient from perfectly-horizontally to randomly. Scattering effects from particles with high canting angles gradually pose significant contribution, and the weighting from high canting angles becomes more important when WP begins to increase to infinite.

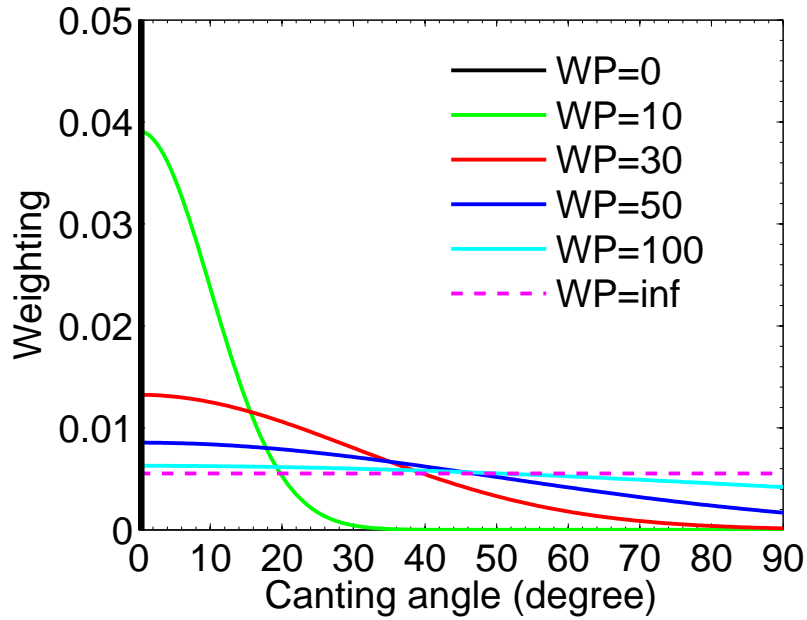


Figure 5.6: Weights of truncated Gaussian function as a function of particle canting angle.

PDs caused by snow particles with preferred orientation ($WP \neq \text{infinity}$) are generally larger than in case of random orientation ($WP = \text{infinity}$). The stronger scattering effects due to preferentially oriented particles results in larger PD and TB than particles with random orientation. When snow particles are all horizontally aligned, their dichroism effects cause PD values up to 3 K (Figure 5.7, top panel). When the oblates tends to become randomly oriented, the PD value begins to decrease with the increasing WP. Decreasing WP from 50 to 0, the change of PD is more than 2 K at the elevation angle of $\sim 30^\circ$.

For TB, the enhancement of TB is gradually reduced when particles tend to be randomly oriented. This can be explained by the scattering effects of randomly oriented oblates which are weaker than in case of preferential orientation (Figure 5.7, bottom panel). Compared to particles with horizontal orientation (“standard TB”, solid black line in the bottom panel of Figure 5.7), TB enhancement caused by randomly oriented particles is ~ 2 K lower. It is noticed that particle orientation has a more significant effect on PD than on TB, by a factor of ~ 2 .

5.2.3 Mass size relationship

An accurate knowledge of snow microphysical properties is necessary to evaluate and improve weather and climate models (Heymsfield *et al.*, 2010). One of the critical components for snow microphysics is the snow density, which connects snow mass to snow particle size, i.e., the mass size relationship. Several previous studies tried to find a “universal” mass size relationship to characterize frozen hydrometeors. However, the mass size relation strongly depends on observational sites and local atmospheric conditions (Matrosov, 2007; Woods *et al.*, 2007; Heymsfield *et al.*, 2010).

Given these findings, two frequently used mass size relationships, i.e., *Brown and Francis* (1995) and *Matrosov* (2007), are discussed in this section to examine their effects on PD and

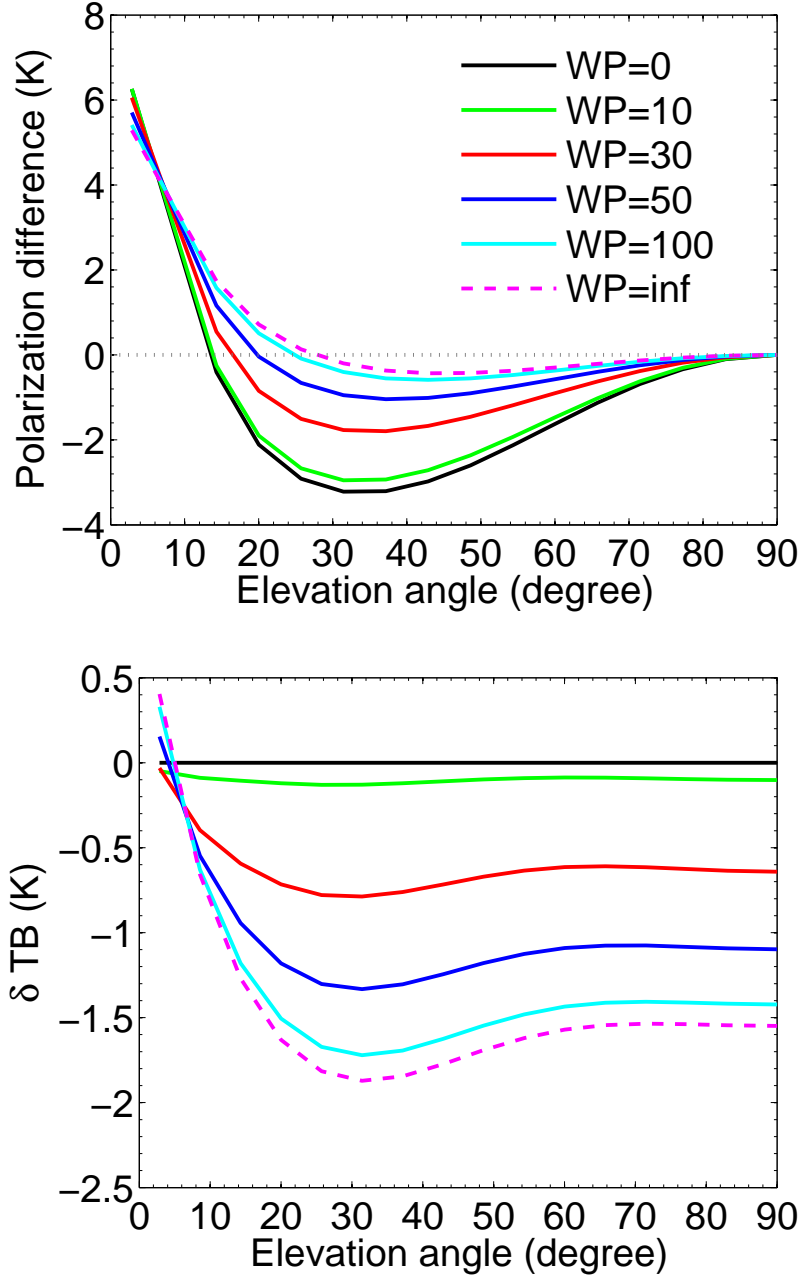


Figure 5.7: Effects of snow particle orientation on PD and TB. With the increase of the width parameter (WP) in truncated Gaussian function (from 0 to infinite), snow particles change gradually from perfectly horizontally oriented to randomly. δTB is the calculated TB compared with the standard TB calculated with horizontally-aligned snow oblates.

TB.

$$\begin{aligned}
 m &= 0.48D^3 (D < 0.0066) \\
 m &= 0.0019D^{1.9} (D \geq 0.0066)
 \end{aligned}
 \tag{5.4}$$

where D (in cm) and m (in g) are the maximum dimension of oblates and the oblate mass, respectively. The mass size relationships are shown in Figure 5.8.

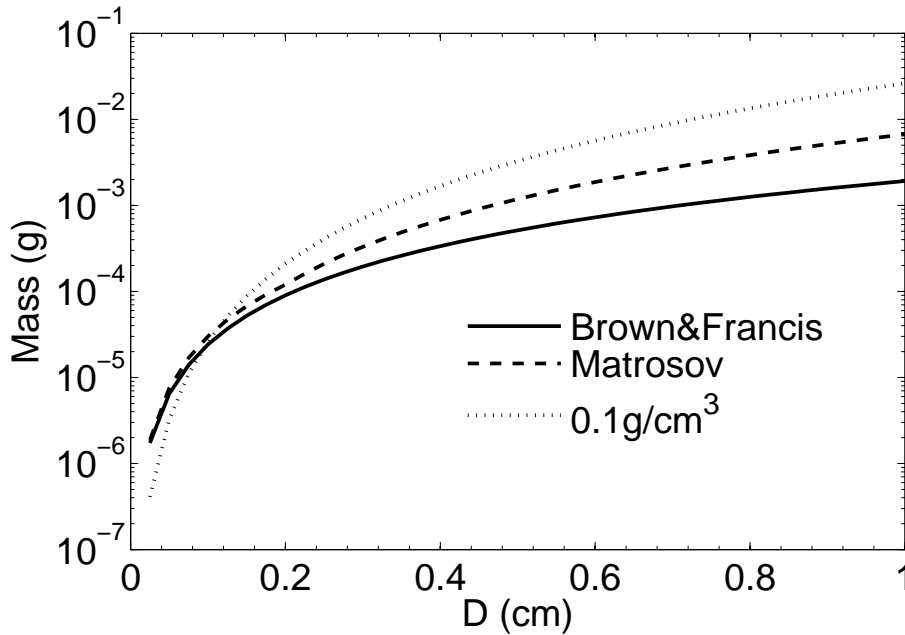


Figure 5.8: Snow particle mass as a function of particle maximum dimension with different mass size relationships (*Brown and Francis*, 1995; *Matrosov*, 2007). Snow particles are assumed to be oblates with an AR of 0.5.

Keeping SWP and LWP constant in the RT model, changing the mass size relationship, e.g., from *Matrosov* (2007) in Equation 5.1 to the less “dense” *Brown and Francis* (1995) (or *Hogan et al.*, 2011) in Equation 5.4, causes a 0.94 K lower PD and a 3.1 K lower TB at the elevation angle of 32°.

The effect of the mass size relationship can be explained as follows: The radiation observed by ground-based instruments is enhanced by the scattering of snow particles existing in the atmosphere. The stronger the scattering from snow particles, the higher the TBs. The refractive index for snow particles is assumed to be a function of ice volume fraction according to the Maxwell-Garnett mixing rule (*Matrosov*, 2007), and it decreases as the particle density decreases. Thus, different mass size relationships especially affect the particle refractive index which finally changes the PDs and TBs. Fluffier particles (*Brown and Francis*, 1995), which have lower density than those using the *Matrosov* mass size relationship (Figure 5.8), lead to lower snow refractive index and weaken the scattering effects of snow particles. Therefore, TB enhancement due to the scattering effects is also reduced, i.e., the PDs and TBs are lower than the original values calculated with the *Matrosov* model. A higher particle density increases the TB and PD enhancement, which is especially significant for the larger particles. In the *Matrosov* mass size relationship, the particle density is less than 0.1 g/cm³ when the maximum dimension of snow particle size exceeds 0.11 cm (Figure 5.8). The refractive index of *Matrosov* snow particle decreases as the increase of particle size, while for particles with a fixed density of 0.1 g/cm³ the refractive index is constant. If a fixed density (0.1 g/cm³) for all snow particles (size up to 1 cm) is considered using the same SWP and LWP, the TB enhancement is up to 8 K higher than the corresponding value calculated with the *Matrosov* model.

To further verify the effects of mass size relationship (i.e., snow particle density and snow refractive index) on PD and TB, monodispersed snow particles with horizontal orientation

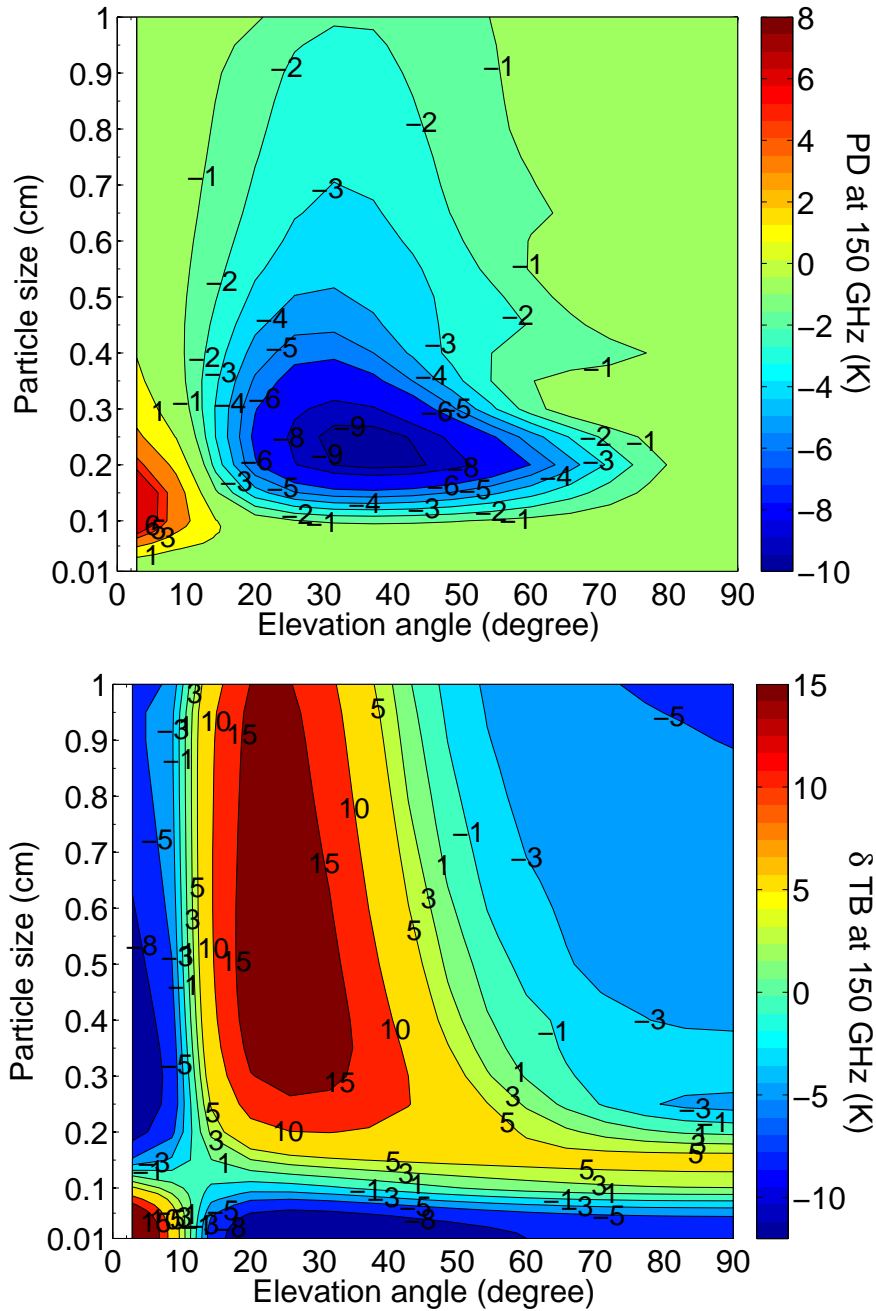


Figure 5.10: Same as Figure 5.9, except that the snow particles are supposed to have a fixed density of 0.1 g/cm^3 .

by the Matrosov model is only $\sim -5 \text{ K}$ (Figure 5.9, top panel) even though the number of monodispersed snow particles in Matrosov relation is higher to arrive the same SWP value. For the Matrosov mass size relationship, the decrease of snow particle density results in a lower refractive index and it further causes a reduced scattering effect (Figure 5.9, bottom panel). Especially for particle sizes larger than 0.6 cm , PD is only $\sim -1 \text{ K}$ since large Matrosov particles have a low refractive index. This could be one of the reasons why large particles induce a much lower PD than smaller particles (Figure 5.9, bottom panel), when comparing to particles with a fixed density.

Another feature of PDs, which needs to be pointed out, is the so-called “resonance” feature (*Evans and Stephens, 1995b; Miao et al., 2003; Xie and Miao, 2011*), as shown in Figure 5.9 and Figure 5.10. This feature is associated with particle scattering characteristics. It seems that PD at a specific frequency is mainly sensitive to snow particles with a certain size. At 150 GHz, the resonance peak position of PD is shown only at the particle size ranging from 0.2 cm to 0.3 cm (hereinafter called resonance size). PD increases with particle size if its size is less than the resonance size. Whereas, the dichroism effect due to oriented particles is weaker when the particles become larger than the resonance particle size, even for particles with a fixed density and refractive index (Figure 5.10, top panel).

Mass size relation reveals prominent effects on TB. TB is strongly enhanced by oriented snow particles (Figure 5.9 and Figure 5.10, bottom panels). When a higher particle density is assumed, TB becomes larger. δ TB due to the constant particle density is up to more than 15 K when comparing to the “standard TB” (Figure 5.10, bottom panel), while the maximum δ TB by Matrosov monodispersed particle is only about 5 K (Figure 5.9, bottom panel). It is noticed that the TB enhancement is limited for large particles. Even when a fixed particle density of 0.1 g/cm³ is assumed (Figure 5.10, bottom panel), δ TB remains the same even for particle size up to 1 cm. This is because the extinction effects due to snow particles tend to be constant when their sizes are much larger than the wavelength.

5.2.4 Other parameters

Supercooled liquid water is frequently observed during snowfall. A source of uncertainties is its optical properties which depends on the refractive index. However, the poor knowledge of the liquid refractive index make it difficult to accurately derive its effects on RT simulations, because of rare laboratory measurements especially at low temperatures. A difference in TB which is caused by varying liquid refractive index models is on the order of 10 (*Ellison, 2006; Stogryn et al., 1995*). Considering the small water droplets assumed in this study, the most important impact of supercooled water on TBs is the strong emission, which greatly depends on the imaginary part of the supercooled water refractive index. The extinction cross section due to the strong absorption of the water droplets gradually increases with temperature, and the difference between the two models can be more than 30%, especially when the temperature is low than 250 K (Figure 5.11). At the temperature of 244 K, the corresponding emission resulting from *Stogryn et al. (1995)* is $\sim 30\%$ lower than the value of *Ellison (2006)*, because of the $\sim 10\%$ lower imaginary part of refractive index; therefore, the supercooled water emission by *Ellison (2006)* results in lower TBs on the order of 10 K (*Redl, 2011*). It reveals that the enormous influence of uncertainties in the different refractive index models for supercooled liquid water may result in significant deviations of SWP and LWP retrievals.

The surface radiation is one of the main sources that enhance the radiance observed by the ground-based instruments. One source of uncertainty is the surface emissivity which varies with frequency and snow type (*Harlow, 2007*). For ground observations, it is found to be comparably low: decreasing from 0.9 to 0.7 results in only ~ 1.62 K lower TB and 0.8 K lower PD. The influence of surface emissivity is very limited at 150 GHz (*Kneifel et al., 2010*).

Another important uncertainty could come from the exponential size distribution. *Field et al. (2005)* is used for the sensitivity study shown above. A decrease in the intercept parameter from 10^7 m⁻⁴ to 10^6 m⁻⁴ increases the mean particle size, which has important effects on the PDs and TBs. At 32° elevation angle, the PD and TB are only influenced minimally (less

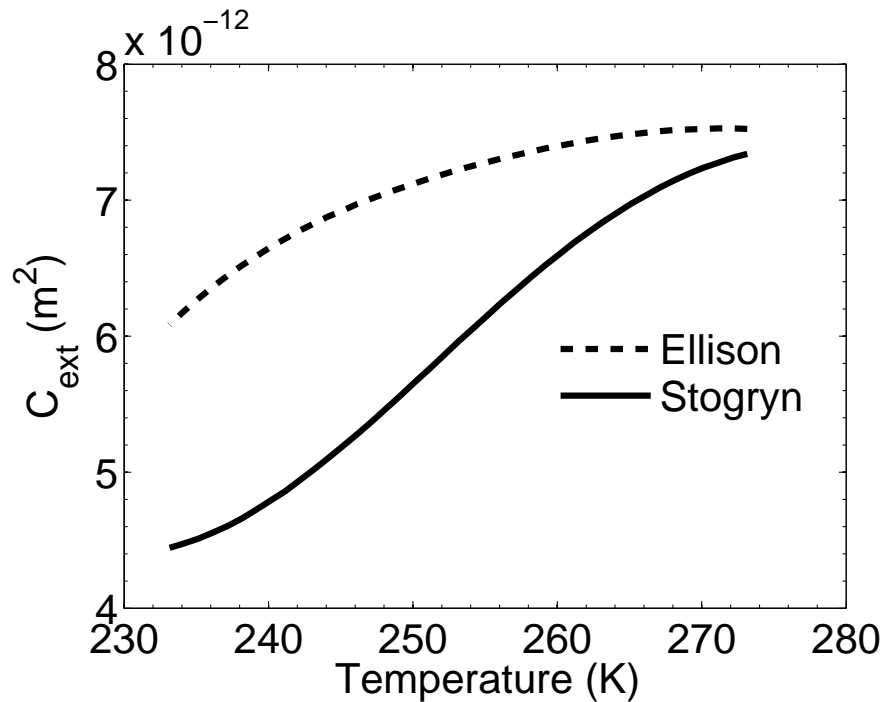


Figure 5.11: Extinction cross section C_{ext} for a single particle at 150 GHz. The radius of supercooled water droplet is assumed to be $10 \mu\text{m}$. Refractive index of supercooled liquid is calculated by *Stogryn et al.* (1995) and *Ellison* (2006).

than 1 K) by the variation of the intercept parameter; however, at other elevation angles (40° - 80° elevation angle), the effects can range up to 5 K in TB and 1 K in PD, assuming the Matrosov mass size relationship.

5.3 Explanations of supercooled liquid water effects on PD and TB

Supercooled liquid water is frequently present during snowfall. It damps PD but strongly enhances TB, as shown in Figure 4.1 and Figure 5.1. To figure out how supercooled liquid water affects PD and TB, RT simulations are performed. Section 5.3.1 introduces a simple physical model to better explain the effects of the absence/existence of supercooled liquid water on PD and TB. A further discussion in Section 5.3.2 analyzes the effects of cloud liquid emission on PD and TB, assuming that cloud liquid water is located at different altitudes with respect to the snow layer.

5.3.1 With or without supercooled liquid water

Generally, in the presence of precipitation and clouds which consist of horizontally-oriented particles, the predominant radiance observed from a ground-based perspective is horizontally polarized, i.e., the intensity at the horizontal polarization is greater than the corresponding value at the vertical polarization (*Czekala et al.*, 2001b; *Troitsky et al.*, 2003; *Battaglia et al.*,

2009). The different extinction/scattering/absorption cross sections at the horizontal and vertical polarizations due to the dichroic medium cause that the received radiation has a preferential polarization. More horizontally polarized intensity is scattered towards the ground surface and more vertically polarized radiance penetrates the dichroic medium. Only at low elevation angles, PD tends to be positive when observed from ground (e.g. *Czekala and Simmer, 1998; Troitsky et al., 2003*).

With the existence of supercooled liquid water, TBs are strongly enhanced due to the absorption/emission processes of supercooled liquid water, while PDs are damped. To better interpret the “damping” effects of supercooled liquid water on PDs, a simplified model is employed in this section (*Miao et al., 2003*). In the simple physical model, the plane-parallel atmosphere is divided into three layers (Figure 5.12). The reflection and refraction effects at the layer boundaries are neglected.

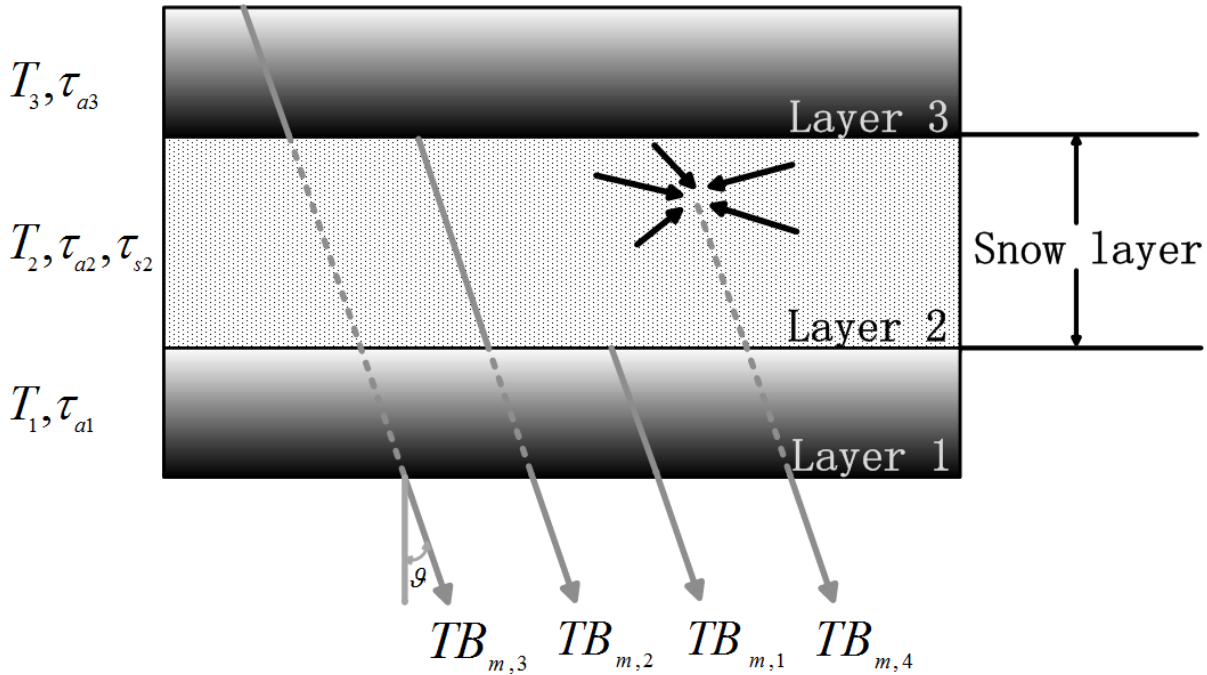


Figure 5.12: Sketch of the three-layer physical model. (From *Miao et al., 2003*)

The snow layer is composed of horizontally-oriented particles and it is located in the middle layer in the simple model (Figure 5.12, Layer 2). The snow layer can be characterized by its absorption and scattering optical depths, τ_a and τ_s . For the snow layer composed of preferentially aligned non-spherical particles, scattering coefficients are different for vertical and horizontal polarizations, so that it enhances one component respect to the other. The absorption effect by the snow layer is usually minimal since it is much weaker than the scattering effect. The other two layers in the model are a non-dichroic but absorbing medium which could be composed of liquid water or gaseous molecules (Figure 5.12, Layer 1 and Layer 3). The radiation attenuation in the two absorbing layers is mainly attributed to their absorption effects, while the scattering effects in these two layers can be neglected.

The total TB received from the ground-based perspective is denoted by TB_m . The subscript m indicates the polarization status of the radiation, v or h, for vertical or horizontal polarization, respectively. The received radiation TB_m has contributions from four components: (a) the emission of Layer 1 with a temperature T_1 and an optical depth τ_{a1} $TB_{m,1}$, (b) the

emission of the snow layer attenuated by the non-dichroic absorbing Layer 1 (its emission can be usually negligible) $TB_{m,2}$, (c) the emission of the non-dichroic Layer 3 attenuated by Layer 2 (its absorption and scattering processes) and Layer 1 (its absorption effect) $TB_{m,3}$, and (d) the contribution from the snow layer scattering which is then attenuated by Layer 1 $TB_{m,4}$. Therefore, TB_m is expressed as the summation of the four different components.

$$TB_m = TB_{m,1} + TB_{m,2} + TB_{m,3} + TB_{m,4} \quad (5.5)$$

The four terms at the right side of Equation 5.5 then are written as,

$$\begin{aligned} TB_{m,1} &= T_1(1 - e^{-\tau_{a1} \sec \vartheta}) \\ TB_{m,2} &= T_2(1 - e^{-\tau_{a2} \sec \vartheta})e^{-\tau_{a1} \sec \vartheta} \\ TB_{m,3} &= T_3(1 - e^{-\tau_{a3} \sec \vartheta})e^{-(\tau_{a1} + \tau_{a2} + \tau_{m,s2}) \sec \vartheta} \\ TB_{m,4} &= T_{m,s}e^{-\tau_{a1} \sec \vartheta} \end{aligned} \quad (5.6)$$

where ϑ is the zenith angle, τ_a is the optical depth due to the absorption of the atmosphere, τ_{s2} specifies the attenuation caused by scattering effect of the snow layer, and $T_{m,s}$ is the scattered brightness temperature at the m polarization in the snow layer.

The absorption optical depths are enhanced by the presence of the strongly absorbing medium (i.e., Layer 1 and Layer 3) in the atmosphere. It can be easily derived by combining Equation 5.5 with Equation 5.6 that TB_m is augmented by the emission processes of Layer 1 and Layer 3. Assuming that supercooled liquid water occurs during snow events, no matter where the supercooled liquid water is located (Layer 1 or Layer 2 or Layer 3), the TB_m is strongly enhanced by the emission of supercooled liquid water. The stronger the liquid water emission, the stronger the received TB from ground.

The induced polarization difference PD can be derived from Equation 5.5 combined with Equation 5.6, and it is given as follows,

$$\begin{aligned} PD &= TB_v - TB_h \\ &= \underbrace{T_3(1 - e^{-\tau_{a3} \sec \vartheta})e^{-(\tau_{a1} + \tau_{a2}) \sec \vartheta} (e^{-\tau_{v,s2} \sec \vartheta} - e^{-\tau_{h,s2} \sec \vartheta})}_{\text{the first term}} \\ &\quad + \underbrace{(T_{v,s} - T_{h,s})e^{-\tau_{a1} \sec \vartheta}}_{\text{the second term}} \end{aligned} \quad (5.7)$$

To derive the PD expressed in Equation 5.7, the first two terms given in Equation 5.5 are canceled, and only the last two terms matter since the radiation interacts with the dichroic medium in Layer 2.

In Layer 2, the scattering optical depths at the horizontal and vertical polarizations, $\tau_{h,s2}$ and $\tau_{v,s2}$, are different since the snow layer is dichroic. If it contains only spherical particles in Layer 2, the first term at the right side of Equation 5.7 is supposed to be zero. For the horizontally-oriented particles, $\tau_{v,s2}$ is less than $\tau_{h,s2}$ for upward viewing observations (*Battaglia et al., 2006; Battaglia and Simmer, 2007*). This is also verified by the extinction matrix element K_{12} which is negative for horizontally aligned oblates. Thus, the sign of the first term in Equation 5.7 is positive. The second term at the right side of Equation 5.7 is attributed to the scattering effects of the snow layer. It is generally non-zero and its value depends on the radiation from all directions in this layer (*Miao et al., 2003*).

The contribution from the atmosphere at lower levels plays an unneglected role in the ground based observations. The ground surface and the medium below the snow layer can be regarded

as one layer within the Layer 1, when additional radiation comes from the surface. The magnitude of the scattered brightness temperature $T_{m,s}$ is mainly associated with the snow particle scattering in Layer 2 and the upwelling TB from the layers below (Layer 1 and the surface emission). The downwelling radiation from Layer 3, which is scattered by Layer 2, could also affect $T_{m,s}$. However, this effect is much smaller since (a) the scattered radiation in the forward direction is usually much stronger, especially for particles with large size parameter (e.g., *Liu*, 2008), and (b) the attenuation by the snow scattering at the upper part of Layer 2 reduces the effects of the downwelling radiances from Layer 3, especially when the snow layer is thick enough. In the incoming scattering direction at the zenith angle of ϑ' , the upwelling radiance T'_s , which contributes to the scattered $T_{m,s}$ in Layer 2, can be expressed by

$$\begin{aligned} T'_s &= T_1(1 - e^{-\tau_{a1} \sec \vartheta'}) + \varepsilon T_{surf} e^{-\tau_{a1} \sec \vartheta'} \\ &\quad + T_2(1 - e^{-\tau_{a2} \sec \vartheta'}) \end{aligned} \quad (5.8)$$

where T_{surf} is the temperature of the ground surface with an emissivity of ε . Both the emissions from the surface and Layer 1 are non-dichroic, while the emission from Layer 2 is negligible.

For simplification, we assume that the ground surface temperature is equal to the temperature of Layer 1, and the surface emissivity is equal to 1. Thus, T'_s is only a function of T_1 , T_2 and the scattering properties of Layer 2 (Equation 5.8). The scattering radiance $T_{m,4}$ is mainly dependent on the temperatures of Layer 1 and Layer 2 and the snow dichroic effects. According to the RT simulations described in Section 5.1, $T_{h,s2}$ in Layer 2 is larger than $T_{v,s2}$ in absence of liquid water, due to the scattering characteristics of horizontally aligned snow particles. Thereby, PD is negative for the ground based observations when supercooled liquid water is absent.

If Layer 1 and Layer 3 are non-absorbing (Figure 5.12), i.e., τ_{a1} and τ_{a3} are zero, the received PD is denoted by PD^{null} . Thus, PD^{null} is only a function of its scattered TB expressing by $T_{m,s}^{null}$ in Layer 2 (Equation 5.9). When only Layer 1 is absorbing with an optical depth τ_{a1} , the induced $PD^{\tau_{a1}}$ is reduced to be only caused by the second term in Equation 5.7, and the value is attenuated by the absorption of Layer 1 (Equation 5.10). Assuming that Layer 1 is non-absorbing while Layer 3 is an absorbing medium, the first term in Equation 5.7 occurs with the absorption optical depth τ_{a3} in Layer 3. This term allows more vertical radiation penetrating through the dichroic medium. When the radiance propagates in the dichroic medium Layer 2, in this case (horizontally oriented particles) $\tau_{h,s2}$ is larger than $\tau_{v,s2}$.

$$PD^{null} = T_{v,s}^{null} - T_{h,s}^{null} \quad (5.9)$$

$$PD^{\tau_{a1}} = (T_{v,s}^{\tau_{a1}} - T_{h,s}^{\tau_{a1}}) e^{-\tau_{a1} \sec \vartheta} \quad (5.10)$$

$$\begin{aligned} PD^{\tau_{a3}} &= T_3(1 - e^{-\tau_{a3} \sec \vartheta}) e^{-\tau_{a2} \sec \vartheta} (e^{-\tau_{v,s2} \sec \vartheta} - e^{-\tau_{h,s2} \sec \vartheta}) \\ &\quad + (T_{v,s}^{\tau_{a3}} - T_{h,s}^{\tau_{a3}}) \end{aligned} \quad (5.11)$$

The three scattering related TBs are very approximate, $T_{m,s}^{null} \approx T_{m,s}^{\tau_{a1}} \approx T_{m,s}^{\tau_{a3}}$, according to Equation 5.8. The PD^{null} is negative if observed from ground. Therefore, compared with the three PD values expressed in Equations 5.9 – 5.11, the PD^{null} value is larger than $PD^{\tau_{a1}}$ since $PD^{\tau_{a1}}$ is attenuated by the absorption of Layer 1. The PD^{null} value is also larger than $PD^{\tau_{a3}}$. This is because $\tau_{h,s2}$ is larger than $\tau_{v,s2}$ in the layer and more vertical radiation from the layer above snow penetrates the dichroic snow layer. Thus, the emission from Layer 3 narrows down polarization signals caused by the snow scattering effects.

Therefore, the effects of supercooled liquid water on TB and PD can be explained as follows.

- (a) When supercooled liquid water is located at an altitude lower than the snow layers, the absorption effect of cloud liquid water damps PD while its emission greatly enhances the TB.
- (b) When the supercooled liquid water is located at a higher altitude, PD mainly originates from two components. One component is the cloud liquid emission attenuated by snow extinction, and the other component is caused by the scattering effects of the snow layer. The first component compensates the snow scattered PD and narrows down the difference between the two orthogonal polarizations.
- (c) If the supercooled water is distributed in the snow layer (either homogeneously or heterogeneously), partial of the PD caused by the snow scattering is absorbed by supercooled liquid water and partial of the PD is compensated by the radiance which is emitted by the non-dichroic layer and scattered by the dichroic layer.

The magnitude of the induced PD depends on the predominant process in the atmosphere: it can be the scattering in the snow layer or the absorption in the layer below or the compensation effect from the layer above.

In general, PD is damped by the supercooled liquid water during snowfall. Assuming that supercooled liquid water is located at different height with respect to the dichroic snow layer, RT simulations are performed in the following section to quantify the effects of liquid water emission on PD and TB.

5.3.2 Locations of supercooled liquid water

One of the highest uncertainties in RT simulations is the radiative properties of the supercooled liquid water. Not only the total amount but also the specific vertical distribution of supercooled liquid water affect the measured TBs and PDs due to the different propagation paths and the radiative interactions between cloud liquid and snow particles. It was reported that supercooled liquid water tends to concentrate at the top of ice clouds (*Rauber and Tokay, 1991; Fleishauer et al., 2002*). However, the vertical distributions of supercooled liquid water, as well as the dependence of cloud liquid water emission on atmospheric temperatures, is still not clear.

To examine the sensitivity of PD and TB to the emission of supercooled liquid water, the top of liquid water layer is assumed to vary from 500 m to 5000 m (AGL). The supercooled liquid water is distributed homogeneously within 500 m with a LWP of 100 g/m². Four different scenarios are considered in the following simulations.

Scenario 1: The temperature profile with a constant value of 260 K reaches up to 10 km. A snow layer is located between 1000 m and 3000 m (AGL), and the SWC is 0.5 g/m³. The atmospheric pressure is interpolated from the standard atmosphere, and expressed as a function of altitude. In order to examine the effects from supercooled liquid water emission, no water vapor is assumed in the atmosphere.

Scenario 2: The air temperature close to the ground is 265 K. A snow layer with a SWC of 0.5 g/m³ is located between 1000 m and 3000 m (AGL), and has a constant temperature

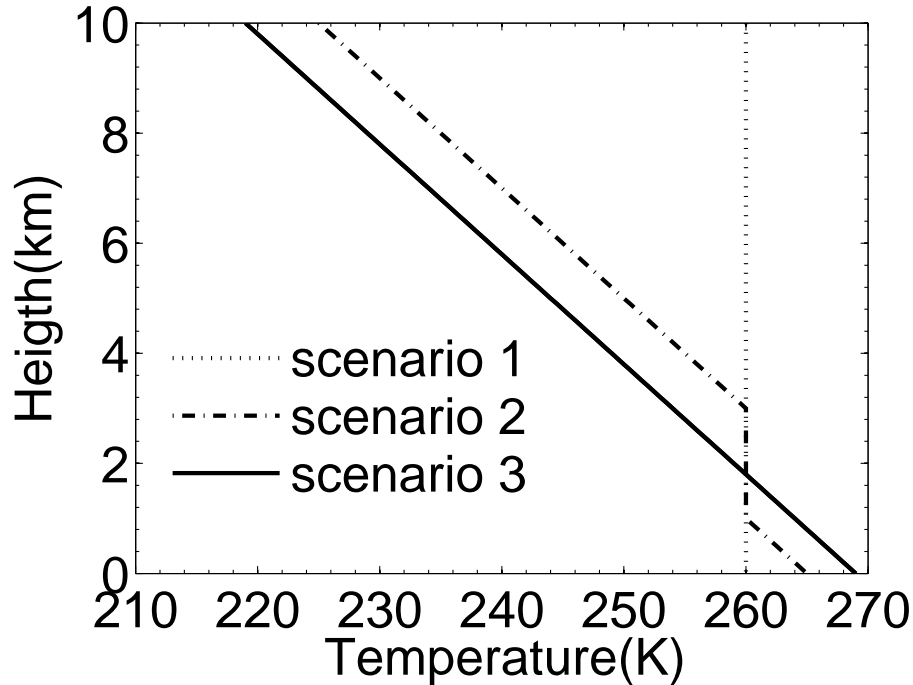


Figure 5.13: Temperature profiles for all the scenarios. Note that, the temperature profile in Scenario 4 is the same as in Scenario 3.

of 260 K. Above and below the snow layer, the temperature lapse rate is -5 K/km. Atmospheric pressure varies with altitude. No water vapor absorption is considered in this scenario.

Scenario 3: The temperature varies with altitude, with a lapse rate of -5 K/km. A snow layer with a SWC of 0.5 g/m³ is assumed to be at an altitude between 1000 m and 3000 m (AGL). Absorption due to water vapor is not considered.

Scenario 4: Same as Scenario 3 except that the absorption of water vapor is included in Scenario 4.

The atmospheric temperature profiles are shown in Figure 5.13. Pressure profiles in the four scenarios are all the same and interpolated as a function of height. The water vapor profile in Scenario 4 is interpolated based on the midlatitude standard atmosphere in winter time. The surface is assumed to be Lambertian with an emissivity of 0.9 and the radiance emitted by the ground surface is unpolarized. The temperature of the ground surface is equal to the temperature of the lowest atmosphere.

Snow particles are assumed to be in exponential distribution (Section 5.1.1), and they are supposed to be horizontally-oriented oblates with an aspect ratio of 0.5. The Matrosov model (Matrosov, 2007) is used to model the mass size relationship of snow particles. Single scattering properties of the snow layer and liquid clouds are calculated by the T-matrix method (Mishchenko, 2000). Supercooled liquid water is supposed to consist of monodispersed spherical water droplets with a radius of 10 μ m. Thus, the dichroism effect originating from liquid water layers can be neglected. The channel frequency considered here is 150 GHz.

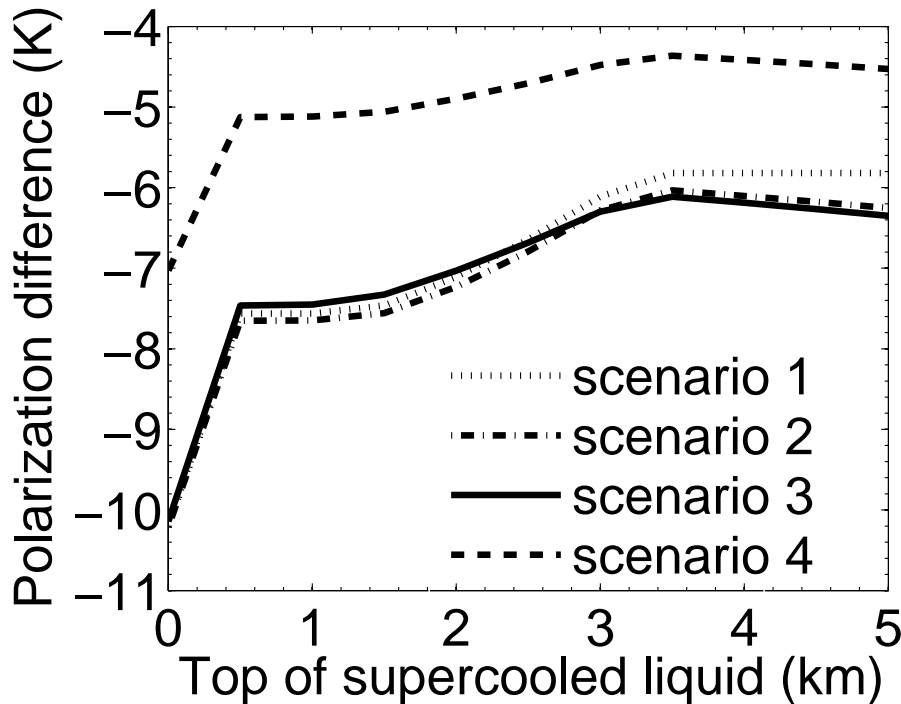


Figure 5.14: PD as a function of top of supercooled liquid water at an elevation angle of 32° . Temperature profiles for the four scenarios are shown in Figure 5.13. Note that no liquid water is present in RT simulations when the top of supercooled liquid = 0 km.

Note that the scattering effect plays a major role in the extinction process at this frequency for the snow layer, while the emission/absorption dominates the extinction process of liquid water clouds. The extinction of supercooled liquid water depends on its temperature and the lower temperature results in less extinction, according to the refractive index model of liquid water at 150 GHz from *Ellison* (2006) (Figure 5.11).

PD and TB are shown as a function of liquid cloud top in Figure 5.14 and Figure 5.15, respectively. Liquid cloud top equal to zero specifies that LWP is assumed to be zero in RT simulations. PD is strongly damped by supercooled liquid water in the snow event, compared to the absence of cloud liquid water (liquid top=0 km, Figure 5.14). The absorption of supercooled liquid water results in ~ 2.5 K decrease of PD for the four scenarios. When cloud liquid water begins to ascend, i.e., its top increases from 500 m to 5000 m (AGL), the variation of PD is up to 2 K.

For Scenario 1 (Figure 5.14, the dotted line), when the height of liquid cloud top is still lower than the snow layer (from 500 m to 1000 m AGL), PD remains the same with an increase of liquid cloud top height. The constant PD is caused by the weak gaseous absorption (no water vapor) and the constant atmospheric temperature profile. As cloud liquid water begins to enter the snow layer (from 1000 m to 3000 m AGL), the PD value decreases gradually (Figure 5.14, the dotted line), since PD is partially absorbed (supercooled liquid water below snow) and the difference between the two orthogonal polarizations is partially narrowed down by the liquid water emission propagating through the snow layer (supercooled liquid water above snow). The radiation at the vertical polarization which is emitted from the liquid water above snow compensates PD significantly and reduced the PD value. This compensation effect

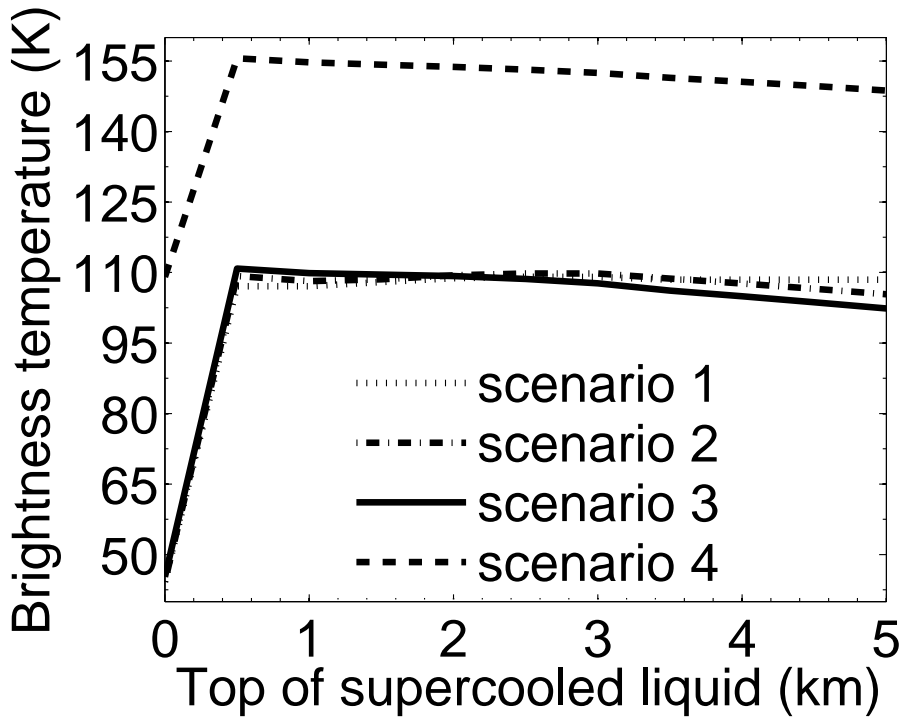


Figure 5.15: Same as Figure 5.14 except for TB

makes PD decrease with the increasing liquid top height. When cloud liquid top is located above the snow layer, PD remains constant even though its top ascends from 3500 m to 5000 m (AGL). This is explained by the constant atmospheric temperature which results in the constant emission of supercooled liquid water.

Scenarios 2 – 4 have a similar PD behavior with Scenario 1 (Figure 5.14). The presence of supercooled liquid water damps the PD value. For Scenarios 2 – 4, when the supercooled liquid water is below the snow layers (500 m to 1000 m AGL), the absorption effects of liquid water reduce the PD values. The stronger the liquid water absorption, the smaller the PD. When the supercooled liquid water is higher than 3000 m in Scenarios 2 – 4, the PD value gradually increases with cloud liquid top height since the emission of supercooled liquid water in these scenarios is reduced by the decreasing temperature, and the “compensation” effects on PD are weakened accordingly. Compared Scenario 2 to Scenario 3, PD in Scenario 2 is lower for the stronger emission from cloud liquid above snow. This can be explained by the “fading” effects from the emission of supercooled liquid water. If the temperature gradually decreases with increasing height, PD is more close to the corresponding value calculated without supercooled liquid water, i.e., at liquid top = 0.

To examine the absorption effects of water vapor, PD in Scenario 4 is compared with the corresponding value in Scenario 3 (Figure 5.14, the solid and slashed lines). It can be seen clearly that the additional absorption by water vapor in the atmosphere can also greatly affect PD, according to PD values in Scenario 4 which are much less than the corresponding values in Scenario 3.

The presence of supercooled liquid water enhances the received TB for upward viewing instruments, on the order of 50 K (Figure 5.15). This is in agreement with observations described in Chapter 4. The temperature dependence of liquid water emission is the main reason that

induces the variation of the TB. Changing the cloud liquid top causes a change of TB up to 5 K. When the height of liquid water increases, the decreasing temperature results in lower liquid water emission and further reduces the received TB (Scenario 2 and Scenario 3 in Figure 5.15), since the dominant process in TB is the emission of supercooled liquid water. The stronger the emission of supercooled liquid water, the stronger the enhanced TB. TB in Scenario 2 is lower than TB in Scenario 3 when cloud liquid top is at a lower altitude since the atmospheric temperature is lower in Scenario 2 (Figure 5.15). It is noted that the existence of water vapor strongly enhances TB due to its strong absorption/emission effects, compared Scenario 3 to Scenario 4. Note that TB is the averaged TB between the vertical and horizontal polarizations.

5.4 Conclusions and remaining uncertainties

To better interpret the polarization observations during snowfall, a single snow case was analyzed in this chapter. The effects of SWP and LWP on PD and TB were examined by means of RT simulations. The RT results verified the effects of SWP and LWP: SWP enhances PD and TB while LWP enhances TB but damps PD.

To further investigate the potential of PD for snowfall retrievals, the sensitivities of PD and TB to snow parameters, such as aspect ratio, mass size relation, orientation, etc., were evaluated by the RT simulations. Changing snow particle aspect ratio can induce the variation of PD and TB up to 7 K. Uncertainties of snow parameters in the RT simulations also come from the representation of particle preferential orientation and mass size relations. Compared to randomly oriented particles, snow particles with preferential orientation enhance their scattering effects and cause larger PD and TB. Denser snow particles induce stronger dichroism and scattering effects, and result in TB and PD enhancement. One of the most prominent uncertainties for RT simulations is caused by the temperature dependent emission of supercooled liquid water during snowfall. The different refractive index models of liquid water could induce a TB difference on the order of 10 K. In the presence of supercooled liquid water, TB is enhanced while PD is damped. The damping effects due to supercooled water are different: (a) if the supercooled liquid water is located at the top of the snow layer, the penetrated vertical radiance from liquid emission compensates partly the PD scattered by the dichroism medium; (b) while the absorption of the liquid water below the snow layer results in a damped PD. The RT simulated PD and TB which depend on the liquid water emission vary up to several Kelvins, when the location of supercooled liquid water changes with respect to the height of the snow layer.

The observed PD and TB are well captured by the assumptions on snow parameters for the single snow case. However, the discrepancies between the observations and RT simulations still remain (Figure 5.16), which could be explained by considering (a) uncertainties in snow microphysical assumptions in RT models and (b) the different observation geometries. While the latter can be improved by synchronous observations in future, the uncertainties in snow microphysical assumptions affect significantly the accuracy of retrievals. All these microphysical properties have non-negligible effects on PD and TB (Section 5.2). However, only soft oblates with a fixed AR are considered in this chapter. Real snow particle habits and sizes can be far more complicated. The simplified particle geometry causes a significant uncertainty in the RT simulations and results in discrepancies between the observations and RT simulations. Another uncertainty resulting from the homogeneously mixed snow particle assumption, e.g., using the Maxwell-Garnett dielectric mixing formula, underestimates snow

particle scattering. Thus, the assumption of mixed snow particles reduces PD and TB in the RT simulations accordingly, compared to complex ice and air geometry (e.g., by the DDA algorithm). Scattering properties of snow particle characterized by more “realistic” geometry need to be taken into account, to avoid uncertainties caused by particle habits. Moreover, the realistic representation of snow particle orientation which has large impact in the RT simulations, especially on PD, can improve the accuracy of snowfall retrievals.

Furthermore, RT simulations in this study were carried out by assuming a one-dimensional plane-parallel model. However, three dimensional effects will become significant, especially when higher frequencies are taken into account. It is necessary to consider cloud inhomogeneity at the observation sites where clouds vary temporally and spatially. Thus, a three dimensional fully polarized radiative transfer model needs to be employed in future studies.

5.5 Implications of PD for snowfall retrievals

For most snow cases at UFS, the presence of supercooled liquid water is quite frequent with a median value on the order of $\sim 100 \text{ g/m}^2$ (Löhnert *et al.*, 2011). Therefore, the contributions of TB signals observed by ground-based microwave radiometers are mainly from the mixture of supercooled liquid water emission and snow scattering. To characterize snowfall parameters, it is significant for passive microwave radiometry to distinguish snow scattering from liquid water emission. Passive microwave radiometry is a suitable and effective method for the retrievals of integrated cloud liquid water amounts (Löhnert and Crewell, 2003). At HATPRO channel frequencies (22 – 31 GHz), TB is much sensitive to liquid water emission rather than snow scattering (Figure 2.4). The snow scattering, which plays an important role at higher frequencies, can be ignored at low microwave frequencies (22 – 31 GHz), while the absorption of supercooled liquid water is important in the whole microwave spectrum. However, the information on the liquid water profile cannot be obtained from passive microwave observations (Crewell *et al.*, 2009) and only the integrated liquid water information can be derived on the basis of the low frequency channels. Unfortunately, the temperature dependence of supercooled liquid water emission, which affects the received PD and TB signals at high microwave frequencies, makes the distinction of snow scattering signals from supercooled liquid water emission quite necessary.

The effects of liquid water emission and snow scattering on TB signals can be overlapped when only TBs are used in the retrievals of snow parameters, even though the observations at 90 GHz and 150 GHz are combined (Figure 4.5). It is possible to retrieve snow microphysics with the combination of PD and TB which is proposed as the snowfall retrieval algorithm (Figure 4.3 and Figure 5.1). The corresponding SWP and LWP can be directly retrieved by the observed PD and TB, by means of the proposed algorithm. Therefore, the impacts of supercooled liquid water and snow on PD and TB can be distinguished from each other.

However, the accuracy of the snowfall retrieval algorithm highly depends on the atmospheric conditions input in the RT model. A reasonable assumption on the snowfall parameters is necessary since the PD and TB in the RT simulations are highly correlated to the snow microphysics (Section 5.2). Another important factor which affects the accuracy is the accurate representation of supercooled liquid water in the proposed retrieval algorithm. The TB and PD values, which derive snow parameters from the proposed PD/TB combination retrieval algorithm, vary with the locations of supercooled liquid water. As shown in Figure 5.16, the slashed gray and solid black contour lines are calculated with supercooled liquid water at the

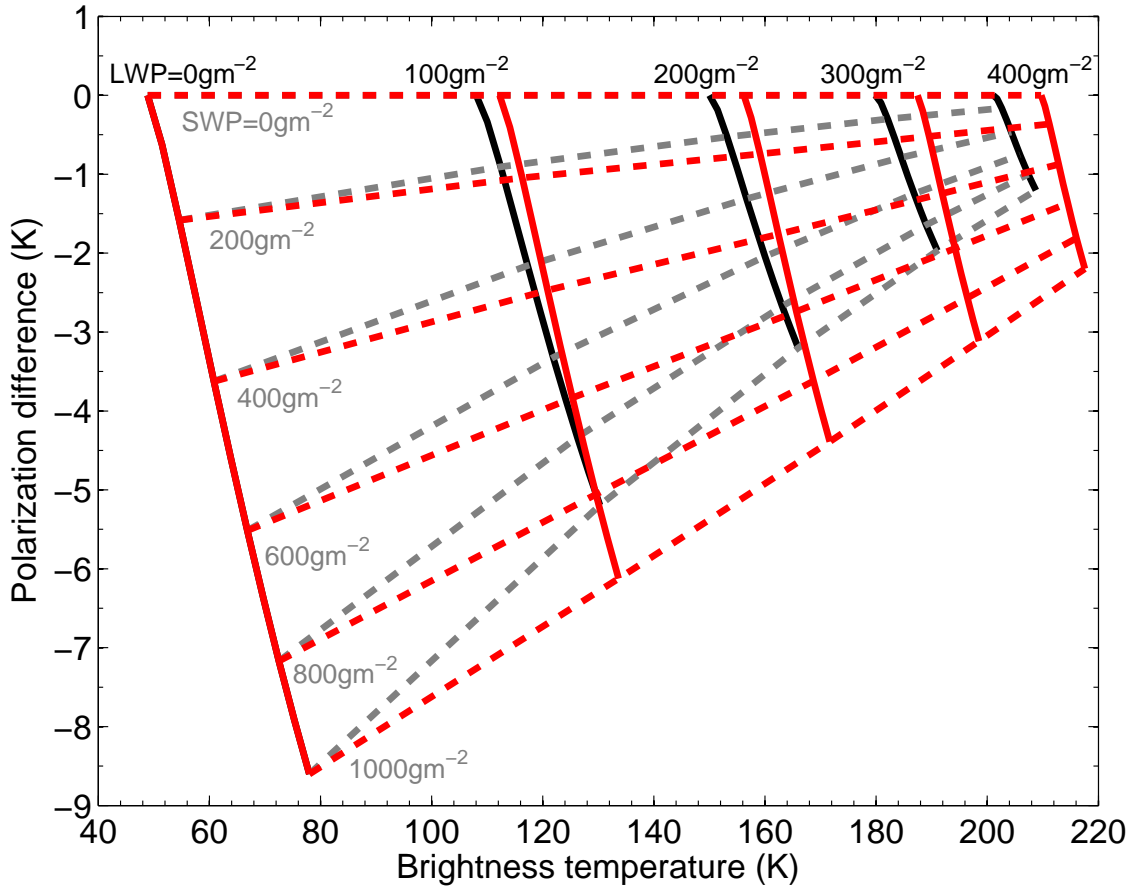


Figure 5.16: RT simulation results (For details see Figure 5.1). The solid black lines are the contours of LWP ranging from 0 to 400 g/m^2 and the dashed gray lines are the contours of SWP ranging from 0 to 1000 g/m^2 (0 m – 2000 m AGL), assuming that supercooled liquid water is located above snow layers (2000 m – 2500 m AGL). The solid red lines are the contours of LWP and the dashed red lines are the contours of SWP when the cloud liquid water is distributed homogeneously in the snow layer, from 0 to 500 m (AGL). Changing the height of supercooled liquid water, from the top of snow layer to bottom, results in PD and TB shifts since supercooled liquid water emission varies with its height.

top of snow layer, i.e., 2000 m – 2500 m (AGL), while the red solid and dashed lines are for cloud liquid touching down the ground surface, i.e., 0 – 500 m (AGL). When the liquid cloud ascends, the emission of supercooled liquid water decreases due to the decreasing atmospheric temperature with height. The more the cloud liquid (snow) amounts, the stronger the absorption (scattering) effects on PD and TB. According to the different effects of the location of supercooled liquid water with respect to snow layer (Section 5.3), the warmer the cloud liquid, the stronger the TB enhanced, while the emission of liquid water damps PD. The uncertainties in supercooled liquid water emission results in a deviation of the retrieved SWP, up to 200 g/m^2 , as shown in Figure 5.16. If the vertical structure of liquid water information can be provided by other techniques, the accuracy of snowfall retrievals can be greatly improved by the constraints from the liquid water information.

PD information promotes the new instrument design for remote sensing of frozen hydrometeors. A dual polarized microwave radiometer with a high accuracy is needed in order to

observe PD signals caused by preferentially oriented snow particles, especially at the observation sites where the strong absorption of gas and liquid water can strongly attenuate PD. Whether polarization sensors will be boarded on space-borne satellites or not significantly depends on the information content provided by polarizations. In the following chapter, the polarization observation from space will be discussed to investigate its benefits for ice cloud characterization.

Chapter 6

Potential of PD information for ice cloud detection

Polarization measurements have been proposed as an efficient method of cloud observation improvement in the past decade (*Prigent et al.*, 2001; *Miao et al.*, 2003; *Davis et al.*, 2005; *Prigent et al.*, 2005). A new generation of the geostationary meteorological satellite FY-4 in China, which is now in pre-research phase, is planned to provide polarization information for ice cloud observations. It is proposed to be equipped with three dual polarized window channels at microwave band, i.e., 150 GHz, 220 GHz and 340 GHz. In this chapter, the sensitivities of PD and TB to the ice particles with preferential orientation are analyzed at the three FY-4 channels, in order to exploit the potential role of polarized signature in characterizing ice clouds in the microwave spectrum.

6.1 FY-4 description

The FY-4 satellite is the second-generation geosynchronous meteorological satellite in China. It intends for meteorological and hydrological observations and its observations will cover the territory of China with a scan period of ~ 15 min. The data observed by the FY-4 satellite can continuously provide high temporal-resolution observations. It can improve the quality of weather analysis and forecasting, atmospheric sounding of temperature and humidity, and the reliability of severe weather system monitoring.

FY-4 is proposed to carry an optical sensor and a microwave sensor aboard. FY-4 will operate in the geostationary orbit ($\sim 36\,000$ km MSL) and thus its spacial resolution will be much lower than the polar orbiting satellites (normally less than 1000 km MSL). The selected frequencies for the microwave sensor range from 50 GHz to 400 GHz. Besides the established observation purposes of the FY-4 satellite, another potential application of the microwave sensor aboard is to observe ice clouds at high altitudes by the window frequency channels which are less affected by the gaseous absorption.

The knowledge of ice clouds is still limited and becomes one of the major uncertainties in weather and climate studies. The challenge for the detection of ice clouds is their high altitudes as well as complex and variable structures. Previous observations showed that considerable crystals in cirrus clouds have preferred orientations due to aerodynamic forces (e.g., *Chepfer et al.*, 1999; *Noel and Chepfer*, 2004; *Noel and Sassen*, 2005). Of all ice cloud

layers, $\sim 6\%$ are found to be characterized by oriented crystals, based on the global analysis of CALIPSO observations (*Noel and Chepfer, 2010*). Non-randomly oriented particles result in a difference between horizontal and vertical polarizations, which has been detected in cloud systems in the previous studies (*Prigent et al., 2001; Troitsky et al., 2003; Prigent et al., 2005; Davis et al., 2005*).

Using high channel frequencies to characterize ice clouds is proposed as a new technique which has been developed for ice cloud retrievals in the past decades (e.g., *Evans and Evans, 1999; Evans et al., 2002; Evans, 2004; Buehler et al., 2007*). To better characterize ice clouds, so far three dual polarized window frequencies at microwave band, 150 GHz, 220 GHz and 340 GHz, are proposed for the microwave sensor of the FY-4 satellite. RT simulations carried out at the three frequencies are presented in the following sections, to investigate the potential of polarized signatures for ice cloud characterization. The habits of ice particles are categorized to platelike, columnlike and irregular shapes (*Noel et al., 2006*). Thus, ice particles in this chapter are assumed to be perfectly circular plates and columns with preferential orientation, since planar and columnar particles count for a large number in ice clouds (*Noel and Sassen, 2005*).

6.2 RT simulations at FY-4 window channels

In this section, the effects of oriented ice particles on PD and TB are discussed, to evaluate the potential role of polarization in determining ice cloud parameters. For this purpose, atmospheric conditions are reconstructed (Section 6.2.1). Horizontally-oriented ice particles are assumed in the RT simulations (Section 6.2.2), and the sensitivities of ice particle parameters to PD and TB are examined (Section 6.2.3), by assuming ice particles with preferred orientation.

6.2.1 RT setup

For RT simulations, assumptions on microphysical parameters of ice particles are made. Ice clouds are located at an altitude ranging from 9 km to 11 km (MSL), which is the typical height of cirrus clouds in the mid-latitude (*Minnis et al., 1990*). The empirical sizes of plates and columns in ice clouds are shown in Table 6.1 and Table 6.2, respectively, according to the model of *Heymsfield (1972)*. The maximum dimension is the diameter (the length) of the circular ice plate (column), and its AR is expressed as the ratio of the maximum dimension to its minimum dimension. The equivalent-volume spherical radius (E/V radius) of the circular plates (circular columns) is distributed in the range of $10 \mu\text{m} - 358 \mu\text{m}$ ($10 \mu\text{m} - 503 \mu\text{m}$). Considering the possible extreme sizes of ice particles (thin plates or long columns with an AR up to 30), the DDA algorithm (*Draine and Flatau, 2004*) is employed to calculate the scattering properties of ice particles.

Ice particles in clouds are assumed to be distributed in a Gamma size distribution (*Evans and Stephens, 1995b; Miao et al., 2003*) and the relation between the particle concentration $N(D_e)$ and its dimension D_e (E/V diameter) is given as

$$N(D_e) = N_0 D_e^{\alpha_0} e^{-\frac{(\alpha_0 + 3.67) D_e}{D_m}} \quad (6.1)$$

where N_0 (in m^{-4}) is chosen to normalize IWP values, α_0 is the width parameter and D_m is the median mass diameter of the ice particle.

Table 6.1: The empirical sizes of circular columns. (From *Xie and Miao*, 2011)

Equivalent-volume spherical radius / μm	Maximum dimension of plates / μm	Minimum dimension of plates / μm	Aspect ratio
10	25.4	8.3	3.1
39	132.1	18.1	7.3
68	259.2	25.0	10.4
97	398.7	30.6	13.0
126	547.6	35.6	15.4
155	703.9	40.1	17.6
184	866.7	44.2	19.6
213	1035.0	48.1	21.5
242	1208.2	51.8	23.3
271	1386.0	55.3	25.1
300	1567.8	58.6	26.8
329	1753.4	64.8	28.4
358	1942.5	67.1	30.0

Table 6.2: The empirical sizes of circular plates. (From *Xie and Miao*, 2011)

Equivalent-volume spherical radius / μm	Maximum dimension of columns / μm	Minimum dimension of columns / μm	Aspect ratio
10	32.5	12.8	2.5
39	135.7	48.3	2.8
68	243.4	83.0	2.9
97	353.6	117.3	3.0
126	465.5	151.4	3.1
155	578.7	185.3	3.1
184	693.0	219.0	3.2
213	808.3	252.5	3.2
242	924.4	286.0	3.2
271	1041.1	319.3	3.3
300	1158.6	352.6	3.3
329	1276.6	385.7	3.3
358	1395.1	418.8	3.3
387	1514.1	451.8	3.4
416	1633.6	484.8	3.4
445	1753.5	517.7	3.4
474	1873.9	550.6	3.4
503	1994.5	583.3	3.4

The Gamma size distribution can be reduced to an exponential distribution when $\alpha_0 = 0$. In this study, α_0 is equal to 1 and D_m ranges from 50 μm to 500 μm . Particles are assumed to be pristine ice with a bulk density of 0.92 g/cm^3 .

Furthermore, the earth surface is regarded as a Lambertian surface with an emissivity of 0.9 for RT input. Sixteen Lobatto quadrature angles per hemisphere are calculated. The atmospheric profile for RT simulations is the averaged profile of the Beijing area (*Xie and Miao, 2011*). The complex refractive index of ice particles at the window channel frequencies of the FY-4 satellite is calculated by the model of *Mätzler (2006)*.

6.2.2 Ice particles with horizontal orientation

The contour graph of TB difference between cloudy and clear sky ($\Delta\text{TB} = \frac{\text{TB}_{v,\text{cloudy}} + \text{TB}_{h,\text{cloudy}}}{2} - \text{TB}_{\text{clear}}$, hereinafter called TB depression) caused by the horizontally-aligned plates with empirical sizes is shown in the top panel of Figure 6.1, while PD is shown in the bottom panel. TB observed from space is depressed with the presence of IWP. In contrast to ground-based observations, the PD values are positive due to the dichroism effects of horizontally oriented ice particles. Increasing the D_m and IWP, the scattering effects of ice clouds increase and result in an increase of TB depression (ΔTB) and PD (Figure 6.1). However, PD begins to be saturated when IWP increases drastically (Figure 6.1, bottom panel). When the large circular plates with a horizontal orientation are gradually predominant in ice clouds, the scattering effects become enhanced and result in strong dichroic scattering effects. Therefore, both ΔTB and PD increase with D_m . With a D_m of 300 μm , TB depression is up to 80 K at 340 GHz (Figure 6.1, top panel). PD is less than 5 K with an IWP lower than 100 g/m^2 and a D_m less than 100 μm , while PD is up to 50 K when D_m increases up to 300 μm (Figure 6.1, bottom panel). Note that all the results in this section are revealed at a zenith angle of 52.8°, which is close to viewing angles of many present space-borne radiometers.

Figure 6.2 shows PD and TB as a function of IWP and D_m for horizontally aligned columns. Compared with ΔTB caused by plates, a similar behavior of TB depression is found for ice columns (Figure 6.2, top panel). TB is strongly depressed by columnar crystals and the scattering effects of ice columns increase with the particle size and IWP (Figure 6.2, top panel). While the “resonance” feature of PD occurs for ice columns with empirical sizes (Figure 6.2, bottom panel), it is not found for ice plates with horizontal orientation (Figure 6.1, bottom panel). The position of the resonance peak is found to be associated with particle sizes with respect to frequency. Figure 6.3 shows the PD peak position as a function of D_m , assuming horizontally aligned ice columns with an AR of 2, the empirical sizes (AR ranging from 2.5-3.4) and an AR of 5. At 340 GHz, the position of the PD resonance peak moves to a larger D_m when the particle AR increases (Figure 6.3). For the empirical AR of columns ranging between 2.5 and 3.4 (Table 6.2), the PD peak is located at a D_m of ~ 400 μm , and it reaches a maximum at a D_m of ~ 425 μm when the column AR is 5, while the peak position moves to a D_m of ~ 375 μm if the AR is equal to 2. The position of the resonance peak also depends on IWP, i.e., it moves from $D_m = \sim 400$ μm at an IWP of 20 g/m^2 to $D_m = \sim 300$ μm at an IWP of 200 g/m^2 (Figure 6.2, bottom panel). However, PD is apparently saturated when IWP increases up to 200 g/m^2 and its resonance peak moves to a shorter D_m .

A similar “resonance” feature is found for ice columns at 220 GHz with an IWP of 400 g/m^2 (not shown), but not at the frequency of 150 GHz (Figure 6.4). The resonance feature

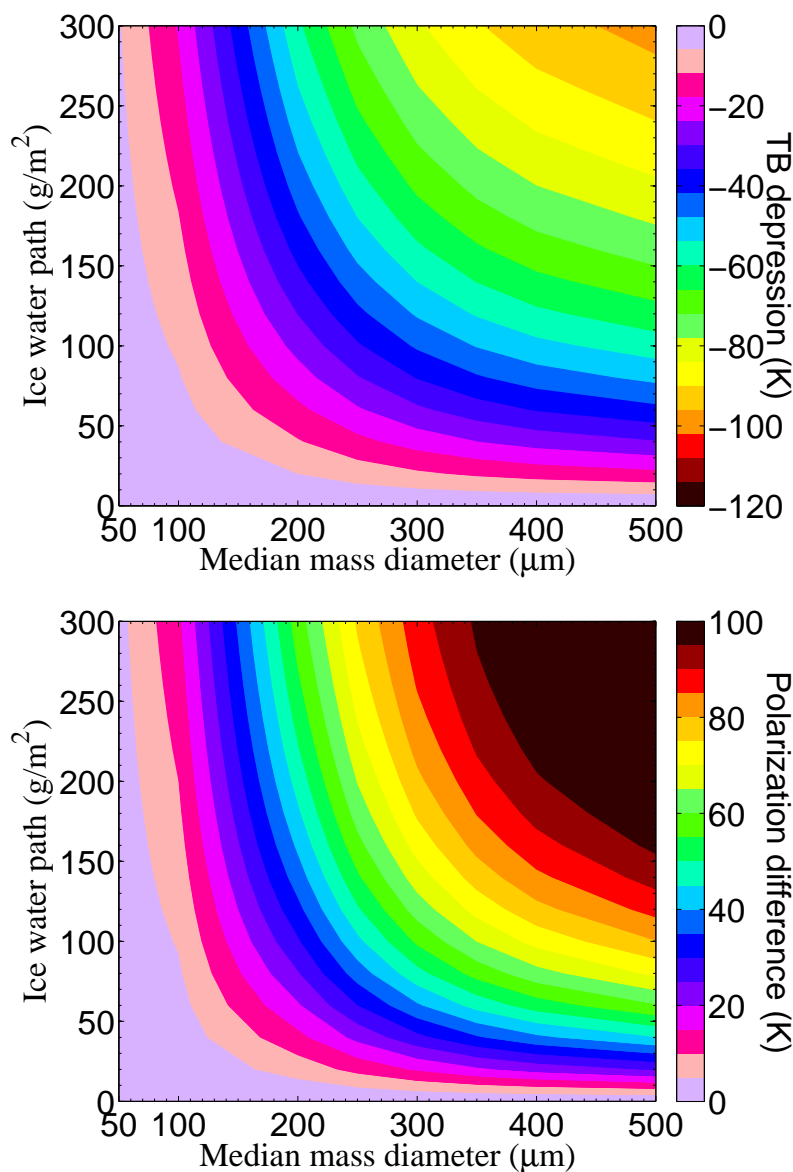


Figure 6.1: Top panel: Brightness temperature difference between clear and cloudy skies as a function of ice water path (IWP) and median mass diameter (D_m) for horizontally oriented planar crystals with empirical sizes at an zenith angle of 52.8° at 340 GHz. Bottom panel: Same as the top panel except that colors indicate polarization difference due to horizontally oriented planar crystals with empirical sizes. (From *Xie and Miao*, 2011)

is caused by the scattering characteristics of ice particles, i.e., their scattering behavior is mainly sensitive to particles with a specific size with respect to frequency.

In addition, it is found that TB is mostly sensitive to IWP, while PD is much more sensitive to particle habit and size. The difference of TB depression caused by horizontally aligned plates and columns is less than 2 K when IWP is less than 100 g/m^2 at 340 GHz (Figure 6.1 and Figure 6.2, top panels). The dichroism effects by planar crystals are much stronger than in case of ice columns. Thus, PD due to horizontally oriented plates is much stronger than the corresponding value calculated with columnar crystals, when comparing Figure 6.1 to

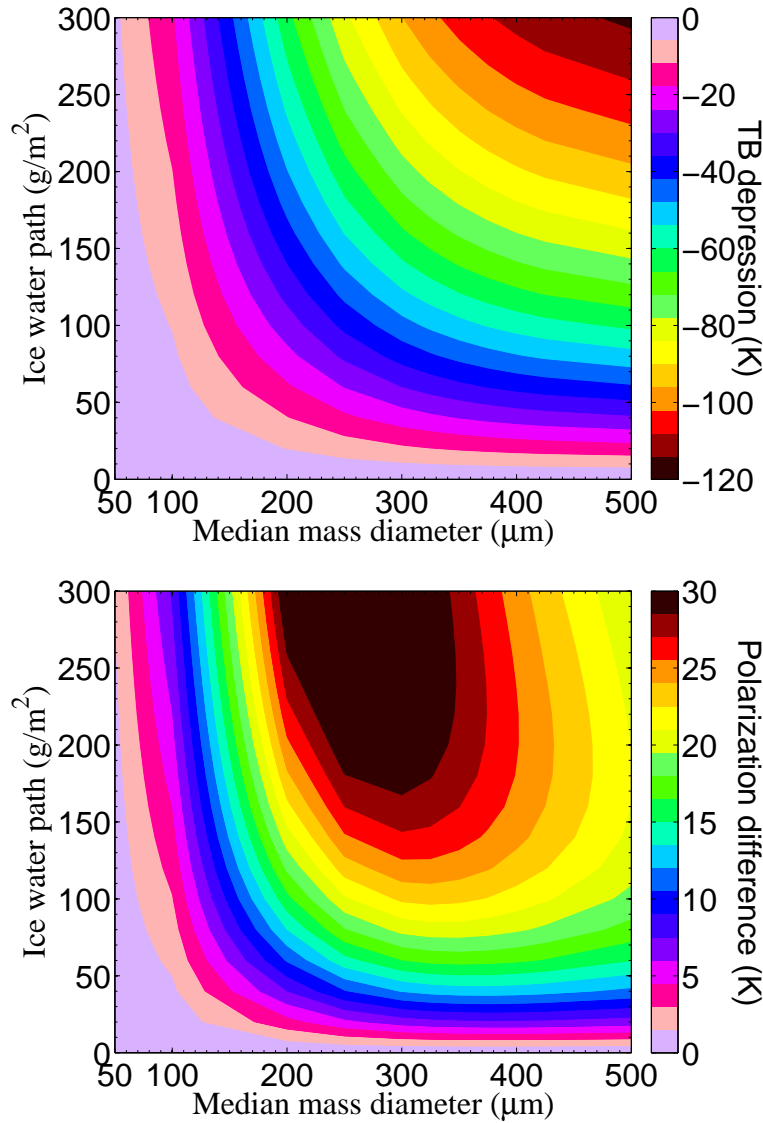


Figure 6.2: Same as Figure 6.1, except for circular ice columns with empirical sizes. (From *Xie and Miao*, 2011)

Figure 6.2. PD is much more sensitive to the higher frequency channel than to the lower 150 GHz and 220 GHz channels. At 340 GHz, PD increases from 0 to 30 K when D_m increases to 200 μm , while for 150 GHz and 220 GHz channels the corresponding increase of PD is less than 15 K. However, PD is easily saturated by the increasing optical depth at the high frequency channels, especially for larger IWP and D_m values. Thereby, high frequency channels can be much more useful for thinner and smaller crystal clouds, while lower channels can be used to detect thick clouds. These findings are consistent with some conclusions in *Buehler et al.* (2007).

6.2.3 Ice particles with canting angles

Most ice particles in clouds are likely to be aligned with their maximum dimension parallel to the ground surface, with a deviation of less than 3° , as described in, e.g., *Noel and Sassen*

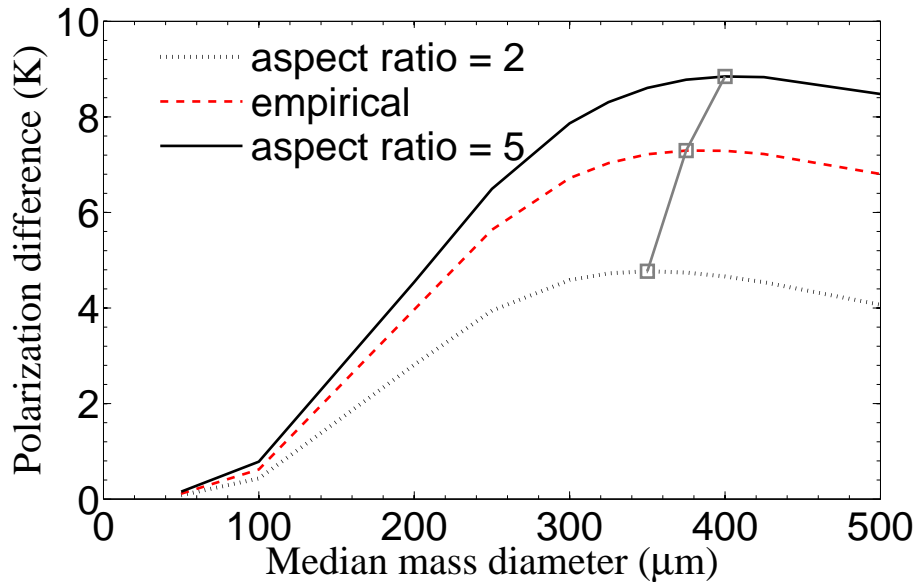


Figure 6.3: Polarization difference (PD) as a function of median mass size diameter of ice particles at 340 GHz. Horizontally oriented columns are assumed to be with an aspect ratio of 2 (the dotted line), empirical size (the slashed line) and 5 (the solid line). The gray square markers indicate the position of the resonance peak caused by the scattering of columns. IWP is 20 g/m^2 . Note that PD is shown at a zenith angle of 52.8° . (From *Xie and Miao, 2011*)

(2005); *Noel et al. (2006)*. However, canting angles can be sometimes introduced because of the external turbulence or electrification processes. To investigate the effects of ice particle orientation on the scattering effects, the truncated Gaussian distribution is assumed for the distribution of ice particle orientation (Equation 5.3 in Section 5.2). The WP in the truncated Gaussian distribution determines the preferred orientation of ice particles. Varying the WP from 0 to infinite, the weight from high canting angles becomes important and ice particles change gradually from horizontally oriented to randomly.

Figure 6.5 and Figure 6.6 show the effects of crystal canting angles on PD and TB caused by planar and columnar particles, respectively. The top panels show the TB depression and the bottom panels shown PD caused by oriented ice particles. Generally, ice particles with horizontal orientation cause the strongest dichroism effect and largest PD, and PD due to particles with preferred orientation is larger than in case of random orientation. Horizontally aligned particles behave similarly to oriented particles with a WP of 10, and the difference of TB depression is less than 0.2 K. This can be explained by the weights in the Gaussian distribution where the weights are mostly from the horizontally oriented ice particles when WP is less than 10. When ice particles gradually orient from horizontally to randomly, PD decreases, by a factor of $\sim 3 - 4$ (Figure 6.5 and Figure 6.6, bottom panels). This can be caused by the scattering properties of ice particles with different orientation. Horizontally aligned crystals result in greater positive signals than those with extreme canting angles away from the horizontal orientation (Figure 5.5). When the radiance propagates in the dichroic medium characterized by perfectly vertically oriented crystals, the horizontal component dominates the upwelling TB received by the downward viewing sensor from space.

The orientation of ice particles also affects TB (Figure 6.5 and Figure 6.6, top panels). When

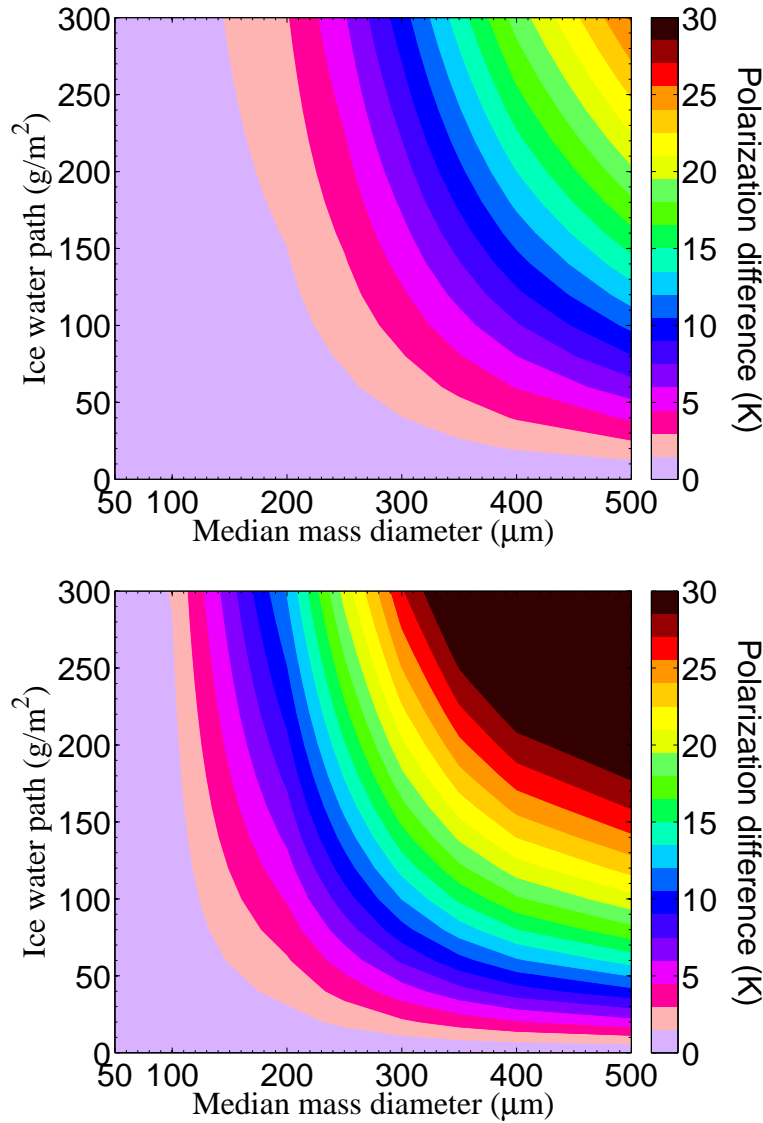


Figure 6.4: PD caused by horizontally aligned columns at the frequency of 150 GHz (top panel) and 220 GHz (bottom panel). (From *Xie and Miao*, 2011)

ice particles gradually become randomly oriented, TB increases about 6 K for both shapes since scattering effects are reduced for the non-dichroic material. However, the difference of the TB depression caused by the two different shapes is small. These results are in consistency with the RT simulations by oriented oblates (Chapter 5). In contrast to snow oblates, the scattering and dichroism effects of ice particles are much stronger. This can be explained by the extreme AR of ice particles which results in higher scattering effects and the constant refractive index of ice particles at various sizes.

6.3 Conclusions

In this chapter, the effects of nonrandomly oriented circular plates and columns on PD and TB were examined to investigate the potential role of PD in cirrus cloud detection. The

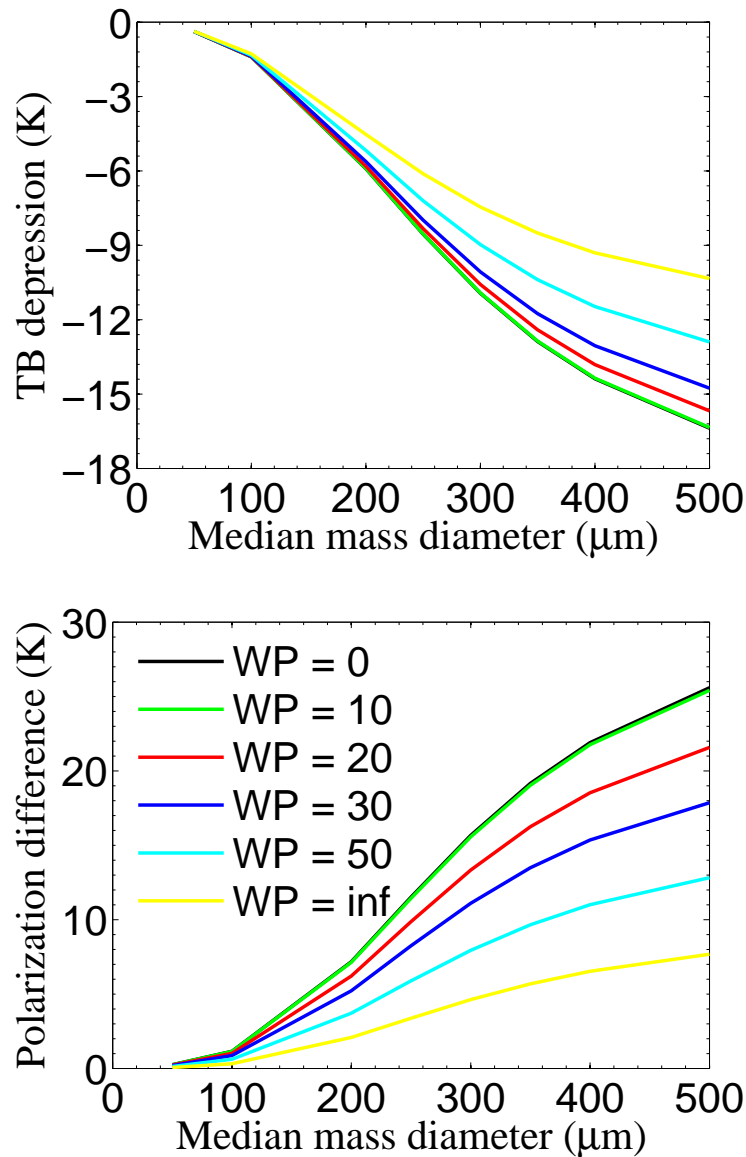


Figure 6.5: Effects of plate orientation. Top panel (bottom panel) reveals the effects of planar particle orientation on brightness temperature depression (polarization difference). The IWP is chosen to be 20 g/m^2 and the width parameter (WP) in the truncated Gaussian distribution changes from 0 to infinite, i.e., the particle orientation varies from horizontally to randomly. (From *Xie and Miao*, 2011)

scattering properties of oriented ice particles were calculated with the DDSCAT6.1 code package (*Draine and Flatau*, 2004), and the RT calculations were carried out by a polarized RT model (Chapter 2). The results showed clearly the benefits of polarization observations for ice cloud parametrization.

- (a) PDs are sensitive to particle aspect ratio, shape and orientation. Polarization observations offer additional information on ice cloud microphysics. TBs which are more sensitive to IWP are useful for the integrated amount of ice in clouds. In addition, the upwelling TB depression caused by ice clouds is affected by particle orientation,

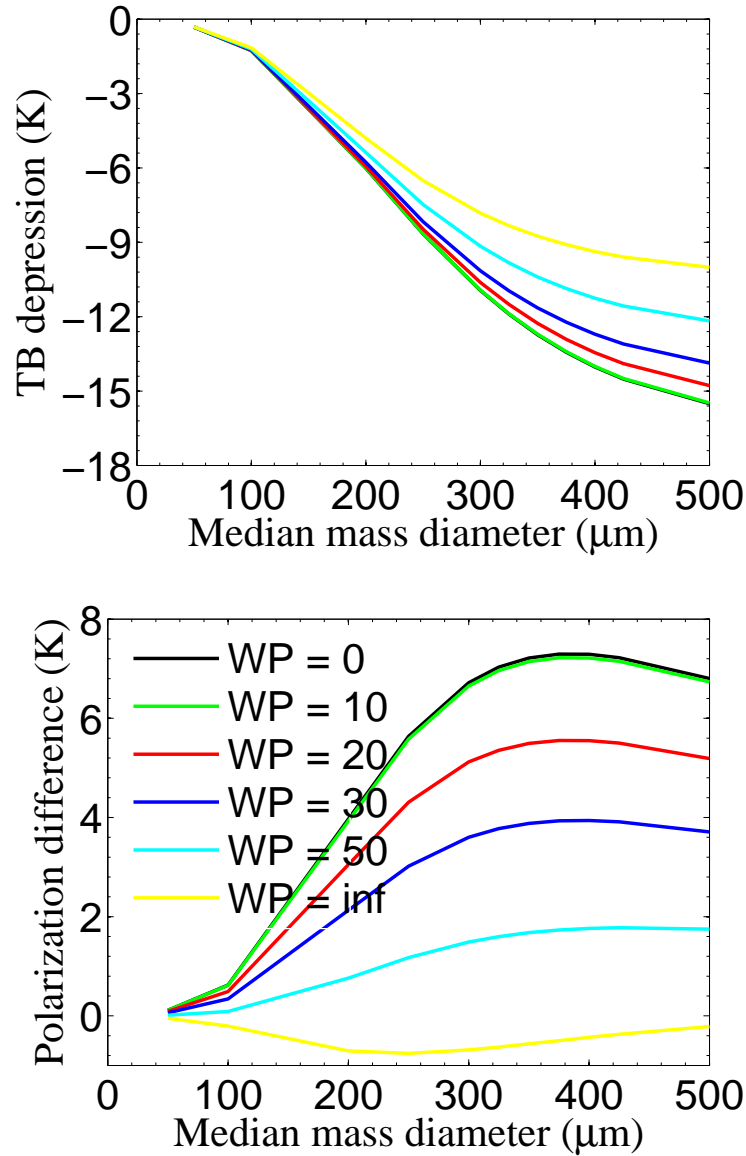


Figure 6.6: Same as Figure 6.5, except for the effects of column orientation on TB and PD. (From *Xie and Miao, 2011*)

since the scattering characteristics of ice particles vary with their orientation. When the ice particles change from horizontally to randomly oriented, the shift of TB is up to 6 K at 340 GHz. Therefore, to accurately retrieve IWP, polarization measurements are necessary for the related information on crystal orientations.

- (b) PD due to the columnar crystals shows a “resonance” feature at higher frequencies (220 GHz and 340 GHz), but there is no notable resonance characteristic for horizontally oriented plates at the three estimated FY-4 frequencies. The position of the resonance peak greatly depends on crystal size and IWP in ice clouds. PD peak position moves towards a longer D_m if the channel frequency or particle AR increases. The resonance behavior of PD can offer additional information for retrievals of cloud microphysical parameters though it depends on IWP, D_m , particle shape and orientation. Due to the

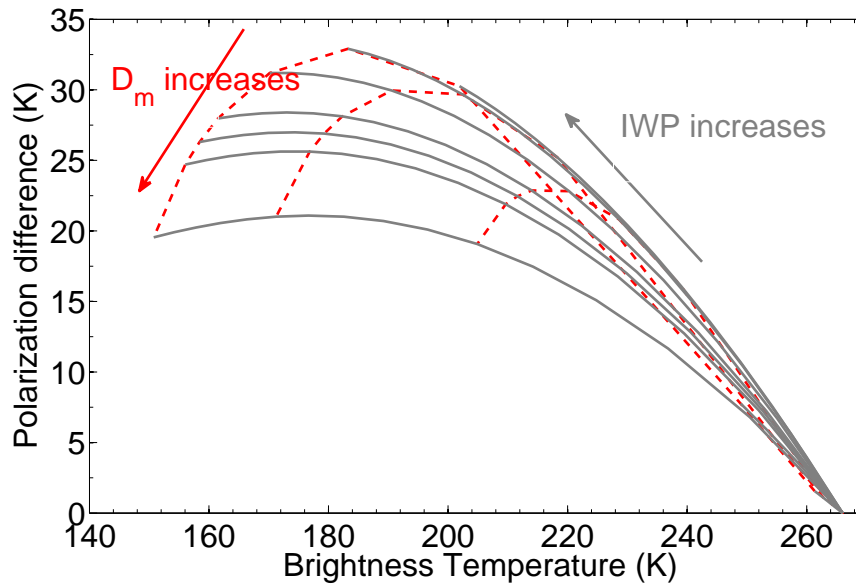


Figure 6.7: PD and TB calculated with different D_m and IWP in clouds. The red slashed lines along the red arrow indicate the increase of D_m , while the gray lines along the gray arrow specify the increasing IWP. Ice crystals are assumed to be horizontally aligned columns. RT simulations are performed at 340 GHz.

response at different frequencies, it is possible to find the resonance characteristics if the channels at different frequencies are combined.

- (c) When the ice particles change from horizontal to random orientation with the increase of the WP in the truncated Gaussian distribution, the dichroism effects of ice particles are weakened and PD decreases. Meanwhile, their scattering effects are also reduced and TB depression is lower for randomly oriented crystals. The resonance position moves to a longer D_m for ice columns when the WP increases.
- (d) For the Lambertian surface, its emissivity has a great effect on the brightness temperature, while it has very limited influence on PD, especially at higher frequencies where water vapor absorption screens the surface effects. In case of a polarized surface, e.g., the water surface, PD can still provide information for cloud retrievals if the polarized signals from the surface are discriminated from ice particles by other techniques.

In this chapter, only perfectly shaped particles were considered, i.e., circular ice plates and columns, and ice particles were assumed to be all with the same single habit. The uncertainties in ice parameters cause PD and TB uncertainties in RT calculations. However, it is noticed that with polarization information it could be possible to retrieve microphysical parameters of ice clouds.

Figure 6.7 shows PD and TB calculated with different IWP and D_m at 340 GHz from space, by assuming horizontally oriented ice columns in clouds. IWP increases along the gray arrow, while D_m increases along the red arrow. It is difficult to distinguish the effects of D_m and IWP if only the TB signals are obtained from observations. PD combined with TB observations can constrain ice cloud retrievals. A specific PD/TB combination corresponds to D_m and IWP. However, on the one hand, for the lower frequencies, e.g., 150 GHz, from

space perspective it is difficult to derive ice microphysical parameters even if the polarization information is used, due to the channel sensitivity. The low frequencies are more connected to the IWP. On the other hand, both the increase of IWP and D_m can result in the PD saturation, especially at higher frequency channels where the PD is saturated at a lower IWP and D_m . The accuracy of ice cloud retrievals by means of high frequencies will be improved when the IWP is provided by other measurements. Thus, for the improvement of retrieval accuracy, it is important to combine low frequency channels with high frequencies in the future study.

Chapter 7

Summary and outlook

In this work, polarization observations of oriented frozen hydrometeors with microwave radiometry were presented during snowfall, and the benefits of polarized signals for ice cloud retrievals and the new instrument design were analyzed with RT simulations. To understand the radiation interaction in the atmosphere, RT theory was introduced in Chapter 2. A polarized RT model was introduced to analyze the radiative interactions in the atmosphere. For the calculations of scattering properties, the T-matrix and DDA methods that were employed in this study were briefly reviewed (Chapter 2). The instruments employed in this study and the auxiliary observations at UFS were presented in Chapter 3 to observe polarized signals during snowfall. Together with the passive and active instruments deployed at UFS in Germany (Chapter 3), the polarization observations performed by DPR at 150 GHz were analyzed during snowfall (Chapter 4). A second microwave radiometer HATPRO observes IWV and LWP, and MRR provides indirect SWP measurements during snowfall. Based on the snowfall measurements in 2010 (Chapter 3), the observed PD and TB at 150 GHz were described as a function of LWP and SWP (Chapter 4). By this fact, the dependencies of PD and TB on snowfall parameters were further studied (Chapter 4). The polarization observations were characterized well by the RT simulations where the atmospheric conditions were reconstructed (Chapter 5). The RT simulations verified the existence of preferentially oriented frozen hydrometeors during snowfall and further evaluated the effects of their microphysical parameters on PD and TB (Chapter 5). Polarization observations for ice cloud characterization are applicable to improve the retrieval accuracy of ice clouds which are characterized by oriented frozen hydrometeors and promote the design of space-borne microwave radiometers (Chapter 5 and Chapter 6).

Instrumentation and data set

To observe PD caused by oriented snow particles, polarization observations were carried out at UFS by DPR at 150 GHz. The DPR observations were quality-controlled by a surveillance camera during daytime and night. A 90 GHz channel of DPR measures synchronously with the two polarized channels at 150 GHz. Other auxiliary observations at UFS provided important parameters during snowfall, including LWP, indirect SWP and synoptic data.

Due to calibration uncertainty, PD showed a bias of ~ 2 K even at an elevation angle of 90° (Figure 3.1). To correct for the PD bias during snowfall, the PD during clear sky in 2010

was analyzed. The results indicated that DPR has a systematic but stable offset. A total duration of snowfall was found to be 458 hours in 2010 (Figure 3.2).

Polarization observation during snowfall

With the analysis of a single snow case and a 458-hour snowfall data set in 2010, the observation results showed that the PD signal caused by oriented snow particles was up to -10 K at an elevation angle of 34.8° during snowfall (Figure 4.1 and Figure 4.3). However, for most snow cases in 2010, the observed PDs were around -2 K at 150 GHz and the median LWP derived from the HATPRO observations was on the order of 100 g/m² during snowfall (Figure 4.3). To figure out why PD values were around -2 K for most snow cases, DPR measurements were analyzed together with HATPRO and MRR observations. Based on the analysis, the dependencies of PD and TB on SWP and LWP were found. The analysis showed that SWP enhances both PD and TB, while the existence of LWP during snowfall strongly enhances TB but damps PD. The PD values up to -5 K were found only when the observed LWP was lower than 200 g/m² during snowfall.

The synchronously observed TBs at 90 GHz were analyzed with the PD and TB at 150 GHz at 34.8° elevation angle. The TB90 signals are drastically affected by the strong emission of supercooled liquid water (Figure 4.6) when compared to the HATPRO observed LWP which was shown as a function of PD and TB combinations (Figure 4.3).

According to the polarization observations presented in this study, it is necessary to improve the accuracy of microwave radiometers in order to observe the potential PD signals caused by oriented frozen hydrometeors, especially at the sites where the PD is seriously damped by the strong absorption of supercooled liquid water. Meanwhile, due to the scattering characteristics of snow particles, the optimized elevation angle ranges between 20° and 50° elevation angle where PD reaches maximum.

In addition, although the dependence of PD and TB on the 2m-temperature recorded by the weather station at the summit of Mount Zugspitze was examined, it was difficult to conclude whether the PD/TB combinations are correlated to the local atmospheric conditions or not. The observations at UFS were not sufficient to obtain snow type information by means of the available instruments. For more information on the snowfall types, long-term observations at UFS are now complemented by a cloud radar operating at 35.2 GHz.

RT simulations

The observed PD and TB during snowfall were characterized well by assuming reasonable snow parameters in RT simulations. The effects of SWP and LWP on PDs and TBs were confirmed by the RT simulations, under the assumption of horizontally oriented snow oblates during snowfall (Section 5.1.2). Regarding to the frequent presence of LWP during snowfall, its “damping (enhancing)” effects on PD (TB) during snowfall were further explained by a simple physical model (Section 5.3). RT simulations with the simple model showed that PD is absorbed by the supercooled liquid water which is located lower than the dichroic snow layer, while for supercooled liquid water above the snow layer, its “damping” effects on PD are caused by the compensation of the liquid water emission penetrating through the dichroic

snow layer. The enhancing effects of LWP on TB can be concluded as: the warmer the liquid water, the higher the TB.

However, the mismatch between the observations and RT simulations still exists (Figure 5.1) and it can be explained by different observation geometries and the simplified snow microphysical parameters in the RT simulations. The mismatch due to the different observation geometries can be solved by synchronizing the instruments in future observations, while the simplified snow microphysical parameters still result in significant uncertainties in the RT simulations.

All retrieval algorithms require an accurate and realistic representation of snow microphysics. However, realistic snow particles have far more complex habit and size, especially under varying atmospheric conditions. A reasonable representation of snow parameters becomes important in the retrievals, due to the sensitivities of PD and TB to snow parameters. Any change in the microphysical parameters of snow particles, i.e., their aspect ratio, preferred orientation and mass size relationships, etc., can cause significant uncertainties in PDs and TBs, up to several Kelvins (Section 5.2). PDs and TBs are underestimated for randomly-oriented or rounder snow particles in the RT simulations. Especially the fluffy ice-air mixed snow oblates by the Maxwell-Garnett assumption reduce scattering effects and further underestimate PDs and TBs.

To better represent snow microphysical parameters in the retrievals, it is necessary to model the scattering properties of snow particles with preferential orientation and more realistic habit, by using, e.g., the DDA algorithm. In contrast to traditional scattering databases (e.g., *Liu, 2008; Hong et al., 2009*), a new scattering database is needed to be established to calculate particle scattering properties in a wide frequency and temperature range, in which the polarization characteristics of preferentially oriented particles should be taken into consideration.

Moreover, considering the inhomogeneous ice clouds which vary temporally and spatially, a three dimensional RT model with full polarizations should be employed in order to better reconstruct in-situ atmospheric conditions. When the optical depth due to atmospheric scattering of frozen hydrometeors increases, especially at high microwave frequencies, single scattering properties can not represent well radiative interaction in ice clouds. Thus, multiple scattering effects between frozen hydrometeors which become much prominent at high frequencies need to be taken into account.

Implications of polarization information on snow retrievals

Polarization observations can benefit the accuracy of retrieval algorithms. The scattering effects of snow particles are weakened by the assumption of randomly oriented particles (Figure 5.7). Thus, TBs are underestimated in RT simulations from the ground-based viewing. The proposed algorithm for snow retrievals is to combine PD with TB. One specific PD and TB combination therefore corresponds to SWP and LWP values. By assuming reasonable snow microphysical parameters, the retrieved SWP and LWP show good consistency with the observations (Figure 5.1). The performance of this algorithm greatly depends on the representation of snow parameters in RT simulations. The varying snow microphysical parameters pose essential uncertainties in snowfall retrievals.

Apart from the complex snow parameters, the presence of supercooled liquid water during snowfall makes snow retrieval much bewildering. It is important for passive microwave ra-

diometry to distinguish the liquid water emission from snow scattering, since the observed radiation in the microwave spectrum is the summed signal of the liquid water emission and snow scattering. To solve this problem, observations at 90 GHz should be taken into account as auxiliary information, since TBs at 90 GHz channel are mostly sensitive to the emission of cloud liquid water. It presents big potential for LWP retrievals especially during snowfall. On the one hand, the 90 GHz channel can be useful to avoid the LWP mismatch between the observations and RT simulations due to different observation geometries, since this channel observes synchronously with the two orthogonal channels at 150 GHz. On the other hand, while the sensitivity of the 90 GHz channel to SWP is much weaker, TB90 is mainly enhanced by the emission of cloud liquid water during snowfall and its sensitivity to LWP can be comparable to the 150 GHz channels. When TB90 and LWP are both revealed as a function of the PD/TB combinations at 150 GHz, TB90 highly correlates with LWP.

The temperature dependence of supercooled liquid water emission makes snowfall retrieval much more complicated since the emission from supercooled liquid water affects the observed PD and TB. PDs and TBs are deviated by the emission of supercooled liquid water when the radiative properties of supercooled liquid water change. Although the frequent presence of cloud liquid water poses an important uncertainty in snow retrievals, it is possible to retrieve snow parameters by analyzing cloud liquid effects on PDs and TBs. When the information on supercooled liquid water can be provided by other techniques, the retrieval algorithm using the PD and TB combinations can be applied to snowfall retrievals (Figure 5.16).

Implications of polarization observation for instrument design

Another application of polarization observations is to promote new instrument design. So far, most of the existing instruments, either space-/air-borne or ground-based microwave radiometers, are only equipped with one single polarization since it is unclear whether polarized signals due to oriented particles would be beneficial to ice cloud retrievals or not. A large number of retrievals assumes spherical or randomly oriented ice particles in the scattering properties and radiative transfer calculations and the polarization signature caused by frozen hydrometeors is treated to be zero (e.g., *Evans et al.*, 2002; *Buehler et al.*, 2007).

The geostationary space-borne satellite FY-4 in China, which is proposed to be equipped with polarized channels at the three window frequencies, i.e., 150 GHz, 220 GHz and 340 GHz, was analyzed in this study. The results show that platelike ice particles induce much stronger PD than columns. A typical PD characteristic due to ice columns is a “resonance” feature caused by the scattering effects of particles which are mainly sensitive to a specific size at a specific frequency. PD is sensitive to ice particle habit and aspect ratio, while TB is more sensitive to total ice amount. A retrieval algorithm is proposed for ice cloud parametrization by means of the PD and TB combinations (Figure 6.7). Additional information will be provided by polarization observations to quantify ice clouds since the orientation of ice crystals has significant effects on both PD and TB. Microphysical parameters of ice clouds can be derived by the polarized channels at high frequencies combining with low frequency channels. Therefore, microwave polarization instruments aboard space-borne satellites can be beneficial to ice cloud observations.

List of acronyms

2DVD	2-Dimensional Video Disdrometer
ADMIRARI	ADvanced MICrowave RAdiometer for Rain Identification
AGL	Above Ground Level
AMSU-B	Advanced Microwave Sounder Unit-B
AR	Aspect Ratio
CALIPSO	Cloud-Aerosol Lidar and Infrared Pathfinder Satellite Observation
CIWSIR	Cloud Ice Water path Submillimetre Imaging Radiometer
CoSSIR	Compact Scanning Submillimeter Imaging Radiometer
CRYSTAL-FACE	Regional Study of Tropical Anvils and Cirrus Layers Florida Area Cirrus Experiment
DPR	dual polarized microwave radiometer
DDA	Discrete Dipole Approximation
DDSCAT	DDA code package provided by Draine and Flatau
DWD	Deutscher Wetterdienst
EOS	Earth Observatory System
FDTD	Finite-Difference Time Domain
FM-CW	Frequency Modulated Continuous Wave
FY-4	FengYun-4 Satellite
HATPRO	Humidity And Temperature PROfiler
HPBW	Half Power Beam Width
IWC	Ice Water Content
IWP	Ice Water Path
IWV	Integrated Water Vapor
JPL	Jet Propulsion Laboratory
LIDAR	LIght Detecting And Ranging
LWC	Liquid Water Content
LWP	Liquid Water Path
METEK	Meteorologische Messtechnik GmbH
MLS	Microwave Limb Sounder
MRR	Micro Rain Radar
MSL	Mean Sea Level
PD	Polarization Difference
RPG	Radiometer Physics GmbH
RT	Radiative Transfer
SMMR	scanning multichannel microwave radiometer
SSM/I	Special Sensor Microwave Imager
SWCIR	Submillimetre-Wave Cloud Ice Radiometer
SWP	Snow Water Path

TB	Brightness Temperature
TB90	Brightness Temperature at 90 GHz
TOSCA	Towards an Optimal estimation based Snow Characterization Algorithm
UARS	Upper Atmosphere Research Satellite
UFS	Umweltforschungsstation Schneefernerhaus
UTC	Coordinated Universal Time
WP	Width Parameter in truncated Gaussian function

List of symbols

a_n, b_n	expansion coefficients in the Mie theory
$\mathbf{a}, \mathbf{b}, \mathbf{p}, \mathbf{q}$	expansion coefficients in the T-matrix method
c	speed of light
d	distance
h	Planck constant
i	imaginary unit
k	wave number
k_B	Boltzmann constant
m	mass
m_0	refractive index
\hat{n}	wave propagation direction
\mathbf{r}	wave propagation vector
r_e	equivalent volume spherical radius
s	wave propagation path
t	time
\hat{v}, \hat{h}	unit vectors in vertical / horizontal directions
x	size parameter
A_e	effective area
B_λ	intensity
$C_{ext}, C_{sca}, C_{abs}$	extinction / scattering / absorption cross section
D	particle size
D_e	equivalent volume spherical diameter
D_m	median mass diameter
E	energy
\mathbf{E}	electric field
$\mathbf{E}_h, \mathbf{E}_v$	electric field vector at vertical / horizontal direction
E_{0v}, E_{0h}	electric field complex amplitude at vertical / horizontal direction
E_v, E_h	electric field amplitude at vertical / horizontal direction
$F_{vv}, F_{vh}, F_{hv}, F_{hh}$	elements in amplitude scattering matrix
H_2O	water vapor
$\vec{\mathbf{I}}$	Stokes vector
I, Q, U, V	four Stokes parameters
I_v, I_h	intensity at vertical / horizontal polarization
I_λ	specific radiative intensity
\vec{K}	extinction matrix
K	extinction matrix element
\vec{M}	scattering matrix

M	scattering matrix element
N_0	parameter in exponential size distribution
N_i, N	particle number
N_2	nitrogen
O_2	oxygen
P, P_L, P_C	degree of polarization, degree of linear polarization, degree of circular polarization
PD	polarization difference
\vec{R}	reflection matrix
\vec{S}	source vector
\bar{S}	amplitude scattering matrix
T	temperature
\mathbf{T}	transition matrix
\vec{T}	transmission matrix
TB	brightness temperature
TB_h, TB_v	brightness temperature at horizontal / vertical polarization
TB90	brightness temperature at 90 GHz
Z_e	reflectivity factor
α_0	parameter in Gamma-size distribution
$\bar{\alpha}, \bar{\beta}, \bar{t}$	matrix
β, θ, ϕ	Euler angle
$\beta_{ext}, \beta_{sca}, \beta_{abs}$	extinction / scattering / absorption coefficient
η, ζ	angles expressing electric wave
ε_λ	emissivity
ε_0	permittivity
λ	wavelength
ω	wave angular frequency
ω_0	single scattering albedo
φ	azimuth direction
ϑ	zenith angle
μ	cosine of zenith angle
μ_0	magnetic permeability
τ	optical depth
$\vec{\sigma}$	emission vector
σ	emission vector element
Δ_h, Δ_v	phase of the electric field complex amplitude
Δ_{v-h}	relative phase of electric field vectors
Λ	slope coefficient in exponential size distribution
Ω	solid angle

Bibliography

- Armstrong, R. L., and E. Brun, *Snow and climate*, Cambridge University Press, 2008, 222 pp.
- Battaglia, A., and C. Simmer, Explaining the polarization signal from rain dichroic effects, *Journal of Quantitative Spectroscopy and Radiative Transfer*, 105, 84–101, 2007.
- Battaglia, A., C. Simmer, S. Crewell, H. Czekala, C. Emde, F. Marzano, M. Mishchenko, J. Pardo, and C. Prigent, Emission and scattering by clouds and precipitation, in *Thermal Microwave Radiation: Applications for Remote Sensing, IET Electromagnetic Waves Serial Volume 52*, edited by C. Mätzler *et al.*, pp. 101–223, The Institution of Engineering and Technology, Stevenage, U. K, 2006.
- Battaglia, A., P. Saavedra, C. Simmer, and T. Rose, Rain observations by a multifrequency dual-polarized radiometer, *IEEE Geoscience and Remote Sensing Letters*, 6, 354–358, 2009.
- Bennartz, R., and G. W. Petty, The sensitivity of microwave remote sensing of precipitation to ice particle size distribution, *Journal of Applied Meteorology*, 40, 345–364, 2001.
- Bohren, C. F., and D. R. Huffman, *Absorption and scattering of light by small particles*, John Wiley and Sons, New York, 1998, 530 pp.
- Brown, P. R. A., and P. N. Francis, Improved measurements of the ice water content in cirrus using a total-water probe, *Journal of Atmospheric and Oceanic Technology*, 12, 410–414, 1995.
- Buehler, S. A., Cloud ice water submillimeter imaging radiometer, 20, University of Bremen, Bremen, Germany, 2005.
- Buehler, S. A., C. Jimenez, K. F. Evans, B. Rydberg, P. Eriksson, and A. J. Heymsfield, A concept for a satellite mission to measure cloud ice water path and ice particle size, *Quarterly Journal of the Royal Meteorological Society*, 133, 109–128, 2007.
- Cadeddu, M. P., Evaluation of water permittivity models from ground-based observations of cold clouds at frequencies between 23 and 170 GHz, *IEEE Transactions on Geoscience and Remote Sensing*, 49, 2999–3008, 2011.
- Chepfer, H., G. Brogniez, P. Goloub, F. M. Breno, and P. H. Flamant, Observations of horizontally oriented ice crystals in cirrus clouds with POLDER-1/ADEOS-1, *Journal of Quantitative Spectroscopy and Radiative Transfer*, 63, 521–543, 1999.
- Collier, C. G., *Applications of weather radar systems: A guide to uses of radar data in meteorology and hydrology*, Ellis Horwood Limited, 1989, 294 pp.

- Cordisco, E., C. Prigent, and F. Aires, Snow characterization at a global scale with passive microwave satellite observation, *Journal of Geophysical Research*, *111*, D19102, doi:10.1029/2005JD006773, 2006.
- Cornet, C., L. C-Labonnote, and F. Szczap, Three-dimensional polarized Monte Carlo atmospheric radiative transfer model (3DMCPOL): 3D effects on polarized visible reflectances of a cirrus clouds, *Journal of Quantitative Spectroscopy and Radiative Transfer*, *111*, 174–186, 2010.
- Crewell, S., K. Ebell, U. Löhnert, and D. D. Turner, Can liquid water profiles be retrieved from passive microwave zenith observations?, *Geophysical Research Letters*, *36*, L06803, doi:10.1029/2008GL036934, 2009.
- Czekala, H., and C. Simmer, Microwave radiative transfer with nonspherical precipitating hydrometeors, *Journal of Quantitative Spectroscopy and Radiative Transfer*, *60*, 365–374, 1998.
- Czekala, H., S. Havemann, K. Schmidt, T. Rother, and C. Simmer, Comparison of microwave radiative transfer calculations obtained with three different approximations of hydrometeor shape, *Journal of Quantitative Spectroscopy and Radiative Transfer*, *63*, 545–558, 1999.
- Czekala, H., S. Crewell, C. Simmer, and A. Thiele, Discrimination of cloud and rain liquid water by groundbased polarized microwave radiometry, *Geophysical Research Letters*, *28*, 267–270, 2001a.
- Czekala, H., S. Crewell, C. Simmer, A. Thiele, A. Hornbostel, and A. Schroth, Interpretation of polarization features in ground-based microwave observations as caused by horizontally aligned oblate raindrops, *Journal of Applied Meteorology*, *40*, 1918–1932, 2001b.
- Davis, C. P., D. L. Wu, C. Emde, J. H. Jiang, R. E. Cofield, and R. S. Harwood, Cirrus induced polarization in 122 GHz aura microwave limb sounder radiances, *Geophysical Research Letters*, *32*, doi:10.1029/2005GL022681, 2005.
- Debye, P., Der Lichtdruck auf Kugeln von beliebigem Material, *Annals of Physics*, *30*, 57–136, 1909.
- Defer, E., C. Prigent, F. Aires, J. R. Pardo, C. J. Walden, O.-Z. Zanife, J.-P. Chaboureaud, and J.-P. Pinty, Development of precipitation retrievals at millimeter and sub-millimeter wavelengths for geostationary satellites, *Journal of Geophysical Research*, *113*, doi:10.1029/2007JD008673, 2008.
- Delanoë, J., and R. J. Hogan, Combined CloudSat-CALIPSO-MODIS retrievals of the properties of ice clouds, *Journal of Geophysical Research*, *115*, D00H29, doi:10.1029/2009JD012346, 2010.
- Draine, B. T., and P. J. Flatau, Discrete-dipole approximation for scattering calculations, *Journal of the Optical Society of America A*, *11*, 1491–1499, 1994.
- Draine, B. T., and P. J. Flatau, User guide for the discrete dipole approximation code DDSCAT 6.1, available online, <http://arxiv.org/abs/astro-ph/0409262v2>, 2004.
- Ellison, W., Freshwater and sea water, in *Thermal Microwave Radiation: Applications for Remote Sensing*, IET Electromagnetic Waves Serial Volume 52, edited by C. Mätzler, pp. 431–455, The Institution of Engineering and Technology, Stevenage, U. K., 2006.

- Evans, K. F., Submillimeter-wave ice cloud radiometry channel selection study, *Technical report*, University of Colorado, Boulder, USA, 2004, available online, <http://nit.colorado.edu/mwcirrus>.
- Evans, K. F., and A. H. Evans, The prospect for remote sensing of cirrus clouds with a submillimeter-wave spectrometer, *Journal of Applied Meteorology*, *38*, 514–525, 1999.
- Evans, K. F., and G. L. Stephens, A new polarized atmospheric radiative transfer model, *Journal of Quantitative Spectroscopy and Radiative Transfer*, *46*, 413–423, 1991.
- Evans, K. F., and G. L. Stephens, Microwave radiative transfer through clouds composed of realistically shaped ice crystals. Part I: Single scattering properties, *Journal of the Atmospheric Sciences*, *52*, 2041–2057, 1995a.
- Evans, K. F., and G. L. Stephens, Microwave radiative transfer through clouds composed of realistically shaped ice crystals. Part II: Remote sensing of ice clouds, *Journal of the Atmospheric Sciences*, *52*, 2058–2072, 1995b.
- Evans, K. F., and J. Vivekanandan, Multiparameter Radar and Microwave Radiative Transfer Modeling of Nonspherical Atmospheric Ice Particles, *IEEE Transactions on Geoscience and Remote Sensing*, *28*, 423–437, 1990.
- Evans, K. F., S. J. Walter, A. J. Heymsfield, and G. M. McFarquhar, Submillimeterwave cloud ice radiometer: simulations of retrieval algorithm performance, *Journal of Geophysical Research*, *107*, doi:10.1029/2001JD000709, 2002.
- Evans, K. F., J. R. Wang, P. E. Racette, G. Heymsfield, and L. Li, Ice cloud retrievals and analysis with the compact scanning submillimeter imaging radiometer and cloud radar system during CRYSTAL FACE, *Journal of Applied Meteorology*, *44*, 839–859, 2005.
- Field, P. R., R. J. Hogan, P. R. A. Brown, A. J. Illingworth, T. W. Choullarton, and R. J. Cotton, Parameterization of ice-particle size distributions for mid-latitude stratiform clouds, *Quarterly Journal of the Royal Meteorological Society*, *131*, 1997–2017, 2005.
- Fleishauer, R. P., V. E. Larson, and T. H. Vonder Haar, Observed microphysical structure of midlevel, mixed-phase clouds, *Journal of the Atmospheric Sciences*, *59*, 1779–1803, 2002.
- Gasiewski, A. J., Numerical sensitivity analysis of passive EHF and SMMW channels to tropospheric water vapor, clouds, and precipitation, *IEEE Transactions on Geoscience and Remote Sensing*, *30*, 859–870, 1992.
- Greco, M., and W. S. Olson, Precipitating snow retrievals from combined airborne cloud radar and millimeter-wave radiometer observations, *Journal of Applied Meteorology and Climatology*, *47*, 1634–1650, 2008.
- Haferman, J. L., Microwave scattering by precipitation, in *Light scattering by nonspherical particles: Theory, measurements, and geophysical applications*, edited by M. I. Mishchenko *et al.*, p. Chapter 17, Academic Press, 2000.
- Harlow, R. C., Airborne retrievals of snow microwave emissivity at AMSU frequencies using ARTS/SCEM-UA, *Journal of Applied Meteorology and Climatology*, *46*, 23–35, 2007.
- Heymsfield, A., Ice crystal terminal velocities, *Journal of the Atmospheric Sciences*, *7*, 1348–1357, 1972.

- Heymsfield, A. J., C. Schmitt, A. Bansemmer, and C. H. Twohy, Improved representation of ice particle masses based on observations in natural clouds, *Journal of the Atmospheric Sciences*, *67*, 3303–3318, 2010.
- Heymsfield, G. M., and R. Fulton, Passive Microwave and Infrared Structure of Mesoscale Convective Systems, *Meteorology and Atmospheric Physics*, *54*, 123–139, 1994.
- Hogan, R. J., M. P. Mittermaier, and A. J. Illingworth, The retrieval of ice water content from radar reflectivity factor and temperature and its use in evaluating a mesoscale model, *Journal of Applied Meteorology and Climatology*, *45*, 301–317, 2006.
- Hogan, R. J., L. Tian, P. R. A. Brown, C. D. Westbrook, A. J. Heymsfield, and J. D. Eastment, Radar scattering from ice aggregates using the horizontally aligned oblate spheroid approximation, *Journal of Applied Meteorology and Climatology*, *in press*, doi:10.1175/JAMC-D-11-074, 2011.
- Hogan, R. J., L. Tian, P. R. A. Brown, C. D. Westbrook, A. J. Heymsfield, and J. D. Eastment, Radar scattering from ice aggregates using the horizontally aligned oblate spheroid approximation, *Journal of Applied Meteorology and Climatology*, *51*, 655–671, 2012.
- Hong, G., P. Yang, B. A. Baum, A. J. Heymsfield, F. Weng, Q. Liu, G. Heygster, and S. Buehler, Scattering database in the millimeter and submillimeter wave range of 100–1000 GHz for nonspherical particles, *Journal of Geophysical Research*, *114*, D06201, doi:10.1029/2008JD010451, 2009.
- Hufford, G., A model for the complex permittivity of ice at frequency below 1 THz, *International Journal of Infrared and Millimeter Waves*, *12*, 677–682, 1991.
- Jiang, J. H., and D. L. Wu, Ice and water permittivity for millimeter and sub-millimeter remote sensing applications, *Atmospheric Science Letter*, *5*, 146–151, 2004.
- Jiménez, C., S. A. Buehler, B. Rydberg, P. Eriksson, and K. F. Evans, Performance simulations for a submillimeter-wave satellite instrument to measure cloud ice, *Quarterly Journal of the Royal Meteorological Society*, *133*, 129–149, 2007.
- Kahnert, F. M., Numerical methods in electromagnetic scattering theory, *Journal of Quantitative Spectroscopy and Radiative Transfer*, *79–80*, 775–824, 2003.
- Kim, M.-J., A physical model to estimate snowfall over land using microwave measurements, *Doctoral Thesis*, University of Washington, Washington, USA, 2004.
- Kim, M.-J., J. A. Weinman, W. S. Olson, D.-E. Chang, G. Skofronick-Jackson, and J. R. Wang, A physical model to estimate snowfall over land using AMSU-B observations, *Journal of Geophysical Research*, *113*, D09201, doi:10.1029/2007JD008589, 2008.
- Kneifel, S., U. Löhnert, A. Battaglia, S. Crewell, and D. Siebler, Snow scattering signals in ground-based passive microwave radiometer measurements, *Journal of Geophysical Research*, *115*, D16214, doi:10.1029/2010JD013856, 2010.
- Kneifel, S., M. Maahn, G. Peters, and C. Simmer, Observation of snowfall with a low-power FM-CW K-band radar (Micro Rain Radar), *Meteorology and Atmospheric Physics*, *113*, 75–87, 2011.
- Korolev, A., and G. Isaac, Roundness and aspect ratio of particles in ice clouds, *Journal of the Atmospheric Sciences*, *60*, 1795–1807, 2003.

- Kutuza, B. G., G. K. Zagorin, A. Hornbostel, and A. Schroth, Physical modeling of passive polarimetric microwave observations of the atmosphere with respect to the third Stokes parameter, *Radio Science*, *33*, 677–695, 1998.
- Levizzani, V., S. Laviola, and E. Cattani, Detection and measurement of snowfall from space, *Remote Sensing*, *3*, 145–166, 2011.
- Liebe, H. J., MPM—an atmospheric millimeter wave propagation model, *International Journal of Infrared and Millimeter Waves*, *10*, 631–650, 1989.
- Liou, K.-N., Review influence of cirrus clouds on weather and climate processes: a global perspective, *Monthly Weather Review*, *114*, 1167–1199, 1986.
- Liou, K. N., *An introduction to atmospheric radiation*, Academic Press, San Diego, 2002, 583 pp.
- Liu, G., A database of microwave single-scattering properties for nonspherical ice particles, *Bulletin of the American Meteorological Society*, *10*, 1563–1570, 2008.
- Löffler-Mang, M., and J. Joss, An optical disdrometer for measuring size and velocity of hydrometeors, *Journal of Atmospheric and Oceanic Technology*, *17*, 130–139, 2000.
- Löhnert, U., and S. Crewell, Accuracy of cloud liquid water path from ground-based microwave radiometry, *Radio Science*, *38*, doi:10.1029/2002RS002654, 2003.
- Löhnert, U., S. Kneifel, A. Battaglia, M. Hagen, L. Hirsch, and S. Crewell, A multi-sensor approach towards a better understanding of snowfall microphysics: The TOSCA project, *Bulletin of the American Meteorological Society*, *92*, 613–628, 2011.
- Marshall, J. S., and W. M. Palmer, The distribution of rain drops with size, *Journal of the Atmospheric Sciences*, *5*, 165–166, 1948.
- Matrosov, S. Y., Modeling backscatter properties of snowfall at millimeter wavelengths, *Journal of the Atmospheric Sciences*, *64*, 1727–1736, 2007.
- Mätzler, C., and U. Wegmüller, Dielectric properties of fresh-water ice at microwave frequencies, *Journal of Physics D: Applied Physics*, *20*, 1623–1630, 1987.
- Mätzler, C., P. W. Rosenkranz, and J. Cermak, Microwave absorption of supercooled clouds and implications for dielectric properties of water, *Journal of Geophysical Research*, *115*, D23208, doi:10.1029/2010JD014283, 2010.
- Mätzler, C., Dielectric properties of natural media, in *Thermal Microwave Radiation: Applications for Remote Sensing, IET Electromagn. Waves Ser. vol. 52*, edited by C. Mätzler, pp. 427–495, The Institution of Engineering and Technology, Stevenage, U. K., 2006.
- Miao, J., K.-P. Johnsen, S. Buehler, and A. Kokhanovsky, The potential of polarization measurements from space at mm and sub-mm wavelengths for determining cirrus cloud parameters, *Atmospheric Chemistry and Physics*, *3*, 39–48, 2003.
- Mie, G., Beiträge zur Optik trüber Medien, speziell kolloidaler Metallösungen, *Annalen der Physik*, *25*, 377–445, 1908.
- Minnis, P., D. F. Young, K. Sassen, J. M. Alverez, and C. J. Grund, The 27–28 October 1986 FIRE IFO cirrus case study: cirrus parameter relationships derived from satellite and lidar data, *Monthly Weather Review*, *118*, 2402–2425, 1990.

- Mishchenko, M. I., Calculation of the amplitude matrix for a nonspherical particle in a fixed orientation, *Applied Optics*, *39*, 1026–1031, 2000.
- Mishchenko, M. I., L. D. Travis, and D. W. Mackowski, T-matrix computations of light scattering by nonspherical particles: a review, *Journal of Quantitative Spectroscopy and Radiative Transfer*, *55*, 535–575, 1996.
- Mishchenko, M. I., L. D. Travis, and A. A. Lacis, *Scattering, absorption, and emission of light by small particles*, Cambridge University Press, Cambridge, 2002, 448 pp.
- Noel, V., and H. Chepfer, Study of ice crystal orientation in cirrus clouds based on satellite polarized radiance measurements, *Journal of the Atmospheric Sciences*, *61*, 2073–2081, 2004.
- Noel, V., and H. Chepfer, A global view of horizontally oriented crystals in ice clouds from Cloud-Aerosol Lidar and Infrared Pathfinder Satellite Observation (CALIPSO), *Journal of Geophysical Research*, *115*, D00H23, doi:10.1029/2009JD012365, 2010.
- Noel, V., and K. Sassen, Study of planar ice crystal orientations in ice clouds from scanning polarization lidar observation, *Journal of Applied Meteorology*, *44*, 653–664, 2005.
- Noel, V., H. Chepfer, M. Haefelin, and Y. Morille, Classification of ice crystal shapes in midlatitude ice clouds from three years of lidar observations over the SARTA observatory, *Journal of the Atmospheric Sciences*, *63*, 2978–2991, 2006.
- Noh, Y.-J., Observational analysis and retrieval of snow using satellite data at high microwave frequencies, *Doctoral Thesis*, The Florida State University, Florida, USA, 2006.
- Ono, A., The shape and riming properties of ice crystals in natural clouds, *Journal of the Atmospheric Sciences*, *26*, 138–147, 1969.
- Pardo, J. R., J. Cernicharo, and E. Serabyn, Atmospheric transmission at microwaves (ATM): an improved model for millimeter/submillimeter applications, *IEEE Transactions on Antennas and Propagation*, *49*, 1683–1694, 2001.
- Pardo, J. R., E. Serabyn, M. C. Wiedner, and J. Cernicharo, Atmospheric transmission at microwaves (ATM): an improved model for millimeter/submillimeter applications, *Journal of Quantitative Spectroscopy and Radiative Transfer*, *96*, 537–545, 2005.
- Petty, G. W., *A first course in atmospheric radiation (Second Edition)*, Sundog publishing, Madison, 2006, 459 pp.
- Prigent, C., J. R. Pardo, M. I. Mishchenko, and W. B. Rossow, Microwave polarized signatures generated within cloud systems: Special sensor microwave imager (SSM/I) observations interpreted with radiative transfer simulations, *Journal of Geophysical Research*, *106*, 28243–28258, 2001.
- Prigent, C., E. Defer, J. R. Pardo, C. Pearl, W. B. Rossow, and J.-P. Pinty, Relations of polarized scattering signatures observed by the TRMM microwave instrument with electrical processes in cloud systems, *Geophysical Research Letters*, *32*, doi:10.1029/2004GL022225, 2005.
- Protat, A., J. Delanoë, E. J. O’Connor, and T. S. L’Ecuyer, The evaluation of CloudSat and CALIPSO ice microphysical products using ground-based cloud radar and lidar observations, *Journal of Atmospheric and Oceanic Technology*, *27*, 793–810, 2010.

- Pruppacher, H. R., and J. D. Klett, *Microphysics of clouds and precipitation, Second Edition*, Kluwer Academic, Dordrecht, The Netherlands, 1997, 954 pp.
- Purcell, E. M., and C. R. Pennypacker, Scattering and absorption of light by nonspherical dielectric gains, *The Astrophysical Journal*, *186*, 705–714, 1973.
- Rauber, R. M., and A. Tokay, An explanation for the existence of supercooled water at the top of cold clouds, *Journal of the Atmospheric Sciences*, *48*, 1005–1023, 1991.
- Redl, S., Mikrowellensignale von unterkühlten Flüssigwasserwolken, *Diploma Thesis*, University of Cologne, Cologne, Germany, 2011.
- Roberti, L., and C. Kummerow, Monte Carlo calculations of polarized microwave radiation emerging from cloud structures, *Journal of Climatology and Applied meteorology*, *104*, 2093–2104, 1999.
- Rosenkranz, P. W., Water vapor microwave continuum absorption: a comparison of measurements and results, *Radio Science*, *33*, 919–928, 1998.
- Schulz, F. M., K. Stamnes, and F. Weng, VDISORT, an improved and generalized discrete ordinate method for polarized (vector) radiative transfer, *Journal of Quantitative Spectroscopy and Radiative Transfer*, *61*, 105–122, 1999.
- Siebler, D., Bestimmung von Größen und Formfaktoren von Schnee anhand von Messungen am Schneefernerhaus, *Diploma Thesis*, University of Munich, Munich, Germany, 2010.
- Skofronick-Jackson, G., and B. T. Johnson, Surface and atmospheric contributions to passive microwave brightness temperatures for falling snow events, *Journal of Geophysical Research*, *116*, D02213, doi:10.1029/2010JD014438, 2011.
- Skofronick-Jackson, G. M., A. J. Gasiewski, and J. R. Wang, Influence of microphysical cloud parameterizations on microwave brightness temperatures, *IEEE Transactions on Geoscience and Remote Sensing*, *40*, 187–196, 2002.
- Skofronick-Jackson, G. M., M.-J. Kim, J. A. Weinman, and D.-E. Chang, A physical model to determine snowfall over land by microwave radiometry, *IEEE Transactions on Geoscience and Remote Sensing*, *42*, 1047–1058, 2004.
- Spencer, R. W., W. S. Olson, R. Wu, D. W. Martin, J. A. Weinman, and D. A. Santek, Heavy thunderstorms observed over land by the Nimbus-7 scanning multichannel microwave radiometer, *Journal of Climatology and Applied meteorology*, *22*, 1041–1046, 1983.
- Spencer, R. W., H. M. Goodman, and R. E. Hood, Precipitation retrieval over land and ocean with the SSM/I: identification and characteristics of the scattering signal, *Journal of Atmospheric and Oceanic Technology*, *6*, 254–273, 1989.
- Stephens, G. L., and C. D. Kummerow, The remote sensing of clouds and precipitation from space: A review, *Journal of the Atmospheric Sciences*, *64*, 3742–3765, 2007.
- Stephens, G. L., D. G. Vane, R. J. Boain, G. G. Mace, K. Sassen, Z. Wang, A. J. Illingworth, E. J. O’Connor, W. B. Rossow, S. L. Durden, S. D. Miller, and the CloudSat Science Team, The CAPLISO mission: A global 3D view of aerosols and clouds, *Bulletin of the American Meteorological Society*, *83*, 1771–1790, 2002.

- Stogryn, A.P., H. T. Bull, K. Rubayi, and S. Irvan chy, The microwave permittivity of sea and fresh water, *Aerojet Report*, 1995, <http://rime.aos.wisc.edu/MW/models/stogryn.shtml>.
- Stokes, G. G., On the composition and resolution of streams of polarized light from difference sources, *Transactions of the Cambridge Philosophical Society*, *9*, 399–423, 1852.
- Sun, W., Y. Hu, B. Lin, Z. Liu, and G. Videen, The impact of ice cloud particle microphysics on the uncertainty of ice water content retrievals, *Journal of Quantitative Spectroscopy and Radiative Transfer*, *112*, 189–196, 2011.
- Troitsky, A. V., A. M. Osharin, A. V. Korolev, and J. W. Strapp, Polarization of thermal microwave atmospheric radiation due to scattering by ice particles in clouds, *Journal of the Atmospheric Sciences*, *60*, 1608–1620, 2003.
- Turner, D., P. Cadeddu, U. Löhnert, S. Crewell, and A. M. Vogelmann, Modifications to the water vapor continuum in the Microwave suggested by ground-based 150 GHz Observations, *IEEE Transactions on Geoscience and Remote Sensing*, *47*, 3326–3337, doi:10.1109/TGRS.2009.2022262, 2009.
- van de Hulst, H. C., *Light scattering by small particles*, Wiley, New York, 1957, 470 pp.
- Wallace, J. M., and P. V. Hobbs, *Atmospheric science: an introductory survey, Second Edition*, Elsevier, 2006, 483 pp.
- Wang, J. R., G. Liu, J. D. Spinhirne, P. Racette, and W. D. Hart, Observations and retrievals of cirrus cloud parameters using multichannel millimeter-wave radiometric measurements, *Journal of Geophysical Research*, *106*, 15251–15263, doi:10.1029/2000JD900262, 2001.
- Waterman, P. C., Matrix formulation of electromagnetic scattering, *Proceedings of IEEE*, *53*, 805–812, 1965.
- Winker, D. M., J. Pelon, J. A. Coakley Jr., S. A. Ackerman, R. J. Charlson, P. R. Colarco, P. Flamant, Q. Fu, R. M. Hoff, C. Kittaka, T. L. Kubar, H. Le Treut, M. P. McCormick, G. Mégie, L. Poole, K. Powell, C. Trepte, M. A. Vaughan, and B. A. Wielicki, The CloudSat mission and the A-train: A new dimension of space-based observations of clouds and precipitation, *Bulletin of the American Meteorological Society*, *91*, 1211–1229, 2010.
- Woods, C. P., M. T. Stoelinga, and J. D. Locatelli, The IMPROVE-1 storm of 1-2 February 2001. Part III: Sensitivity of a mesoscale model simulation to the representation of snow particle types and testing of a bulk microphysical scheme with snow habit prediction, *Journal of the Atmospheric Sciences*, *64*, 3927–3948, 2007.
- Wu, D. L., J. H. Jiang, and C. P. Davis, EOS MLS cloud ice measurements and cloudy-sky radiative transfer model, *IEEE Transactions on Geoscience and Remote Sensing*, *44*, 1156–1165, 2006.
- Wu, D. L., H. M. Pickett, and N. J. Livesey, Aura MLS THz observations of global cirrus near the tropopause, *Geophysical Research Letters*, *35*, L15, doi:10.1029/2008GL034233, 2008.
- Wu, R., and J. A. Weinman, Microwave radiances from precipitating clouds containing aspherical ice, combined phase, and liquid hydrometeors, *Journal of Geophysical Research*, *89*, 7170–7178, 1984.

- Wylie, D. P., W. P. Menzel, H. M. Woolf, and K. I. Strabala, Four years of global cirrus cloud statistics using HIRS, *Journal of Climate*, 7, 1972–1986, 1994.
- Xie, X., and J. Miao, Polarization difference due to nonrandomly oriented ice particles at millimeter/submillimeter waveband, *Journal of Quantitative Spectroscopy and Radiative Transfer*, 112, 1090–1098, 2011.
- Xie, X., J. Miao, and W. Wang, Microwave radiative transfer in scattering atmosphere: Effects of complex permittivity of ice spherical crystals, *Journal of Quantitative Spectroscopy and Radiative Transfer*, 110, 1124–1131, 2009.
- Xie, X., U. Löhnert, S. Kneifel, and S. Crewell, Snow particle orientation observed by ground-based microwave radiometry, *Journal of Geophysical Research*, 117, D02206, doi:10.1029/2011JD016369, 2012.
- Yang, P., and K. N. Liou, Finite-difference time domain method for light scattering by small ice crystals in three dimensional space, *Journal of the Optical Society of America A*, 13, 2072–2085, 1996.
- Yang, P., M. Wendisch, L. Bi, G. Kattawar, M. Mishchenko, and Y. Hu, Dependence of extinction cross-section on incident polarization state and particle orientation, *Journal of Quantitative Spectroscopy and Radiative Transfer*, 112, 2035–2039, 2011.
- Yurkin, M. A., and A. G. Hoekstra, The discrete dipole approximation: an overview and recent developments, *Journal of Quantitative Spectroscopy and Radiative Transfer*, 106, 558–589, 2007.
- Yurkin, M. A., and A. G. Hoekstra, The discrete-dipole-approximation code ADDA: capabilities and known limitations, *Journal of Quantitative Spectroscopy and Radiative Transfer*, 112, 2234–2247, 2011.

Danksagung

Part of the work was supported by the National Natural Science Foundation of China (NSFC) under grants 40476061 and 40525015, and by the Innovation Foundation of BUAA for PhD Graduates. The work carried out in Germany has been funded by the China Scholarship Council (CSC).

I would like to express my gratitude to my supervisor Prof. Jungang Miao from Beihang University (BUAA) who encouraged and supported me throughout my PhD study. His guidance enabled me to understand the subject and was invaluable to me. I wish to acknowledge my supervisors Prof. Susanne Crewell and Dr. Ulrich Löhnert from University of Cologne for their guidance and invaluable suggestions for my work in Germany. I am deeply indebted to the three of them. Without their support the work would not be possible.

I thank the Fernerkundung Gruppe, Kerstin Ebell, Sonja Reitter, Gerrit Maschwitz, Emilliano Orlandi, Jan Schween, Rainer Haseneder-Lind, Sandra Steike, Stephanie Redl, Mario Mech, Maximilian Maahn, Stefan Kneifel and Ulrich Löhnert. I wish to thank Stefan and Uli for the fruitful discussions that always gave me new ideas to improve my research work. Every time Gerrit and Mario fixed the computer problems for me. I can always ask Kerstin and Sonja when I had questions either during work or in the daily life. Jan and Rainer gave me a lot of useful suggestions for the instrument data processing. I wish to thank Max and Chi Yan Tsui for their help with the proofreading of the thesis.

I thank Michael Mishchenko for providing his T-matrix code for public use and Bruce T. Draine and Piotr J. Flatau for DDSCAT code package. I wish to thank K. Franklin Evans for his RT4 model package which is used in this study for radiative transfer calculations. I would also like to thank Martin Hagen from German Aerospace Center (DLR) for the MRR data and Maximilian Maahn for data processing. The German Weather Service (DWD) which provides the ceilometer data at UFS and weather observations at the summit of Mount Zugspitze is also acknowledged.

The supports from my former colleagues from BUAA are acknowledged, especially the group members Yingshu Piao, Mu qiao, Haibo Zhao, Wei Zeng, Hairui Liu, Lili Jiang, Yan Xu and Yongfang Zhang. Special thanks to all my friends in China who gave me a lot of help. I am also grateful to my friends in Germany, especially Stefanie Rau who helped me with my German.

Especially, I wish to express my gratitude to my beloved family, for their support and understanding throughout these years.

Erklärung

Ich versichere, dass ich die von mir vorgelegte Dissertation selbständig angefertigt, die benutzten Quellen und Hilfsmittel vollständig angegeben und die Stellen der Arbeit - einschließlich Tabellen, Karten und Abbildungen -, die anderen Werken im Wortlaut oder dem Sinn nach entnommen sind, in jedem Einzelfall als Entlehnung kenntlich gemacht habe; dass diese Dissertation noch keiner anderen Fakultät oder Universität zur Prüfung vorgelegen hat; dass sie - abgesehen von unten angegebenen Teilpublikationen - noch nicht veröffentlicht worden ist sowie, dass ich eine solche Veröffentlichung vor Abschluss des Promotionsverfahrens nicht vornehmen werde. Die Bestimmungen dieser Promotionsordnung sind mir bekannt. Die von mir vorgelegte Dissertation ist von Prof. Dr. S. Crewell betreut worden.

Köln, den 23. 04. 2012

Xinxin Xie

Teilveröffentlichungen

- Xie, X., J. Miao, and W. Wang, Microwave radiative transfer in scattering atmosphere: Effects of complex permittivity of ice spherical crystals, *Journal of Quantitative Spectroscopy and Radiative Transfer*, 110, 1124-1131, 2009.
- Xie, X., and J. Miao, Polarization difference due to nonrandomly oriented ice particles at millimeter/submillimeter waveband, *Journal of Quantitative Spectroscopy and Radiative Transfer*, 112, 1090-1098, 2011.
- Xie, X., U. Löhnert, S. Kneifel, and S. Crewell, Snow particle orientation observed by ground-based microwave radiometry, *Journal of Geophysical Research*, 117, D02206, doi:10.1029/2011JD016369, 2012.

